

**DEVELOPMENT OF A NAVIER STOKES SOLVER FOR  
COMPRESSIBLE VISCOUS FLOWS AND COUPLING IT  
WITH OPTIMIZATION CODES**

**SIKIŞTIRILABİLİR VİSKOZ AKIŞLAR İÇİN BİR NAVIER  
STOKES ÇÖZÜCÜSÜNÜN GELİŞTİRİLMESİ VE  
OPTİMİZASYON KODLARIYLA EŞLENMESİ**

**Burak PEHLİVAN**

**Assist. Prof. Dr. Özgür EKİCİ**

**Supervisor**

Submitted to

Graduate School of Science and Engineering of Hacettepe University

as a Partial Fulfillment to the Requirements

for the Award of the Degree of Master of Science

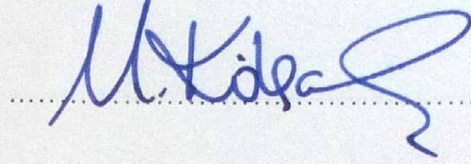
in Mechanical Engineering

2019

This work titled "**Development Of A Navier Stokes Solver For Compressible Viscous Flows And Coupling It With Optimization Codes**" by Burak Pehlivan has been approved as a thesis for the Degree of **Master of Science in Mechanical Engineering** by the Examining Committee members mentioned below.

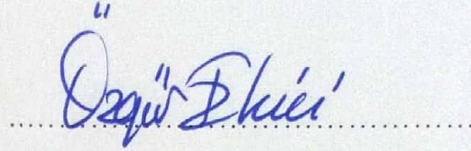
Prof. Dr. Murat KÖKSAL

Head



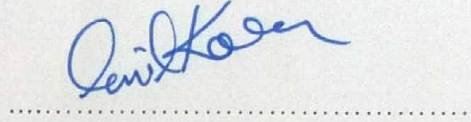
Asst. Prof. Dr. Özgür EKİCİ

Advisor



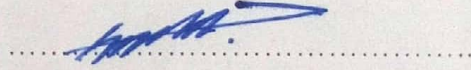
Prof. Dr. Cemil KOÇAR

Member



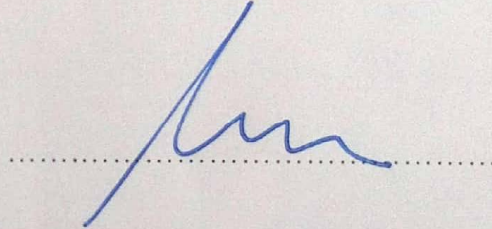
Asst. Prof. Dr. Bilsay SÜMER

Member



Asst. Prof. Dr. Mustafa KAYA

Member



This thesis has been approved as a thesis for the Degree of **Master of Science in Mechanical Engineering** by Board of Directors of Graduate School of Science and Engineering on .... / .... / .....

Prof. Dr. Menemşe GÜMÜŞDERELİOĞLU  
Director of the Institute of  
Graduate School of Science and Engineering

## ETHICS

In this thesis study, prepared in accordance with the spelling rules of Institute of Graduate Studies in Science of Hacettepe University,

I declare that

- all the information and documents have been obtained in the base of the academic rules,
- all audio-visual and written information and results have been presented according to the rules of scientific ethics,
- in case of using others Works, related studies have been cited in accordance with the scientific standards,
- all cited studies have been fully referenced
- I did not do any distortion in the data set,
- and any part of this thesis has not been presented as another thesis study at this or any other university.

12/6/2019

Burak PEHLIVAN



## YAYINLAMA VE FİKRİ MÜLKİYET HAKLARI BEYANI

Enstitü tarafından onaylanan lisansüstü tezimin / raporumun tamamını veya herhangi bir kısmını, basılı(kağıt) ve elektronik formatta arşivleme ve aşağıda verilen koşullarla kullanıma açma iznini Hacettepe Üniversitesine verdiğimi bildiririm. Bu izinle Üniversiteye verilen kullanım hakları dışındaki tüm fikri mülkiyet haklarım bende kalacak, tezimin tamamının ya da bir bölümünün gelecekteki çalışmalarda (makale, kitap, lisans ve patent vb.) kullanım hakları bana ait olacaktır.

Tezin kendi orijinal çalışmam olduğunu, başkalarının haklarını ihlal etmediğimi ve tezimin tek yetkili sahibi olduğumu beyan ve taahhüt ederim. Tezimde yer alan telif hakkı bulunan ve sahiplerinden yazılı izin alınarak kullanılması zorunlu metinlerin yazılı izin alınarak kullandığımı ve istenildiğinde suretlerini Üniversiteye teslim etmeyi taahhüt ederim.

Yükseköğretim Kurulu tarafından yayınlanan **“Lisansüstü Tezlerin Elektronik Ortamda Toplanması, Düzenlenmesi ve Erişime Açılmasına İlişkin Yönerge”** kapsamında tezim aşağıda belirtilen koşullar haricinde YÖK Ulusal Tez Merkezi / H. Ü. Kütüphaneleri Açık Erişim Sisteminde erişime açılır.

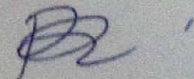
o Enstitü / Fakülte yönetim kurulu kararı ile tezimin erişime açılması mezuniyet tarihimden itibaren 2 yıl ertelenmiştir. <sup>(1)</sup>

o Enstitü / Fakülte yönetim kurulunun gerekçeli kararı ile tezimin erişime açılması mezuniyet tarihimden itibaren .... ay ertelenmiştir.

o Tezimle ilgili gizlilik kararı verilmiştir.

12.6.2019

Burak PEHLİVAN



## ÖZET

### SIKIŞTIRILABİLİR VİSKOZ AKIŞLAR İÇİN BİR NAVIER STOKES ÇÖZÜCÜSÜNÜN GELİŞTİRİLMESİ VE OPTİMİZASYON KODLARIYLA EŞLENMESİ

**Burak PEHLİVAN**

**Yüksek Lisans, Makine Mühendisliği**

**Tez Danışmanı: Dr. Öğr. Gör. Özgür EKİCİ**

**Haziran 2019, 104 sayfa**

Tezde, sıkıştırılmaz ve sıkıştırılabilir akışlar için Navier Stokes çözümleri geliştirilmiştir. Kodlar, sonrasında optimizasyon algoritmalarıyla eşlenerek optimizasyon çalışmaları gerçekleştirilmiştir.

Sıkıştırılmaz 2 boyutlu akışta, sadece 3 denklem ( $u, v, P$ ) gerekirken sıkıştırılabilir 2 boyutlu akışta 5 denklem ( $u, v, P, T, \rho$ ) gereklidir. Sıkıştırılabilir akış çözümleri genellikle çözüm için daha uzun süre gerektirir. Normalde mevcut olan ticari akış çözümleri sıkıştırılabilir ya da sıkıştırılmaz akış çözümleri olarak çalışırlar. Daha hızlı bir şekilde çözüme yakınsama daha düşük mertebeden bir algoritma, kaba bir ağ ya

da problemi sıkıştırılmaz olarak çözmekle mümkün olur. Bunun yanında, hesaplamalı aerodinamikte, 3 boyutlu geometrilerde hızlı çözümler öncelikle sıkıştırılmaz akış çözümleriyle mümkün olur, daha sonra çözümde iyileştirme sıkıştırılabilir akış çözücüsüyle elde edilir, böylece iki çözüm gerçekleştirilir (iki adımlı yaklaşım).

Buradaki temel düşünce, problemi önce bir sıkıştırılmaz akış problemi olarak çözüp, daha sonra elde edilen sonuçları sıkıştırılmaz akış çözümünde ilk şart olarak kullanarak yakınsamayı iyileştirmektir.

Böyle bir kodun yararları:

- İki çözümü birlikte ele alabilecek yapıya sahip bir kodun geliştirilmesi tercih sebebi olacaktır.
- Kökten geliştirilmiş bir Navier Stokes çözücünün geliştirilmesi çeşitli fiziksel modelleri (viskozite, türbülans, ideal olmayan gaz denklemi modelleri) ve farklı ayırıklaştırma modellerini uygulamaya imkan vererek farklı problem uygulamalarında esneklik sağlayacaktır.
- Kökten geliştirilen bir kodu (akış çözücüsü) optimizasyon kodlarıyla birlikte kullanmak, hazır ticari çözücülerle birlikte optimizasyon kodlarını kullanmaya kıyasla çok daha kolaydır. Ticari akış çözücülerinde, akış çözücüsünün kodun optimizasyon koduyla eşlenmesi scriptleme işlemini (programın çıktı dosyasında belirli satırları okuma) gerektirir, bu problemlere sebep olabilir ve binlerce dosyanın yazılması/silinmesi, işlenmesi ve akış çözücüsünün pek çok kez açılmasını gerektirdiği için genel çözümü yavaşlatabilir.

Sıkıştırılabilir akışlar için geliştirilen akış çözücüsü, sıkıştırılabilir akış çözücüsüyle ön koşullandırmaya tabi tutulmuştur. Sahte geçici relaksasyon uygulanarak sıkıştırılabilir ve sıkıştırılmaz akış çözücülerindeki uyum arttırılmıştır. Ön koşullandırmanın çözüm stabilitesini arttırdığı, çözüm süresinde tasarruf sağlayabildiği gözlemlenmiştir.

Geliştirilen akış çözücülerini, kapak güdümlü kavite ve çarpan jet akış problemlerine uygulanmıştır. Sıkıştırılmaz ve sıkıştırılabilir akış rejimleri için elde edilen sonuçlar, var olduğu durumda literatürdeki sonuçlarla kıyaslanmış, iyi bir uyum gözlemlenmiştir.

Son olarak, optimizasyon çalışmaları gerçekleştirilmiştir. Çözücü parametrelerinin optimizasyonu kapsamında, relaksasyon parametreleri, momentum ve basınç düzeltme denklemlerine uygulanan iterasyon sayısı değiştirilerek hesaplama zamanında azalma sağlanmıştır. Çarpan jet akışına yönelik optimizasyon çalışmaları kapsamında, ısı transferi açısından önem taşıyan durma noktası Nusselt sayısı maksimize edilmeye çalışılmış, bunun için sınır şartlarının yanı sıra, geometrik parametreler değişken olarak alınmıştır. Durma noktası Nusselt sayısını maksimize eden parametreler seti elde edilmiştir. Kapak güdümlü akış problemine yönelik örnek bir optimizasyon uygulaması olarak, kapak güdümlü akış için optimizasyon uygulaması geliştirilerek belirli bir hedef sıcaklık için gerekli ısı kuyusu yeri ve sınır şartları optimize edilmiştir.

**Anahtar Kelimeler:** Navier Stokes, sonlu hacimler metodu, sıkıştırılmaz akışlar, sıkıştırılabilir akışlar, optimizasyon, kapak güdümlü kavite akışı, çarpan jet akışı

# **ABSTRACT**

## **DEVELOPMENT OF A NAVIER STOKES SOLVER FOR COMPRESSIBLE VISCOUS FLOWS AND COUPLING IT WITH OPTIMIZATION CODES**

**Burak PEHLİVAN**

**Master's Degree, Department of Mechanical Engineering**

**Supervisor: Assoc. Prof. Dr. Özgür EKICI**

**June 2019, 104 pages**

In the thesis, Navier Stokes solvers have been developed for incompressible and compressible flows. Then the codes have been matched with the optimization algorithms and optimisation studies have been performed.

For an incompressible 2d flow, only 3 equations ( $u$ ,  $v$ ,  $P$ ) are required whereas for a compressible 2d flow 5 equations ( $u$ ,  $v$ ,  $P$ ,  $T$ ,  $\rho$ ) are required. Compressible flow solution takes longer to complete in general. Normally available commercial flow solvers work either as incompressible or compressible flow solvers. Faster convergence is achieved by using a lower order algorithm, or using a coarse mesh or



solving the problem as incompressible. Besides, in computational aerodynamics fast solutions for 3d geometries are achieved first for incompressible flow, then improvement in the solution is obtained with a compressible solver, so generally two solutions are performed. (two step approach)

The main idea here is to solve the problem as if it was an incompressible problem first, then use the results obtained as initial conditions for the compressible solution to speed up the convergence.

Benefits of the code:

- The development of a code that has a structure capable of handling the two solutions together is preferable.
- The development of an in-house Navier stokes solver code provides flexibility in the applications of different problems that makes it possible to utilise various physical models (such as, non-standart viscosity, turbulence, non-ideal gas equation representations) and different discretisation methods.
- An in-house code (flow solver) is much easier to use along with optimization codes compared to commercial solvers. For commercial flow solvers matching the flow solver with the optimization code requires scripting, i.e., reading specific lines on the output files of the program which can cause problems and slow down the overall solution due to writing/deleting thousands of files, processing them, opening the external flow solver many times.

The flow solver developed for the compressible flows has been preconditioned with incompressible flow solver. The coherence between compressible and incompressible flow solvers have been improved by using pseudo-transient under-relaxation. It has been observed that preconditioning increases the solution stability and it can also offer savings in solution time.

The developed flow solvers have been applied to lid driven cavity and impinging jet flow problems. Results that have been obtained for incompressible and compressible

flow regimes have been compared with the results in the literature, and a good coherence has been observed.

Finally, optimisation studies have been performed. Within the context of the optimisation of solver parameters, reduction in computational time has been realised by varying under-relaxation parameters, iteration numbers for the momentum and pressure correction equations. Within the scope of the optimisation studies for impinging jet flow, stagnation point Nusselt number that is important for heat transfer has been studied to be maximised, and for this, boundary conditions as well as geometric parameters have been taken as variable. As an optimisation case study towards lid driven cavity flow problem, optimisation implementation for lid driven cavity flow has been developed and for a specific temperature target, location of the required heat sink and boundary conditions have been optimised.

**Keywords:** Navier-Stokes equations, finite volume method, incompressible flow, compressible flow, optimization, lid driven cavity flow, impinging jet flow

## **ACKNOWLEDGEMENT**

Firstly, I would like to thank my supervisor, Dr. Özgür Ekici, whose guidance has made it possible to write the thesis. His support has always been gratefully appreciated, and his knowledge and expertise in the field has proved invaluable throughout my master study. Without his support, the thesis would have never finished.

I would like to also thank Dr. Funda Kurtuluş and Dr. Murat Köksal and who has significantly contributed to my understanding in fluid dynamics. I would like to thank Dr. Mahmut Aydın and Dr. Selçuk Himmetoğlu who has sparked an interest in me in numerical methods and their application in engineering. I would like to thank Dr. Mustafa Kaya, Dr. Cemil KOCAR and Dr. Bilsay SÜMER for their valuable comments and for their review of the thesis.

Finally, I want to thank my loved family who were always supportive and patient.

## TABLE OF CONTENTS

1. INTRODUCTION.....	1
2. THEORY .....	4
2.1 EQUATIONS SOLVED .....	4
2.2 FINITE VOLUME METHOD WITH DIFFERENT FLUX CALCULATION SCHEMES .....	5
2.2.1 Diffusive Fluxes.....	5
2.2.2 Convective Fluxes.....	5
2.3 SOLUTION OF PRESSURE EQUATION.....	7
2.3.1 Definition of Under-relaxation Terms for Momentum and Pressure Terms ..	9
2.4 SELECTION OF ITERATIVE TECHNIQUE .....	11
2.5 STAGGERED GRID.....	11
2.6 COLLOCATED GRID.....	12
3. PROBLEM OF INTEREST 1- LID DRIVEN CAVITY PROBLEM.....	15
3.1 LITERATURE SURVEY FOR THE PROBLEM .....	15
3.2 RESULTS FOR LID DRIVEN CAVITY PROBLEM.....	22
3.2.1 INCOMPRESSIBLE FLOW, STAGGERED GRID (Problem No: 1-3) .....	23
3.2.2 INCOMPRESSIBLE FLOW, COLLOCATED GRID (Problem No:4) .....	28
3.2.3 COMPRESSIBLE FLOW, STAGGERED GRID (Problem No: 6-9).....	32
3.3 DISCUSSION OF THE RESULTS .....	46
3.4 COMBINED CODE .....	46
3.4.1 Fixed pseudo-temporal advancement for incompressible and compressible solutions .....	46

3.4.2 Fixed residual for incompressible and compressible solutions .....	47
4. PROBLEM OF INTEREST 2- IMPINGING JET FLOW .....	48
4.1 LITERATURE SURVEY FOR THE PROBLEM .....	48
4.2 DOUBLE SLOT IMPINGING JET FLOW .....	66
4.3 SINGLE SLOT IMPINGING JET FLOW .....	75
5. OPTIMISATION STUDIES .....	80
5.1 OPTIMISATION WITH GENETIC ALGORITHM .....	80
5.2 OPTIMISATION STUDIES WITH STAGGERED GRID .....	82
5.2.1 Optimisation With A Target Middle Temperature .....	83
5.2.2 Optimisation With Top Lid Velocity As An Optimisation Variable .....	85
5.2.3 Optimisation With Top Lid Velocity And Location of a Heat Sink As..... Optimisation Variables.....	86
5.3 OPTIMISATION STUDIES WITH COLLOCATED GRID .....	87
5.3.1 Solver Settings Used As Optimisation Variables(Number Of Iterations for... Momentum and Pressure correction equation) .....	87
5.3.2 Solver Settings Used As Optimisation Variables (Number Of Iterations for.. Momentum and Pressure correction equations, Under-relaxation Terms for Pressure and Momentum) .....	89
5.3.3 First Impinging Jet Optimisation With Only Thermal Parameters.....	90
5.3.4 Second Impinging Jet Optimisation With Thermal, Fluid and Geometric .....	91
Parameters .....	91
6. CONCLUSION .....	94
7. REFERENCES .....	96
APPENDICES .....	100
APPENDIX 1: DISCRETISATION OF FLUXES .....	100

## LIST OF FIGURES

Figure 2.1. Schematic of SIMPLE algorithm from Patankar (1980).....	8
Figure 2.2. Staggered grid.....	12
Figure 2.3. Collocated grid .....	12
Figure 3.1. Lid driven cavity.....	15
Figure 3.2. Temperature contour plots for Re=400 from Hussain (2016) obtained by ANSYS Fluent..	16
Figure 3.3. Solution domain used by Bhuiyan et al. (2017) .....	17
Figure 3.4. Velocity contours obtained by Bhuiyan et al. (2017) .....	17
Figure 3.5. Temperature contours obtained by Bhuiyan et al. (2017) .....	17
Figure 3.6. Domain used by Arani et al. (2017).....	18
Figure 3.7. Variation of heat transfer rate from Arani et al. (2017) .....	19
Figure 3.8. Streamlines and isotherm lines for a single heat source from by Arani et al. (2017) .....	20
Figure 3.9. Solution domain used by Taher et al. (2013) .....	21
Figure 3.10. T and v distributions, mid height, Taher et al. (2013) .....	21
Figure 3.11. Variation of u velocity, Re=100, dx=1/10, dy=1/10.....	24
Figure 3.12. Variation of u velocity, Re=100, dx=1/20, dy=1/20.....	24
Figure 3.13. Variation of u velocity, Re=100, dx=1/40, dy=1/40.....	24
Figure 3.14. Variation of u velocity, Re=100, dx=1/80, dy=1/80.....	24
Figure 3.15. Variation of u velocity, Re=400, dx=1/40, dy=1/40.....	25
Figure 3.16. Variation of u velocity, Re=400, dx=1/80, dy=1/80.....	25
Figure 3.17. Variation of u velocity, Re=400, dx=1/120, dy=1/120.....	25
Figure 3.18. Variation of u velocity, Re=1000, dx=1/40, dy=1/40.....	27
Figure 3.19. Variation of u velocity at mid length, Re=1000, dx=1/80, dy=1/80.....	27
Figure 3.20. Variation of u velocity at mid length, Re=1000, dx=1/120, dy=1/120.....	27
Figure 3.21. Midpoint absolute error variation with grid density, Re=100.....	28
Figure 3.22. Midpoint absolute error variation with grid density, Re=400.....	28
Figure 3.23. Midpoint absolute error variation with grid density, Re=1000.....	28
Figure 3.24. Error variation with iteration number, Re=100, dx=1/28, dy=1/28.....	29
Figure 3.25. Variation of u velocity at x=0.5, Reynolds number 100, dx=1/28, dy=1/28.....	30
Figure 3.26. Variation of v velocity at y=0.5, Reynolds number 100, dx=1/28, dy=1/28.....	30
Figure 3.27. Variation of u velocity at x=0.5, Reynolds number 100, dx=1/40, dy=1/40.....	30
Figure 3.28. Variation of v velocity at y=0.5, Reynolds number 100, dx=1/40, dy=1/40.....	30
Figure 3.29. Variation of u velocity at x=0.5, Reynolds number 100, dx=1/60, dy=1/60.....	31
Figure 3.30. Variation of v velocity at x=0.5, Reynolds number 100, dx=1/60, dy=1/60.....	31

Figure 3.31. Midpoint u velocity absolute error variation with grid density, $Re=100$ , collocated grid ....	31
Figure 3.32. Variation of temperature for Reynolds number= $400$ , $dx=dy=1/10$ , $T_{rightwall}=700$ K.....	33
Figure 3.33. Variation of density for Reynolds number= $400$ , $dx=dy=1/10$ , $T_{rightwall}=700$ K.....	33
Figure 3.34. Variation of temperature for Reynolds number= $400$ , $dx=dy=1/20$ , $T_{rightwall}=700$ K.....	34
Figure 3.35. Variation of density for Reynolds number= $400$ , $dx=dy=1/20$ , $T_{rightwall}=700$ K .....	34
Figure 3.36. Variation of temperature, Reynolds number= $400$ , $dx=dy=1/40$ , $T_{rightwall}=700$ K.....	35
Figure 3.37. Variation of density, Reynolds number= $400$ , $dx=dy=1/40$ , $T_{rightwall}=700$ K.....	35
Figure 3.38. Variation of temperature, $Re=400$ , $dx=dy=1/60$ , $T_{rightwall}=700$ K.....	35
Figure 3.39. Variation of density, $Re=400$ , $dx=dy=1/60$ , $T_{rightwall}=700$ K .....	35
Figure 3.40. Variation of temperature, $Re=1000$ , $dx=dy=1/10$ , $T_{rightwall}=700$ K.....	37
Figure 3.41. Variation of density, $Re=1000$ , $dx=dy=1/10$ , $T_{rightwall}=700$ K .....	37
Figure 3.42. Variation of temperature, $Re=1000$ , $dx=dy=1/20$ , $T_{rightwall}=700$ K.....	37
Figure 3.43. Variation of density for $Re=1000$ , $dx=dy=1/20$ , $T_{rightwall}=700$ K .....	37
Figure 3.44. Variation of temperature for $Re=1000$ , $dx=dy=1/40$ , $T_{rightwall}=700$ K.....	38
Figure 3.45. Variation of density for $Re=1000$ , $dx=dy=1/40$ , $T_{rightwall}=700$ K .....	38
Figure 3.46. Variation of temperature for $Re=1000$ , $dx=dy=1/60$ , $T_{rightwall}=700$ K.....	38
Figure 3.47. Variation of density for $Re=1000$ , $dx=dy=1/60$ , $T_{rightwall}=700$ K .....	38
Figure 3.48. Midpoint u velocity absolute error variation with grid density, $Re=400$ .....	39
Figure 3.49. Midpoint u velocity absolute error variation with grid density, $Re=1000$ .....	39
Figure 3.50. Variation of density for Reynolds number= $100$ , $dx=dy=1/10$ , $T_{rightwall}=1000$ K.....	40
Figure 3.51. Variation of temperature for Reynolds number= $100$ , $dx=dy=1/10$ , $T_{rightwall}=1000$ K.....	40
Figure 3.52. Variation of density for Reynolds number= $100$ , $dx=dy=1/20$ , $T_{rightwall}=1000$ K.....	41
Figure 3.53. Variation of temperature for Reynolds number= $100$ , $dx=dy=1/20$ , $T_{rightwall}=1000$ K.....	41
Figure 3.54. Variation of density for Reynolds number= $100$ , $dx=dy=1/40$ , $T_{rightwall}=1000$ K.....	41
Figure 3.55. Variation of temperature for Reynolds number= $100$ , $dx=dy=1/40$ , $T_{rightwall}=1000$ K.....	41
Figure 3.56. Variation of density for Reynolds number= $400$ , $dx=dy=1/10$ , $T_{rightwall}=1000$ K.....	42
Figure 3.57. Variation of temperature for Reynolds number= $400$ , $dx=dy=1/10$ , $T_{rightwall}=1000$ K.....	42
Figure 3.58. Variation of density for Reynolds number= $1000$ , $dx=dy=1/10$ , $T_{rightwall}=1000$ K.....	43
Figure 3.59. Variation of temperature for Reynolds number= $1000$ , $dx=dy=1/10$ , $T_{rightwall}=1000$ K.....	43
Figure 3.60. Variation of density for Reynolds number= $400$ , $dx=dy=1/40$ , $T_{rightwall}=1000$ K.....	43
Figure 3.61. Variation of temperature for Reynolds number= $400$ , $dx=dy=1/40$ , $T_{rightwall}=1000$ K.....	43
Figure 3.62. Variation of density for $Re=1000$ , $dx=dy=1/10$ , $T_{rightwall}=1000$ K .....	44
Figure 3.63. Variation of temperature for $Re=1000$ , $dx=dy=1/10$ , $T_{rightwall}=1000$ K.....	44
Figure 3.64. Variation of density for $Re=1000$ , $dx=dy=1/20$ , $T_{rightwall}=1000$ K .....	44
Figure 3.65. Variation of temperature for $Re=1000$ , $dx=dy=1/20$ , $T_{rightwall}=1000$ K.....	44
Figure 3.66. Variation of density for $Re=1000$ , $dx=dy=1/40$ , $T_{rightwall}=1000$ K .....	45
Figure 3.67. Variation of temperature for $Re=1000$ , $dx=dy=1/40$ , $T_{rightwall}=1000$ K.....	45

Figure 3.68. Midpoint u velocity absolute error variation with grid density, $Re=100$ , $T=1000$ K .....	45
Figure 3.69. Midpoint u velocity absolute error variation with grid density, $Re=400$ , $T=1000$ K .....	45
Figure 3.70. Midpoint u velocity absolute error variation with grid density, $Re=1000$ , $T=1000$ K .....	46
Figure 4.1. Experimental setup used by Bakke (1957) .....	48
Figure 4.2. Solution domain used by Sezai and Mohammad (1999).....	49
Figure 4.3. Domain used by Turgeon et al (1999) .....	50
Figure 4.4. Mesh used by Turgeon et al. (1999) .....	50
Figure 4.5. Skin coefficient values from Turgeon et al. (1999) .....	51
Figure 4.6. Solution domain used by Dagtekin and Oztop (2008).....	52
Figure 4.7. Flow field at $Re=250$ , $H/W=4$ , $d/W=5$ from Dagtekin and Oztop (2008).....	52
Figure 4.8. Isotherms at $Re=250$ , $H/W=6$ , $d/W=5$ from Dagtekin and Oztop (2008).....	52
Figure 4.9. Nusselt number at the bottom wall from Chou and Hung (1994).....	54
Figure 4.10. Modified Pohlhausen equation and numerical solution by Chou and Hung (1994) .....	55
Figure 4.11. Domain studied by Lorenzo et al. (2012).....	55
Figure 4.12. Nusselt number on the bottom wall from Lorenzo et al (2012) .....	57
Figure 4.13. Variation of Nusselt number with $Re$ from Lorenzo et al. (2012) .....	57
Figure 4.14. Domain used in Chung and Luo (2002).....	58
Figure 4.15. Experimental and numerical Nusselt numbers for $H/W=10$ from Chung and Luo (2002) .	59
Figure 4.16. Variation of Nusselt number with Reynolds number from Chung and Luo (2002).....	60
Figure 4.17. Vortex structure at $Re=500$ from Chung and Luo (2002) .....	60
Figure 4.18. Nusselt number for flat plate at $Re=300$ , $H/W=2$ from Tahsini and Mousavi (2012).....	61
Figure 4.19. Jet impingement cooling isotherms from Narumanchi et al. (2005) .....	61
Figure 4.20. Domain used by Shuja and Yilbas (2001) .....	62
Figure 4.21. Axial velocity variation with changing jet exit profile from Shuja and Yilbas (2001).....	63
Figure 4.22. Experimental setup used by Hadhrami et al. (2011) .....	64
Figure 4.23. Variation of Nusselt number with different geometries from Hadhrami et al. (2011).....	64
Figure 4.24. Solution domain used by Sahoo and Sharif (2004).....	65
Figure 4.25. Velocity contours (left) and isotherms from Sahoo and Sharif (2004).....	65
Figure 4.26. Nusselt number at the bottom wall from Sahoo and Sharif (2004) .....	66
Figure 4.27. Density isolines for the double impinging flow, $Re=50$ , $dx=dy=1/40$ , $v_{jet}=-1$ m/s.....	68
Figure 4.28. Isotherms for the double impinging flow, $Re=50$ , $dx=dy=1/40$ , $v_{jet}=-1$ m/s.....	68
Figure 4.29. Density isolines for the double impinging flow, $Re=50$ , $dx=dy=1/80$ , $v_{jet}=-1$ m/s.....	69
Figure 4.30. Isotherms (Kelvin) for the double impinging flow, $Re=50$ , $dx=dy=1/80$ , $v_{jet}=-1$ m/s.....	69
Figure 4.31. Velocity vector for the double impinging flow, $Re=50$ , $dx=dy=1/40$ .....	69
Figure 4.32. Velocity contours for the double impinging jet flow, $Re=50$ , $dx=dy=1/80$ .....	70
Figure 4.33. Isotherms (Kelvin) for the double impinging flow, $Re=100$ , $dx=dy=1/40$ , $v_{jet}=-2$ m/s.....	71
Figure 4.34. Density isolines for the double impinging flow, $Re=100$ , $dx=dy=1/40$ , $v_{jet}=-2$ m/s.....	71



Figure 4.35. Isotherms (Kelvin) for the double impinging jet flow, $Re=100$ , $dx=dy=1/80$ , $v_{jet}=-2$ m/s ..	71
Figure 4.36. Density isolines for the double impinging flow, $Re=100$ , $dx=dy=1/80$ , $v_{jet}=-2$ m/s.....	71
Figure 4.37. Velocity contours for the double impinging jet flow, $Re=100$ , $dx=dy=1/40$ , $v_{jet}=-2$ m/s....	72
Figure 4.38. Velocity contours for the double impinging jet flow, $Re=100$ , $dx=dy=1/80$ , $v_{jet}=-2$ m/s....	72
Figure 4.39. Density isolines for the double impinging flow, $v_{jet}=-1$ m/s, $dx=dy=1/40$ , $w=0.2*L$ .....	73
Figure 4.40. Isotherms for the double impinging jet flow, $v_{jet}=-1$ m/s, $dx=dy=1/40$ , $w=0.2*L$ .....	73
Figure 4.41. Density isolines for the double impinging flow, $v_{jet}=-1$ m/s, $dx=dy=1/40$ , $w=0.02*L$ .....	73
Figure 4.42. Isotherms for the double impinging jet flow, $v_{jet}=-1$ m/s, $dx=dy=1/40$ , $w=0.02*L$ .....	73
Figure 4.43. Velocity contours for the double impinging jet flow, $v_{jet}=-1$ m/s, $dx=dy=1/40$ , $w=0.2*L$ ....	74
Figure 4.44. Velocity contours for the double impinging jet flow, $v_{jet}=-1$ m/s, $dx=dy=1/40$ , $w=0.02*L$ ..	74
Figure 4.45. Variation of Nusselt number at impingement wall for $Re=100$ .....	76
Figure 4.46. Variation of Nusselt number at impingement wall for $Re=300$ , $102 \times 42$ grid.....	77
Figure 4.47. Variation of Nusselt number at impingement wall for $Re=300$ , $102 \times 62$ grid.....	77
Figure 4.48. Variation of Nusselt number at impingement wall for $Re=300$ , $102 \times 82$ grid.....	77
Figure 4.49. Variation of Nusselt number at impingement wall for $Re=300$ , $102 \times 102$ grid.....	77
Figure 4.50. Variation of temperature for single impinging jet flow, $Re=300$ , $102 \times 102$ grid .....	78
Figure 4.51. Variation of density for single impinging jet flow, $Re=300$ , $102 \times 102$ grid .....	78
Figure 4.52. Velocity field for single impinging jet flow, $Re=300$ , $102 \times 102$ grid .....	79
Figure 5.1. Schematic of Genetic Algorithm by Gupta (2016) .....	81
Figure 5.2. Problem with a global minimum .....	81
Figure 5.3. Problem with a global and local minimum .....	82
Figure 5.4. Flowchart of the genetic algorithm .....	83
Figure 5.5. Single impinging jet flow outline of domain.....	91

## LIST OF TABLES

Table 3-1 Average Nusselt number for different grids by Arani et al. (2017) .....	19
Table 3-2 Solutions performed for lid driven cavity problem .....	22
Table 4-1 Simplified viscosity and temperature relations from Turgeon et al. (1999) .....	51
Table 4-2 Test cases used by Chung and Luo (2002) .....	58
Table 4-3 Modelling parameters used for double slot impinging jet flow .....	67
Table 4-4 Modelling parameters used for single impinging jet flow .....	75
Table 5-1 Turbulence paramaters for backward facing step from Fabritius (2014) .....	82
Table 5-2 Optimisation parameter values, the first lid driven cavity problem .....	84
Table 5-3 Optimum solution for target mid temperature .....	84
Table 5-4 Optimisation parameter values, the second lid driven cavity problem .....	85
Table 5-5 Optimum solution for target mid temperature, lid velocity as a optimization parameter.....	85
Table 5-6 Optimisation parameter values, the third lid driven cavity problem.....	86
Table 5-7 Optimum solution for target mid temperature using heat sink as an optimization parameter	86
Table 5-8 Optimisation variable intervals .....	87
Table 5-9 Genetic algorithm settings .....	87
Table 5-10 Optimisation results .....	88
Table 5-11 Optimum momentum and pressure iterations for optimizing computation time .....	88
Table 5-12 Optimisation parameter intervals.....	89
Table 5-13 Genetic algorithm solver settings for collocated grid.....	89
Table 5-14 Optimum under-relaxation parameters for optimizing computation time.....	90
Table 5-15 First impinging jet optimisation parameter value intervals.....	91
Table 5-16 First impinging jet optimisation parameter values .....	91
Table 5-17 Second impinging jet optimisation parameter value intervals.....	92
Table 5-18 Second impinging jet optimisation parameter values .....	92

## LIST OF SYMBOLS AND ABBREVIATIONS

### Symbols

$\alpha_u$	Under-relaxation factor for u component of velocity
$\alpha_v$	Under-relaxation factor for v component of velocity
$\alpha_p$	Under-relaxation factor for pressure
k	Thermal conductivity
$\mu$	Dynamic viscosity
Nu	Nusselt number
$Nu_s$	Stagnation Nusselt number
P	Pressure
$P^*$	Non-dimensionalized pressure
Pe	Peclet number
Pr	Prandtl number
$\rho$	Density
Re	Reynolds number
su	Source term for u momentum equation
sv	Source term for v momentum equation
sT	Source term for temperature
t	Time
T	Temperature
$\Theta$	Non-dimensionalized temperature
u	X component of velocity
$u^*$	X component of velocity, non-dimensionalized
v	Y component of velocity
$v^*$	Y component of velocity, non-dimensionalized
$V_{cell}$	Volume of computational cell
W	Slot width for impinging jet flow
$X^*$	Non-dimensionalized x dimension
$Y^*$	Non-dimensionalized y dimension
z	Compression factor

## **Abbreviations and Acronyms**

CDS                    Central differencing scheme

QUICK Quadratic Upstream Interpolation for Convective Kinematics

SIMPLE              Semi Implicit Method for Pressure Linked Equations

UDS                   First order upwind scheme

# 1. INTRODUCTION

In this thesis, in-house codes have been developed to solve incompressible and compressible fluid flows. Additionally, the developed codes have been matched with genetic algorithm for optimization so that they can be better utilised in design studies.

Incompressible flow solutions are generally carried out with a pressure based solver in the literature. Patankar (1980) has proposed the SIMPLE method to solve the flow field using corresponding corrections to pressure and velocity. Although it is useful, the assumption of incompressibility cannot be used for a variety of flows. For example low-speed flows with significant temperature variations are compressible due to density variations caused by heat addition. Flows involving combustion are one of the primary examples of such flow fields. In this study such problems have been investigated numerically with developed in-house codes and tested on well-accepted benchmark problems.

On the other hand, with the density based solvers, solutions for the low speed compressible viscous flows can be implemented with the addition of artificial terms. For example, Chorin (1968) added an artificial pressure derivative term to the continuity and momentum equations to overcome very fast propagation of pressure variation and related numerical difficulties. The work of Chorin (1968) led to a number of preconditioned density based solvers.

Low-speed flows with significant temperature variations can also be solved with pressure based finite volume methods without the addition of artificial terms, which is the focus of this study. In the case of compressibility, the effectiveness of pressure based method is reduced compared to a purely incompressible flow simulation. To alleviate this problem, a preconditioning is applied on the pressure based solver with the use of preliminary incompressible flow solution in the thesis. The idea is to march with an incompressible solver first, which requires less computational time, then switch to a compressible solver. After development, the solver has been tested for the lid driven cavity and impinging jet flow problems.

The idea is mainly inspired by the computational aerodynamics analysis procedure for wings, which is performed in two steps. First, an incompressible solution is performed for the analysis and design of the wings. Then for more accurate results, compressible flow solution is utilized. Nastase (2008) has described the procedure in detail. The main objective in this methodology is to merge two separate solution codes/algorithms to a single code/algorithm.

It has been observed that the preconditioning of the compressible flow solution with the incompressible solution enhances the stability of the solution and is able to reduce the computational time. The use of pseudo-transient under-relaxation for momentum equations have been realised to enhance the compatibility of incompressible and compressible flow solutions and increase the stability of the solution algorithm.

Additionally, the in-house code developed has been used for optimisation studies. As a rule of thumb, an in-house code (flow solver) is much easier to use along with optimization codes compared to commercial solvers. For commercial flow solvers matching the flow solver with the optimization code requires scripting. This necessitates reading specific lines on the output files of the program which can cause problems and increase the overall solution time due to writing and deleting thousands of lines, and processing them. Therefore, usage of the in-house code leads to a more practical way of optimisation.

The optimisation procedure has been applied to a variety of problems. For optimisation, genetic algorithm has been utilized. Solver variables, i.e., under-relaxation parameters, have been optimised with the use of optimisation procedures. Generally, solver settings are set based on recommended values in literature. Patankar (1980), Ferziger and Peric (2002) have proposed different under-relaxation values for pressure and velocity for SIMPLE solutions. The selection of under-relaxation parameters is in general based upon common best practices. To investigate this problem, an optimization procedure has been applied to the solver settings to optimize the selection of under-relaxation parameters. As a benchmark

optimisation problem, lid driven cavity problem with a heat sink has also been solved. Heat sink location and boundary conditions for temperature and velocity have been selected as optimisation parameters to obtain a specific temperature value at the middle of the domain. It has been shown that heat sink location and lid velocity can be optimized. Finally, impinging jet flow problem has been investigated to optimize maximum stagnation point Nusselt number at the impingement wall. It has been shown that due to thermal-fluid interactions, maximum stagnation point Nusselt number occurs at an impingement wall temperature that is lower than the maximum value allowed.

In summary, this thesis aims to develop a pressure based compressible flow Navier Stokes solver that utilize faster convergence with the use of embedded incompressible solver. The lid driven cavity flow problem, single and double impinging jet problems have been studied in incompressible and compressible flow regimes. Furthermore, different grid arrangements (staggered and collocated) have been utilized in the solutions.

## 2. THEORY

### 2.1 EQUATIONS SOLVED

Navier Stokes equations for 2D laminar flows are given below. For steady flows, time derivative terms drop.

Continuity equation:

$$\frac{\partial \rho}{\partial t} + \frac{\partial(\rho u)}{\partial x} + \frac{\partial(\rho v)}{\partial y} = 0 \quad (2.1)$$

Momentum equations are given next.

x-momentum equation:

$$\frac{\partial(\rho u)}{\partial t} + \frac{\partial(\rho uu)}{\partial x} + \frac{\partial(\rho uv)}{\partial y} = \frac{-\partial p}{\partial x} + \frac{\partial}{\partial x} \left( \mu \frac{\partial u}{\partial x} \right) + \frac{\partial}{\partial y} \left( \mu \frac{\partial u}{\partial y} \right) + su \quad (2.2)$$

y-momentum equation:

$$\frac{\partial(\rho v)}{\partial t} + \frac{\partial(\rho uv)}{\partial x} + \frac{\partial(\rho vv)}{\partial y} = \frac{-\partial p}{\partial y} + \frac{\partial}{\partial x} \left( \mu \frac{\partial v}{\partial x} \right) + \frac{\partial}{\partial y} \left( \mu \frac{\partial v}{\partial y} \right) + sv \quad (2.3)$$

For compressible flows, the following two equations are also required. In the energy equation, viscous dissipation term has been assumed to be negligible. Energy equation:

$$\frac{\partial(\rho T)}{\partial t} + \frac{\partial(\rho u T)}{\partial x} + \frac{\partial(\rho v T)}{\partial y} = \frac{\partial}{\partial x} \left( \frac{k}{C_p} \frac{\partial T}{\partial x} \right) + \frac{\partial}{\partial y} \left( \frac{k}{C_p} \frac{\partial T}{\partial y} \right) + sT \quad (2.4)$$

Equation of state:

$$\rho = \frac{P}{zRT} \quad (2.5)$$

Here, the parameter  $z$  is the compression factor that can be defined as constant or as a function of thermodynamic properties ( $P$ ,  $T$ ). In the thesis, constant  $z$  value has been used.

Compressible form of Navier Stokes equations are needed in high speed flows as well as in flows involving combustion where significant temperature variations occur inside the solution domain.



## **2.2 FINITE VOLUME METHOD WITH DIFFERENT FLUX CALCULATION SCHEMES**

Due to its flexibility compared to finite difference method, and robustness compared to finite element method, finite volume method has gained popularity for the solution of Navier Stokes equations. In the finite volume approach, the cells or control volumes with associated faces are defined inside the solution domain, whereas for the finite difference approach grid points are defined without a face definition. Fluxes are calculated at the cell faces and mass, momentum and energy balances are attempted to be reached at all cells. For each cell and for each equation (mass, momentum, energy) the following condition is sought:

$$(\text{Net transport by convection}) + (\text{Net transport by diffusion}) + (\text{generation term}) = 0$$

Methods of obtaining fluxes, hence the net transport terms should be discussed next.

### **2.2.1 Diffusive Fluxes**

For the diffusive fluxes, central differencing scheme (CDS) can be utilised. The advantages of central difference method are the relative ease of coding and relatively lower truncation errors.

### **2.2.2 Convective Fluxes**

For the discretization of the convective flux terms, different techniques (central difference, upwind, hybrid, power law, MUSCL, QUICK) have been studied in the literature.

Central differencing scheme (CDS) is in general not practical for the convective flux. It yields numerical oscillations and instability especially when the advective fluxes are large compared to diffusive fluxes, around regions of high gradients and rapid changes.

1<sup>st</sup> order upwind scheme (UDS) can generally eliminate these numerical oscillations, but results in higher truncation and dissipative errors compared to central differencing approach.

Hybrid method, which has been developed by Spalding (1972), combines UDS and CDS. It is better in terms of overall numerical accuracy compared to UDS and CDS. Unless otherwise stated, , hybrid scheme has been utilized for the discretization of convective terms and central differencing scheme has been utilized for the discretization of diffusive terms throughout the thesis.

The details of 1<sup>st</sup> order upwind scheme and hybrid method are given in Appendix 1.

Power law method has been developed by Patankar (1980). The method is based on the 1D solution of the convection diffusion equation but is expanded to higher dimensions. It is numerically very stable and also effective in mitigating false diffusion error.

MUSCL method which has been established by van Leer (1979) has low truncation errors and causes low level of numerical oscillations in general. However in the case of utilizing marginally different element sizes in the same mesh, error of the method significantly increases.

QUICK scheme, which was introduced by Leonard (1979), uses a 3-point upstream weighted quadratic interpolation for the cell face values. It gives a third order spatial accuracy. But it has higher stability problems compared to the first order upwind scheme and is more difficult to apply near the boundaries.

### 2.3 SOLUTION OF PRESSURE EQUATION

Solution of pressure equation is carried out with a method known as “Semi Implicit Method for Pressure Linked Equations (SIMPLE)” as developed by Patankar (1980). The method devises a pressure correction from continuity equation. After that, pressure field is corrected with Equation (2.6) and velocity field is corrected with Equation (2.7).

$$p^{k+1} = p^k + \alpha_p * p' \quad (2.6)$$

$$(u, v)^{k+1} = (u, v)^k + (\alpha_u, \alpha_v) * (u, v)' \quad (2.7)$$

SIMPLE Algorithm:

- Set the boundary conditions.
- Initialize,  $u, v, P$
- Solve the discretized momentum equation to compute the intermediate velocity field.
- Compute the uncorrected mass fluxes at faces.
- Solve the pressure correction equation to produce cell values of the pressure correction,  $p'$ .
- Update the pressure field with Equation (2.6) where  $\alpha_p$  is the under-relaxation factor for pressure.
- Update velocity field with Equation (2.7) where  $\alpha_u$  and  $\alpha_v$  are the under-relaxation factors for velocities, and  $u', v'$  are velocity corrections.
- Loop until mass continuity residual at each cell and other residuals drop below a specified tolerance.

The main steps involved in the method are listed below and shown in Figure 2.1.

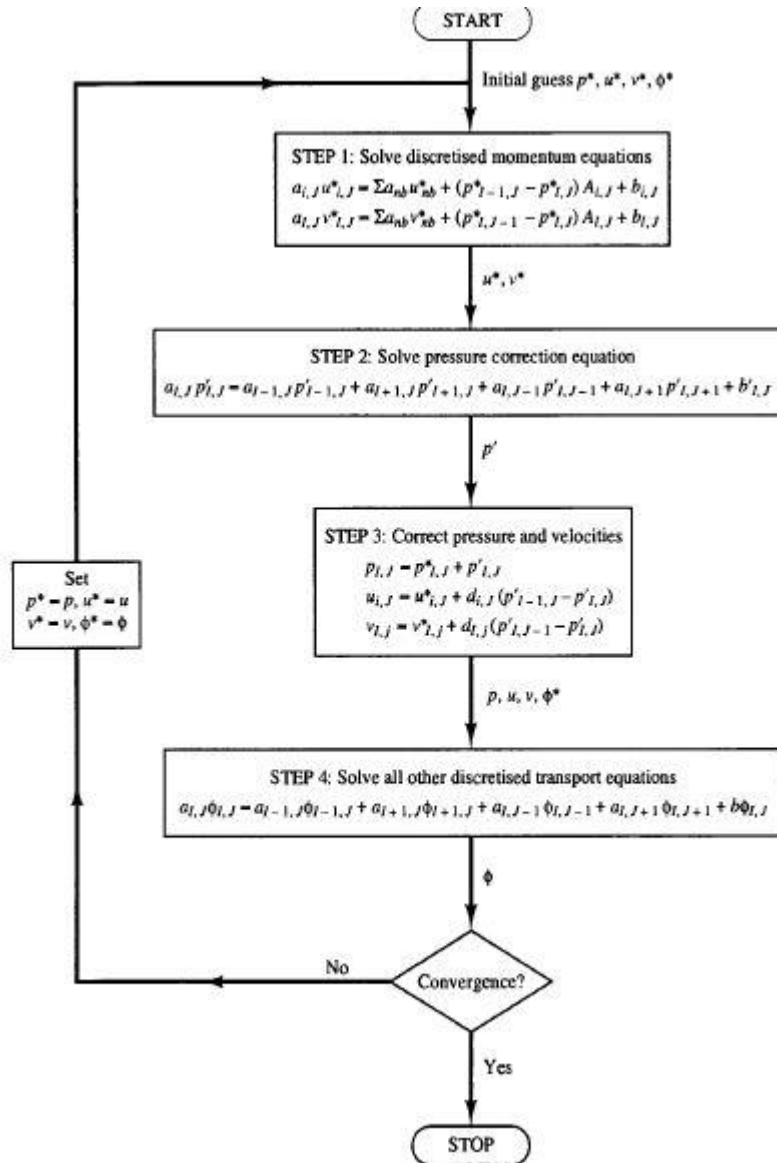


Figure 2.1. Schematic of SIMPLE algorithm from Patankar (1980)

SIMPLE can be used for both incompressible and compressible flows and this has been demonstrated in the present study. As in other iterative techniques, to execute SIMPLE, a convergence criterion is required. The following convergence criterion has been employed after extensive numerical experimentation.

In the first iteration of SIMPLE, a reference mass residual is obtained as described below. Optimizing the error criterion for pressure correction equation is very important for SIMPLE solutions since at least half of the solution time is spent for the pressure correction equation.

Pseudocode for pressure correction error criterion:

```

Initialize ratiop
while ratiop>0.25
    ratiop=norm(Massresiduali- Massresiduali-1)/norm (Massresiduali - Massresidual0)
    Solve Pressure correction equation
End
    
```

In the pseudocode, norm represents the infinity norm or Frobenius norm. The value of 0.25 is not mandatory. But reducing this value results in too many iterations, and increasing it yields a very small number of iterations.

Using a fixed mass residual value as an error criterion (such as “frobenius norm of mass residual less than  $10^{-3}$ ”) for pressure correction equation is not the optimum method. Because it requires too many pressure correction loops during the first phase of the solution and too low number of pressure correction loop counts towards the final phase of the solution (close to convergence). Instead, using a relative error criterion such as the one described above gives almost constant number of iterations during the entire solution and is much closer to the optimum approach.

### **2.3.1 Definition of Under-relaxation Terms for Momentum and Pressure Terms**

With SIMPLE approach, under-relaxation should be introduced to the u, v, and P values. The under-relaxation employed to u, v and under-relaxation employed to the pressure is somewhat interrelated. Through numerical experiments and taking the values used in the literature into account, the optimum under-relaxation factors have been sought.

The under-relaxation can be introduced in two different ways for the momentum equations. In the first approach, constant under-relaxation values (say,  $\alpha_u = \alpha_v = 0.5$ ) are introduced to reach the steady state solution.

Malalasekera, Versteeg (2010) introduces the following equation for the first approach:

$$(a_{i,j}/\alpha_u) * u_{i,j} = \sum a_{nb} u_{nb} + (p_{I-1,J} - p_{I,J}) A_{i,j} + b_{i,j} + [(1 - \alpha_u) \frac{a_{i,j}}{\alpha_u}] u_{i,j}^{n-1} \quad (2.8)$$

In the second approach, (pseudo-transient approach) even steady solution is performed using a pseudo time step. In this approach, Instead of introducing a fixed under-relaxation factor for each cell, different under-relaxation factors are used for each cell using a pseudo time term. The added pseudo-transient term is represented by  $S_t = \rho_{i,j} * \frac{V_{cell}}{\Delta t} * u_{i,j}^{l-1}$ , where l-1 denotes previous pseudo time. For the pseudo-transient analysis of steady state problem, momentum equation becomes:

$$(a_{i,j} + \rho_{i,j} * \frac{V_{cell}}{\Delta t}) * u_{i,j} = \sum a_{nb} u_{nb} + (p_{I-1,J} - p_{I,J}) A_{i,j} + b_{i,j} + S_t \quad (2.9)$$

The second approach is especially useful for recirculating or rapidly changing flows where stability and convergence can be more problematic.

Pseudo time increment should be selected such that fluid should have a “passage time allowance” for each cell.

$$\Delta t < \frac{(dx,dy)}{u_{cell} * 0.3} \quad (2.10)$$

$\Delta t$  should be constant for each cell. So that, either finding the maximum cell velocity or (if known) prescribing a maximum velocity could be done. For the lid driven cavity problem:

$$\Delta t = \frac{dx}{u_{toplid}} \text{ can be utilised.}$$

$$(a_{i,j} + \frac{\rho_{i,j}^0 \Delta V}{\Delta t}) u_{i,j} = \sum a_{nb} u_{nb} + (p_{I-1,J} - p_{I,J}) A_{i,j} + b_{i,j} + \frac{\rho_{i,j}^0 \Delta V}{\Delta t} u_{i,j}^0 \quad (2.11)$$

Both under-relaxation approaches described above has been used for numerical solutions and data from numerical solutions have been obtained. Selection of pseudo the transient approach has been preferred for the preconditioned compressible simulations and high Reynolds number incompressible solutions.

## **2.4 SELECTION OF ITERATIVE TECHNIQUE**

For the solution of transport variables, direct approach, i.e., inverting a huge coefficient matrix to obtain the values of transport variables, is very time consuming and could lead to stability problems. Instead, iterative techniques are employed.

One common iterative technique is Gauss-Seidel method. In this method, new estimates of the transport variables are used whenever they are available.

Another technique is based on the tridiagonal matrix algorithm. In this technique, solution is performed on unidirectional (horizontal or vertical direction) sweeps. If horizontal sweeps are performed, the points above and below the point of interest are transferred to source term. Similarly, the points left and right to the point of interest are transferred to source term for the vertical sweeps. If, number of grid points that influence a point is limited to 2 on the horizontal direction, a tridiagonal matrix solver can be easily used. After solving this "line" using the TDMA, next horizontal line is solved and so on. One advantage of TDMA over Gauss Seidel method is that the definition of error criteria for the TDMA is much more practical.

## **2.5 STAGGERED GRID**

Staggered meshing technique is developed by Harlow and Welch (1965). It stores  $u$ ,  $v$ , and  $P$  values at different nodes to avoid pressure velocity decoupling. Scalar variables (pressure, density, turbulence kinetic energy, temperature etc.) are stored at a common mesh point. Vector quantities on the other hand, are stored at cell centers.

The disadvantage of the method is the relatively higher difficulty in coding compared to collocated grid, especially for complex geometries. The staggered grid is shown schematically in Figure 2.2.

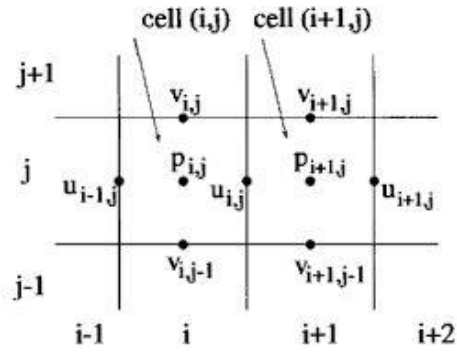


Figure 2.2. Staggered grid

### 2.6 COLLOCATED GRID

Rhie and Chow (1982) proposed a non-staggered grid arrangement for velocity components. In this, pressure, and velocity components are calculated at the same location. Collocated grid is shown schematically below in Figure 2.3.

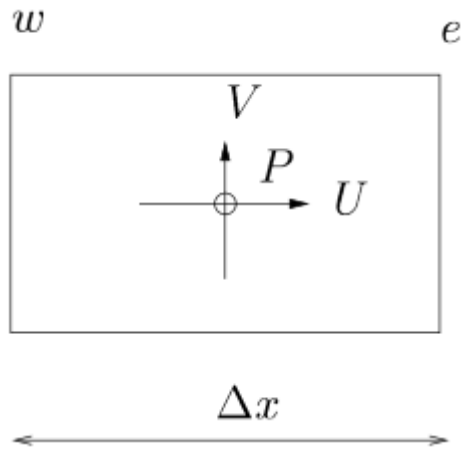


Figure 2.3. Collocated grid

To avoid non-realistic pressure solutions appearing as the solution of the problem (known as the checkerboard pressure field), Rhie and Chow (1982) introduced a momentum interpolation to the solution.



In this formulation, velocities at the cell faces are calculated according to the formula given by Equations (2.12) to (2.14).

$$u_e = \frac{\alpha_u}{(A_P)_e} * (\sum_i A_i u_i + B_p) - \frac{\alpha_u}{(A_P)_e} * \Delta y (P_E - P_P) \quad (2.12)$$

$$\left(\frac{1}{A_P} \sum_i A_i u_i + B_p\right)_e = f_e^+ \left(\frac{1}{A_P} \sum_i A_i u_i + B_p\right)_E + (1 - f_e^+) * \left(\frac{1}{A_P} \sum_i A_i u_i + B_p\right)_P \quad (2.13)$$

$$\frac{1}{(A_P)_e} = \frac{f_e^+}{(A_P)_E} + (1 - f_e^+) * \frac{1}{(A_P)_P} \quad (2.14)$$

Where  $f_e^+$  is an interpolation factor defined by

$$f_e^+ = \frac{\Delta x_P}{2\delta x_e} \quad (2.15)$$

For an equally spaced grid, (2.12) simplifies to:

$$\frac{1}{(A_P)_e} = \frac{0.5}{(A_P)_E} + \frac{0.5}{(A_P)_P} \quad (2.16)$$

Considering the equations given above, instead of using the arithmetic average of velocities at the cell interface, a modified interface velocity is calculated that is affected by the pressure distribution.

Majumdar (1988) modified the original Rhie-Chow formulation to remove the effect of underrelaxation in the calculation of cell face velocities. Cell face velocity calculation given by Majumdar (1988) is:

$$u_e = (1 - \alpha_u) * u_{e,old} + \alpha_u * (0.5 * u(i + 1, j) + 0.5 * u(i, j) - \frac{dy}{a_{pe}} * (P \text{ term})) \quad (2.17)$$

P term is specified by the Rhie-Chow approximation as usual. Similar expressions hold for the other cell face velocities.

Choi (1999) further modified the original Rhie-Chow formulation to remove the effect of under-relaxation and time step size in the calculation of cell face velocities. Here,  $S_1$  is the computation from previous iteration step and  $S_2$  is the computation

from previous time step. The equations proposed by Choi (1999) are given by Equations (2.18) to (2.20).

$$u_e = \frac{\alpha_u}{(A_P)_e} * (\sum_i A_i u_i + B_p) - \frac{\alpha_u}{(A_P)_e} * \Delta y (P_E - P_P) + S_1 + S_2 \quad (2.18)$$

$$S_1 = (1 - \alpha_u) * (u_e^{k-1} - f_e^+ u_E^{k-1} - (1 - f_e^+) f_e^+ u_P^{k-1}) \quad (2.19)$$

$$S_2 = \left( \alpha_u * \frac{\rho}{\Delta t} \right) * \left( (\Delta V)_e * \frac{u_e^{n-1}}{A_P^u} - f_e^+ * (\Delta V)_E * \frac{u_E^{n-1}}{A_P^u} - (1 - f_e^+) * (\Delta V)_P * \frac{u_P^{n-1}}{A_P^u} \right) \quad (2.20)$$

In the unsteady compressible formulation with collocated grid, formulation of Choi (1999) has been implemented throughout the thesis.

### 3. PROBLEM OF INTEREST 1- LID DRIVEN CAVITY PROBLEM

#### 3.1 LITERATURE SURVEY FOR THE PROBLEM

Lid driven cavity is one of the benchmark problems for CFD code validation. The problem usually involves a moving top lid and three stationary walls. The motion of the lid creates a complex velocity field inside the domain. The problem has been studied thoroughly in the literature. The problem does not require a complex meshing procedure but relatively dense meshes are required due to vortex motions. The velocity field is highly dependent on the Reynolds number.

For the incompressible case, the results obtained have been compared with the results from Ghia et al. (1982). Reynolds numbers of 100, 400 and 1000 have been studied. It is worth mentioning that the problem can be studied above  $Re=1000$ . However, the physical meaning of the numerical solution degrades with a laminar simulation as the flow field becomes turbulent and the numerical model for the laminar flow loses its accuracy at high Re numbers. Figure 3.1 shows the basic geometry of the lid driven cavity flow.

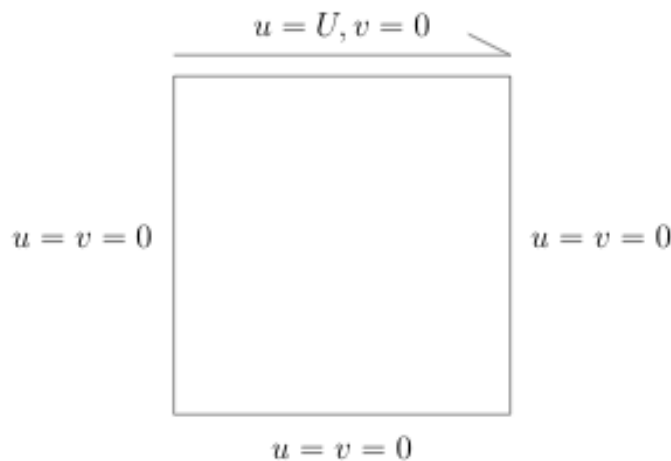


Figure 3.1. Lid driven cavity

As the Reynolds number increases, a denser mesh should be utilized to obtain an accurate result in this problem. Due to circulatory nature of the flow, convergence of the transport equations for the lid driven cavity problem is more challenging compared to unidirectional type of flows, e.g., nozzle flow.

The problem has also been investigated for the compressible flow case in the literature. For example, Shah et al. (2007) has developed a solution for equal wall temperatures and with flow on the two opposite boundaries.

Hussain (2016) solved the compressible Navier Stokes equations for lid driven cavity problem where he used adiabatic thermal boundary conditions. The initial thermal condition is selected as uniform at 300 Kelvins. The solution has been performed for various Reynolds numbers, ranging from 100 to 1000. One of the representative solution is shown in Figure 3.2.

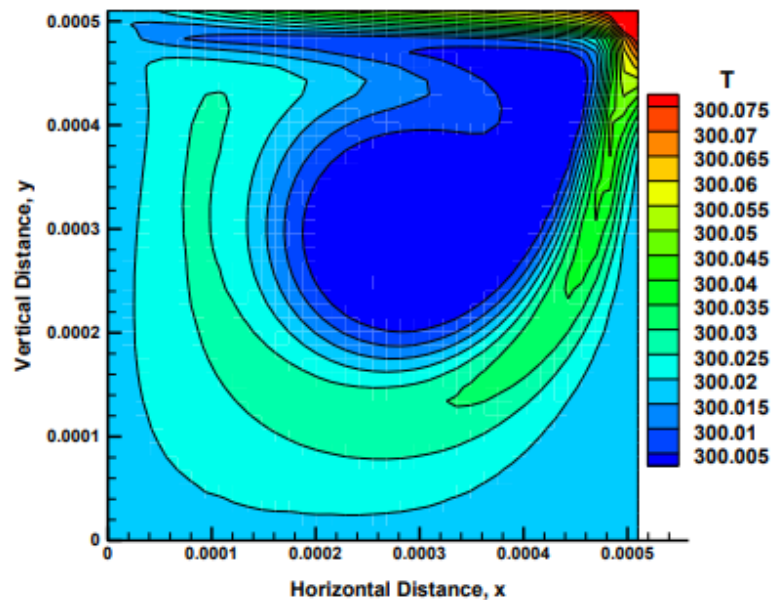


Figure 3.2. Temperature contour plots for Re=400 from Hussain (2016) obtained by ANSYS Fluent

Bhuiyan et al. (2017) studied the lid driven cavity problem with discrete heat source and sink pairs. He used high and low temperature regions on the cavity boundaries. The remaining sections of the boundaries are set to adiabatic conditions. They used non-dimensional form of the laminar steady state Navier Stokes equations and the discretization is made using Galerkin weighted residual formulation of finite-element method. Solution have been performed for Re=100. Figure 3.3 shows the domain used in their study.

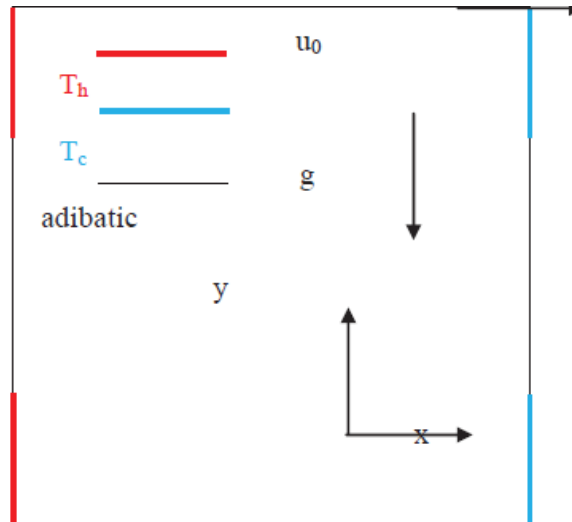


Figure 3.3. Solution domain used by Bhuiyan et al. (2017)

Figure 3.4 and Figure 3.5 show the velocity and temperature contours obtained from the reference study by Bhuiyan et al. (2017). As expected, temperature contours get denser around the isothermal boundary parts and the temperature values in the domain close to the isothermal boundaries get closer to the fixed values in the boundary.

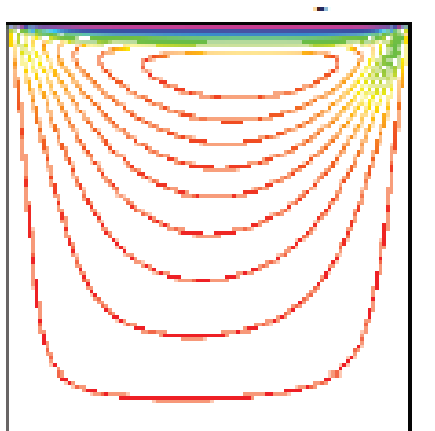


Figure 3.4. Velocity contours obtained by Bhuiyan et al. (2017)

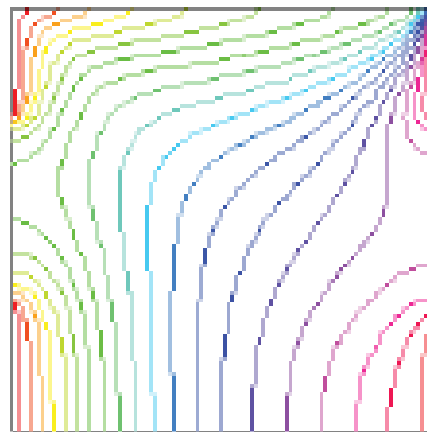


Figure 3.5. Temperature contours obtained by Bhuiyan et al. (2017)

Arani et al. (2017) studied fluid flow and heat transfer in a lid driven cavity. They used discrete heat sources. Steady-state, laminar continuity, momentum and energy

equations in Cartesian coordinates were used. In their solution, the non-dimensional form of Navier Stokes equations and a pressure-based solver utilizing SIMPLER algorithm has been employed.

Arani et al. (2017) used a domain as given in Figure 3.6. The right wall is kept at a fixed temperature. The bottom and top walls are adiabatic. The left wall is partially adiabatic and the left wall has discrete heat sources on it.

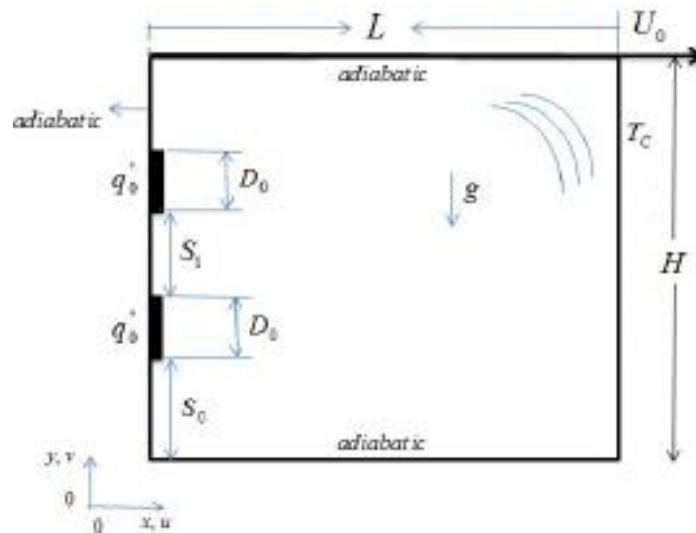


Figure 3.6. Domain used by Arani et al. (2017)

Nusselt number variation on the heat source surface for different grids has been studied to ensure grid independence. It was found that after reaching a grid size of 101x121, relative change in the Nusselt number decreases. The Nusselt number variation with grid size is shown in Table 3-1.

Table 3-1 Average Nusselt number for different grids by Arani et al. (2017)

Grid size	Average Nusselt number
101x101	654.2
111x101	801.2
101x121	879.2
101x131	907.2

Arani et al. (2017) then searched the optimal location for a single discrete heat source on the left wall to maximize the heat transfer rate. The search for the optimal location was based on a complete exploration of the possible solutions. So, in essence no optimization algorithm has been employed. Heat transfer parameter has been defined as follows:

$$C = q * L_{\text{source}} / (k * (T_{\text{max}} - T_c)) \quad (3.1)$$

The variation of parameter C with heat source location is given in Figure 3.7.

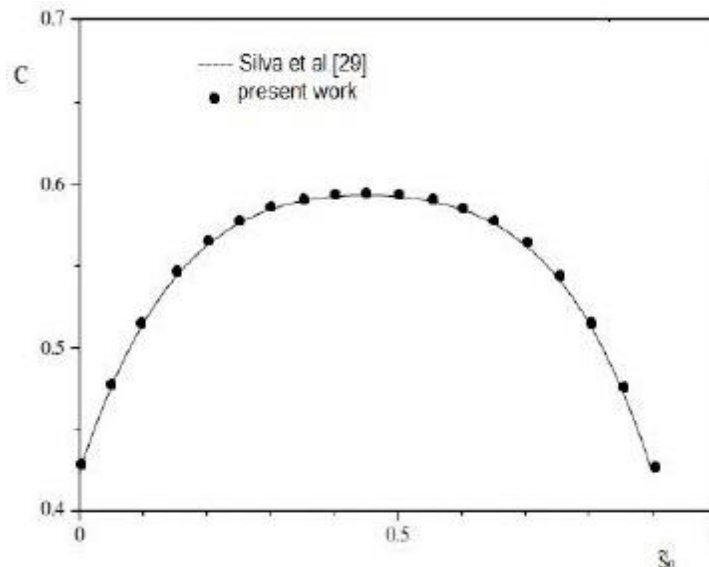


Figure 3.7. Variation of heat transfer rate from Arani et al. (2017)

For a single heat source, streamline patterns and isotherm lines have been obtained. By Arani et al. (2017). These are illustrated in Figure 3.8. Effect of heat source on the isotherm lines is evident. Effects of temperature variation in the domain on the streamline patterns are not clearly observed.

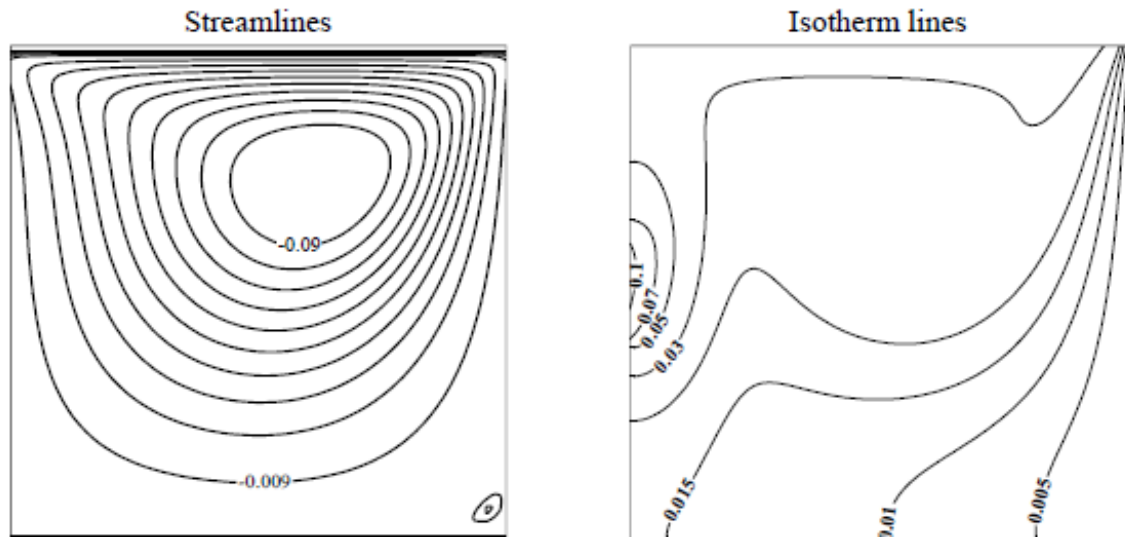


Figure 3.8. Streamlines and isotherm lines for a single heat source from by Arani et al. (2017)

Taher et al. (2013) studied the heated lid driven cavity problem using Lattice Boltzmann technique. The domain is shown below. A heat source is located at the bottom wall. The left and right walls are at fixed temperatures. The top wall is insulated. The domain utilized is illustrated in Figure 3.9.



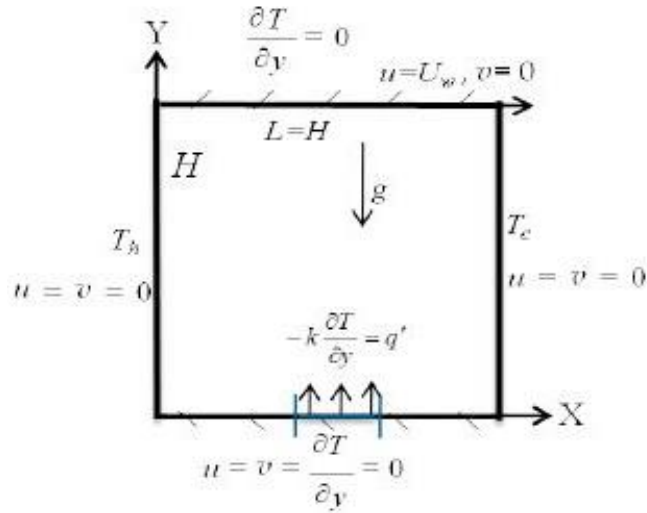


Figure 3.9. Solution domain used by Taher et al. (2013)

Different grid sizes of 80×81, 100×100, 120×120 and 150×150 have been studied and the effect of grid resolution on the results have been observed. These are illustrated in Figure 3.10.

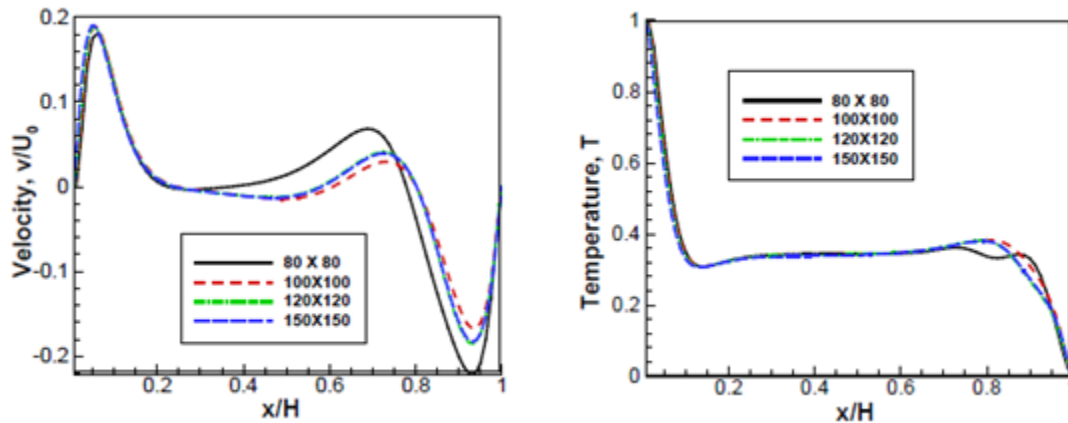


Figure 3.10. T and v distributions, mid height, Taher et al. (2013)

In the next sections, lid driven cavity problem has been investigated under incompressible and compressible flow assumption with different grid resolutions and grid settings. Primary Reynolds numbers of interest are between 100-1000. Results obtained have been compared with those found in the literature whenever such results are available.

### 3.2 RESULTS FOR LID DRIVEN CAVITY PROBLEM

The flow codes written are around 4000 lines overall. Results at different Reynolds numbers, different grid densities and different right wall temperatures (for the compressible case) have been illustrated in the following sections. Hybrid method has been utilised for the incompressible solutions. The cases studied are summarized in Table 3-2.

Table 3-2 Solutions performed for lid driven cavity problem

<b>Problem No</b>	<b>Solver Type</b>	<b>Grid Type</b>	<b>Grid Density</b>	<b>Re</b>	<b>T (Kelvin) at right BC</b>
1	Incompressible	Staggered	10x10	100	-
1	Incompressible	Staggered	20x20	100	-
1	Incompressible	Staggered	40x40	100	-
1	Incompressible	Staggered	80x80	100	-
2	Incompressible	Staggered	40x40	400	-
2	Incompressible	Staggered	80x80	400	-
2	Incompressible	Staggered	120x120	400	-
3	Incompressible	Staggered	40x40	1000	-
3	Incompressible	Staggered	80x80	1000	-
3	Incompressible	Staggered	120x120	1000	-
4	Incompressible	Collocated	28x28	100	-
4	Incompressible	Collocated	40x40	100	-
4	Incompressible	Collocated	60x60	100	-
4	Incompressible	Collocated	80x80	100	-
5	Compressible	Staggered	10x10	400	700
5	Compressible	Staggered	20x20	400	700
5	Compressible	Staggered	40x40	400	700
5	Compressible	Staggered	60x60	400	700
6	Compressible	Staggered	10x10	1000	700
6	Compressible	Staggered	20x20	1000	700
6	Compressible	Staggered	40x40	1000	700

6	Compressible	Staggered	60x60	1000	700
7	Compressible	Staggered	10x10	100	1000
7	Compressible	Staggered	20x20	100	1000
7	Compressible	Staggered	40x40	100	1000
7	Compressible	Staggered	60x60	100	1000
8	Compressible	Staggered	10x10	400	1000
8	Compressible	Staggered	20x20	400	1000
8	Compressible	Staggered	40x40	400	1000
8	Compressible	Staggered	60x60	400	1000
9	Compressible	Staggered	10x10	1000	1000
9	Compressible	Staggered	20x20	1000	1000
9	Compressible	Staggered	40x40	1000	1000
9	Compressible	Staggered	60x60	1000	1000

### 3.2.1 INCOMPRESSIBLE FLOW, STAGGERED GRID (Problem No: 1-3)

First, the simplest case (thermal effects are absent and  $Re=100$ ) with coarse mesh have been investigated. Then, the solution is repeated with finer grids to obtain closer results to the benchmark solution given by Ghia et al. (1982). Secondly, the same procedure has been applied for  $Re=400$  and results are again compared to those found in Ghia et al. (1982).

Figure 3.11 shows that the  $u$  velocity results of in-house code at the mid section, it shows a good agreement with the reference results of Ghia et al. (1982). A coarse mesh of  $10 \times 10$  has been used.

The incompressible flow field simulation with a denser mesh has been performed again at  $Re=100$ . Figure 3.12 shows that the  $u$  velocity results of in-house code at the mid section shows good agreement with the reference results of Ghia et al. (1982). A mesh of  $20 \times 20$  has been used. The conformity of the results to the reference results has improved compared to the previous case.

Figure 3.13 shows the results obtained by utilising a smaller cell size; a mesh of 40x40 has been employed. The values obtained by the in-house code is almost the same with those from the reference solution.

Figure 3.14 shows the  $u$  velocity at the mid section for a finer grid,  $dx=dy=1/60$ . Again, no discrepancy between reference solution and solution from the in-house code has been observed.

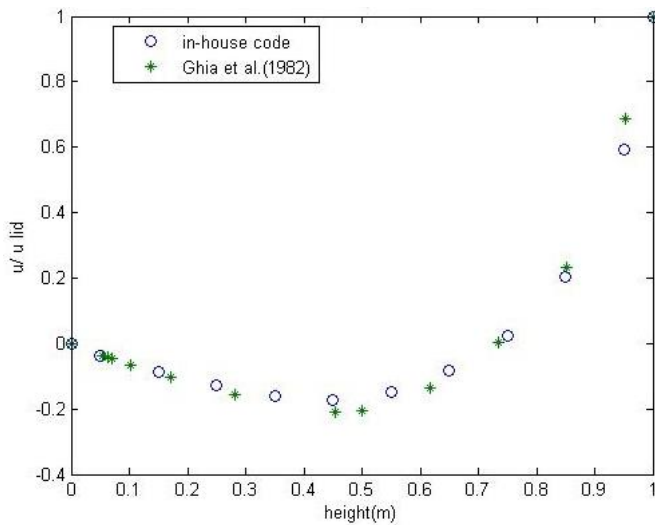


Figure 3.11. Variation of  $u$  velocity,  $Re=100$ ,  $dx=1/10$ ,  $dy=1/10$

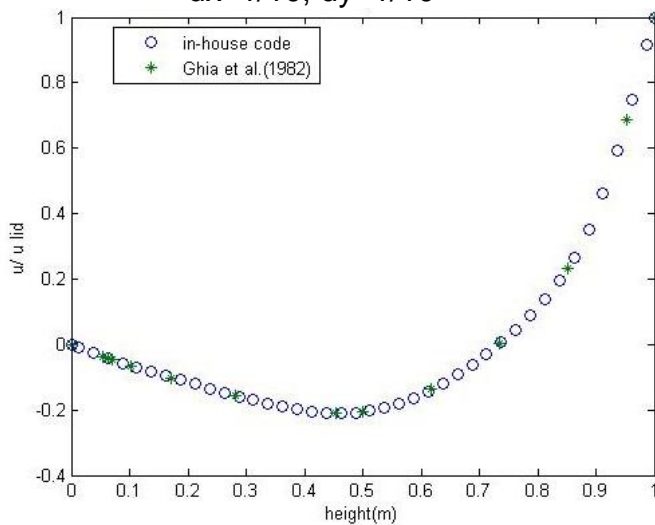


Figure 3.13. Variation of  $u$  velocity,  $Re=100$ ,  $dx=1/40$ ,  $dy=1/40$

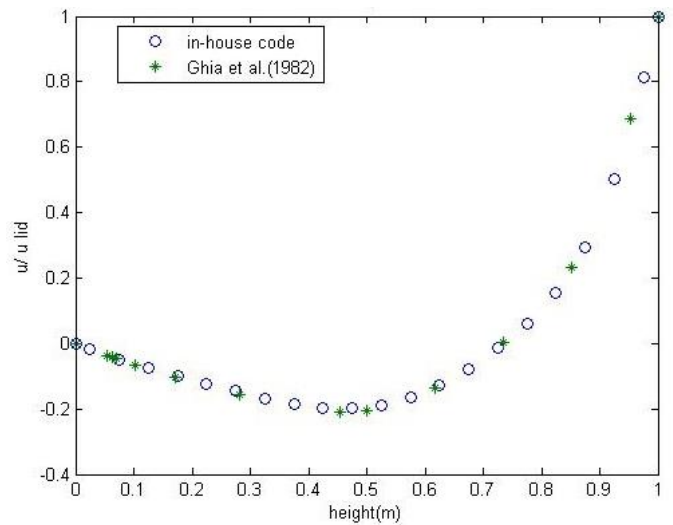


Figure 3.12. Variation of  $u$  velocity,  $Re=100$ ,  $dx=1/20$ ,  $dy=1/20$

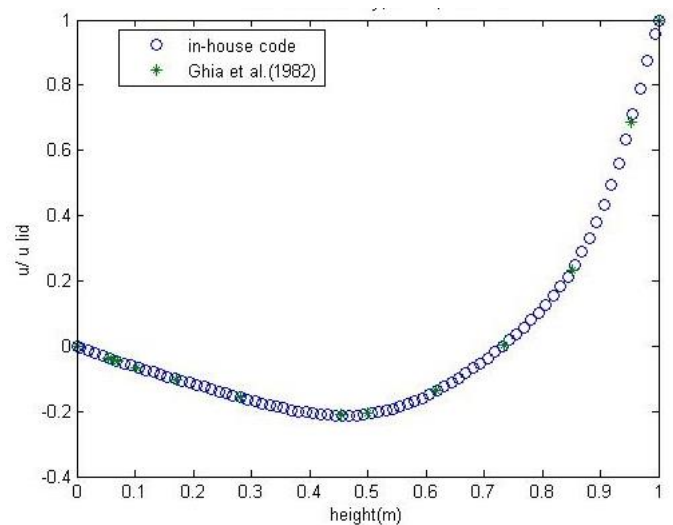


Figure 3.14. Variation of  $u$  velocity,  $Re=100$ ,  $dx=1/80$ ,  $dy=1/80$

For higher Reynolds numbers, the difference between reference solution and the solution from the in-house code slightly increases when the mesh size is 40x40. This is illustrated in Figure 3.15. The discrepancy between the reference solution and the solution from the in-house code can be lessened by utilising finer grids; 80x80 and 120x120. This is illustrated in Figure 3.16 and Figure 3.17.

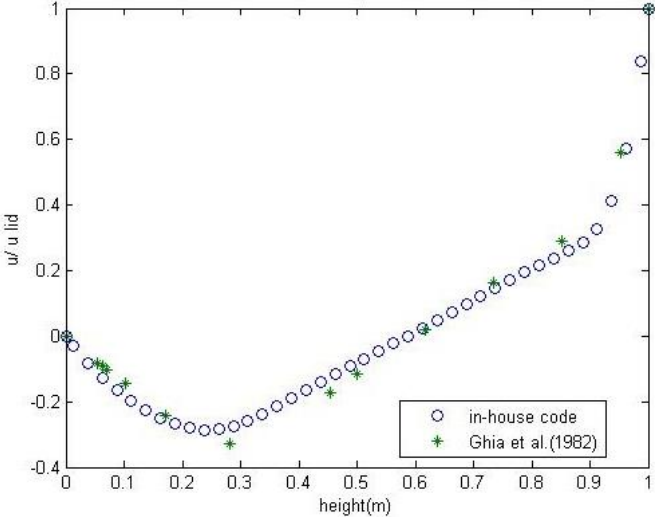


Figure 3.15. Variation of  $u$  velocity,  $Re=400$ ,  $dx=1/40$ ,  $dy=1/40$

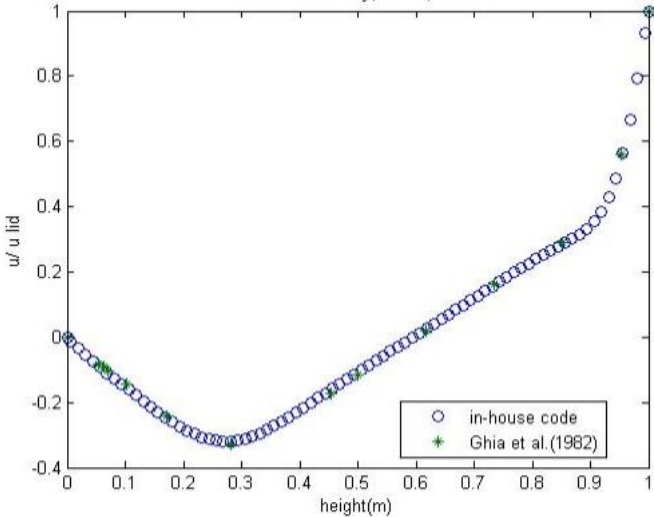


Figure 3.16. Variation of  $u$  velocity,  $Re=400$ ,  $dx=1/80$ ,  $dy=1/80$

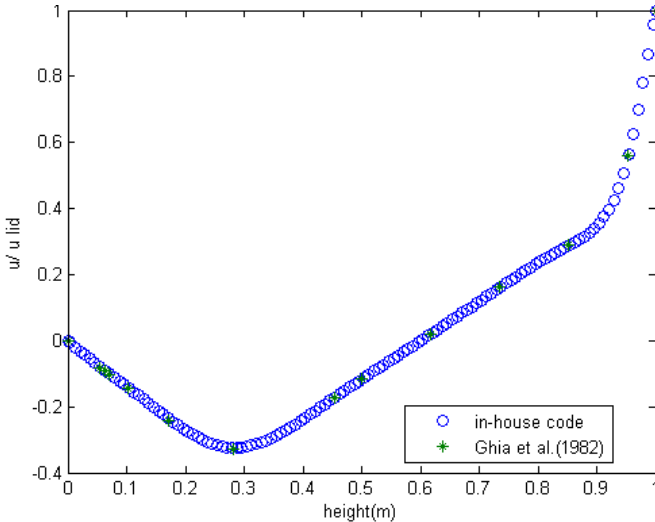


Figure 3.17. Variation of  $u$  velocity,  $Re=400$ ,  $dx=1/120$ ,  $dy=1/120$

Next, solution has been performed for  $Re=1000$ . Figure 3.18 shows the  $u$  velocity solution with  $40 \times 40$  mesh for  $Re=1000$ . The discrepancy between the solutions are more remarkable compared to  $Re=400$ . Near the bottom boundary and top boundary, the coarse mesh has difficulty in reaching the reference values, which have been obtained with a  $128 \times 128$  mesh. Still, good conformity has been observed.

Figure 3.19 shows the variation of  $u$  velocity at mid length, with a finer mesh. This time, the results obtained from the in-house code is closer to the reference results compared to the previous coarser mesh.

The solution has been performed with the finest mesh of  $120 \times 120$  for  $Re=1000$  in Figure 3.20. The conformity of the results to the reference results have improved with grid improvement. There is still some difference between the reference solution and the solution obtained from the in-house code. Note that Ghia et al. (1982) used a fourth order accurate discretisation scheme with  $256 \times 256$  grid. So that, small differences between the results of Ghia et al. (1982) and results obtained when using dense grids is apprehensible.

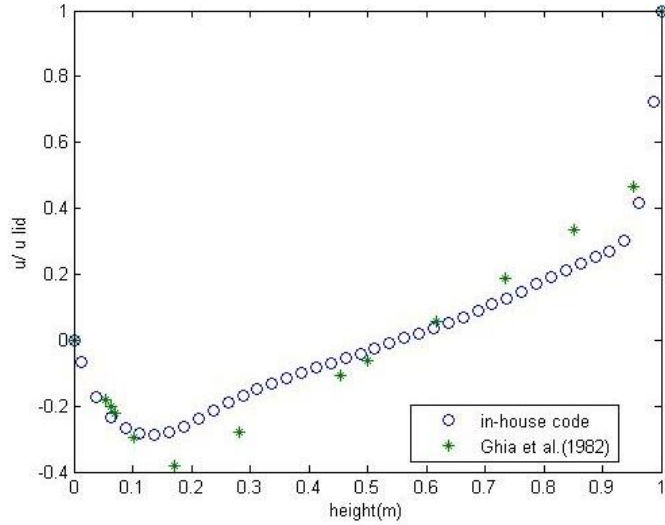


Figure 3.18. Variation of  $u$  velocity,  $Re=1000$ ,  $dx=1/40$ ,  $dy=1/40$

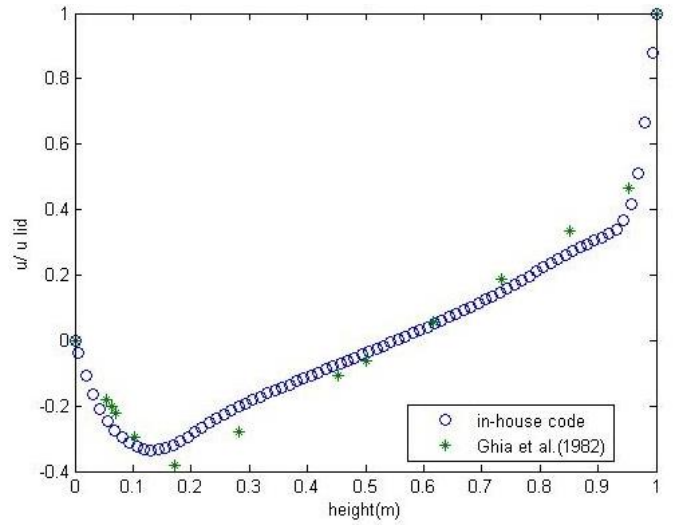


Figure 3.19. Variation of  $u$  velocity at mid length,  $Re=1000$ ,  $dx=1/80$ ,  $dy=1/80$

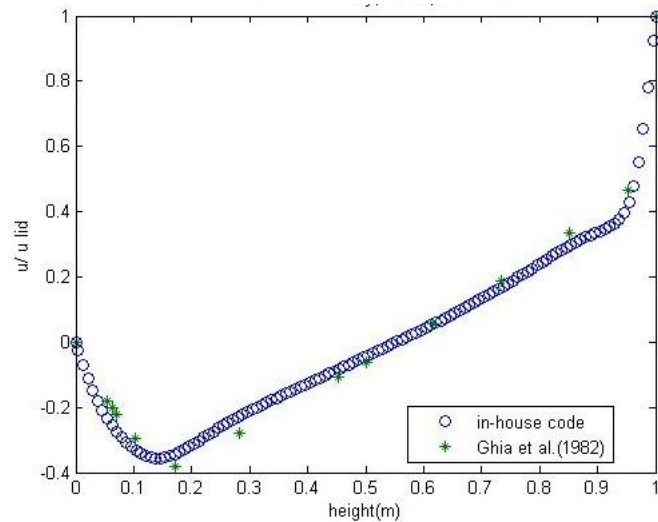


Figure 3.20. Variation of  $u$  velocity at mid length,  $Re=1000$ ,  $dx=1/120$ ,  $dy=1/120$

The error variation with grid density has been studied in Figure 3.21, Figure 3.22, and Figure 3.23 for the first three problem. The results of Ghia et al. (1982) has been used as the benchmark solution for the error analysis. The midpoint  $u$  velocity given by Ghia et al. (1982) has been selected as the reference point for the error analysis. The results obtained have been interpolated to the midpoint of computational domain whenever needed. The error that has been given is the absolute error compared to

the result of Ghia et al. (1982). It has been observed that error decreases with finer grid for all the cases.

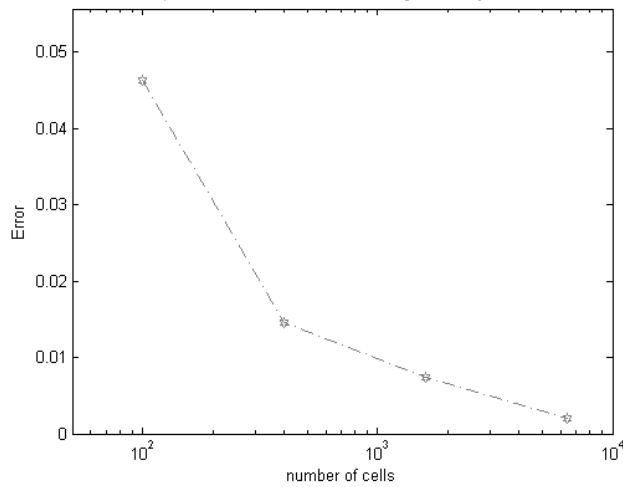


Figure 3.21. Midpoint absolute error variation with grid density, Re=100

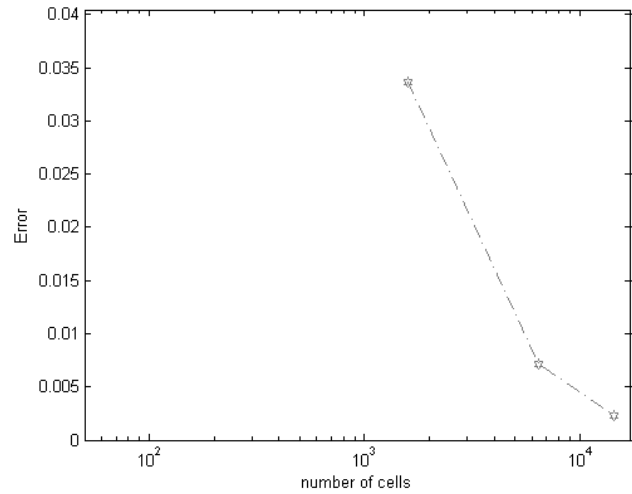


Figure 3.22. Midpoint absolute error variation with grid density, Re=400

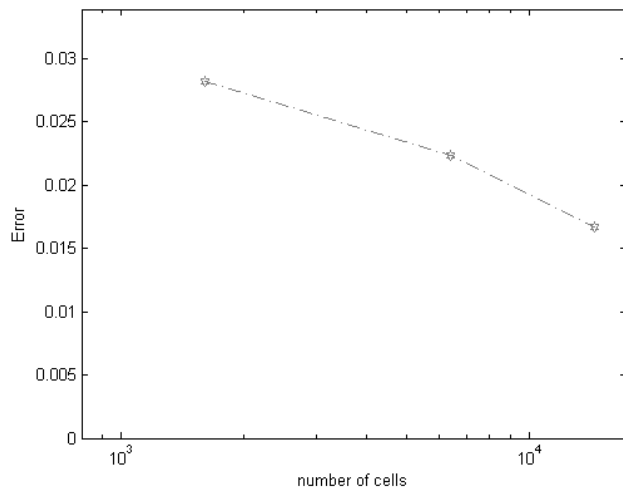


Figure 3.23. Midpoint absolute error variation with grid density, Re=1000.

In the next section, collocated grid arrangement has been utilised to solve the lid driven cavity problem.

### 3.2.2 INCOMPRESSIBLE FLOW, COLLOCATED GRID (Problem No:4)

For the collocated grid, Rhie-Chow interpolation scheme has been utilised. One important characteristic of Rhie-Chow interpolation is that for very coarse meshes



results may lose its meaning. This is not happening in a staggered grid configuration, which is one practical advantage of the staggered grid over the collocated one. The results given below have been obtained for a 28x28 grid.

Error is defined as the maximum of (velocity variation, continuity flux imbalance) in the code. Such a hybrid error definition is useful to get a more realistic picture of the flow. Hybrid method has been employed to calculate convective fluxes. The following figures have been obtained with a 28x28 collocated grid. Figure 3.24 shows that error decreases in a relatively smooth manner during iterations. The Reynolds number is taken to be 100.

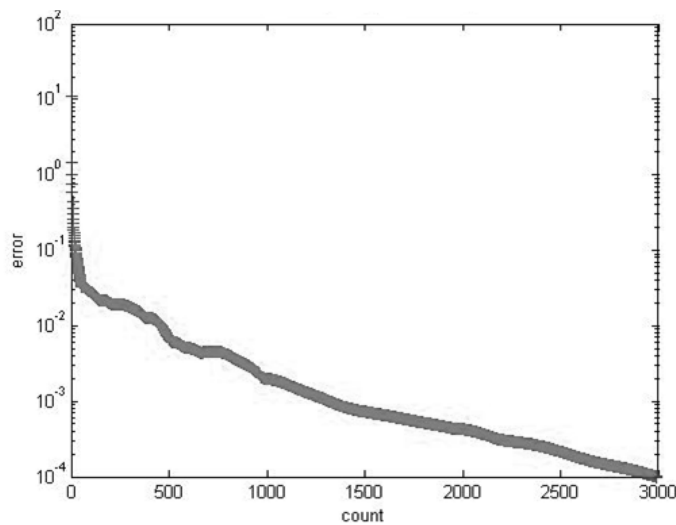


Figure 3.24. Error variation with iteration number,  $Re=100$ ,  $dx=1/28$ ,  $dy=1/28$

Figure 3.25, Figure 3.27, Figure 3.29 show the variation of  $u$  velocity at mid length obtained by using collocated grid for different grid densities. The results obtained by collocated grid is very close to the reference values. Figure 3.26, Figure 3.28, and Figure 3.30 show the variation of  $v$  velocity at mid height obtained by utilizing collocated grid for different grid densities. Again, results are in good conformity even for the rather coarse 28x28 mesh.

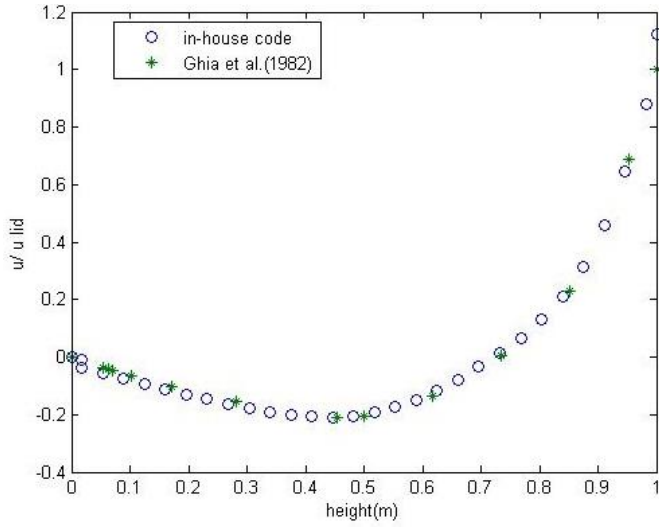


Figure 3.25. Variation of  $u$  velocity at  $x=0.5$ , Reynolds number 100,  $dx=1/28$ ,  $dy=1/28$

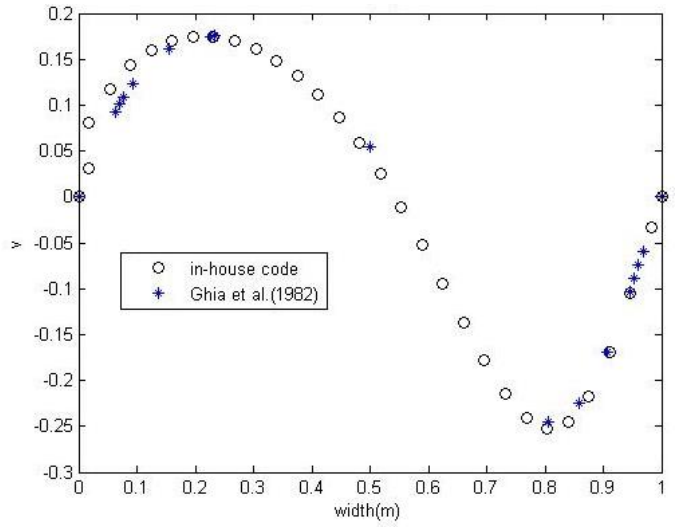


Figure 3.26. Variation of  $v$  velocity at  $y=0.5$ , Reynolds number 100,  $dx=1/28$ ,  $dy=1/28$

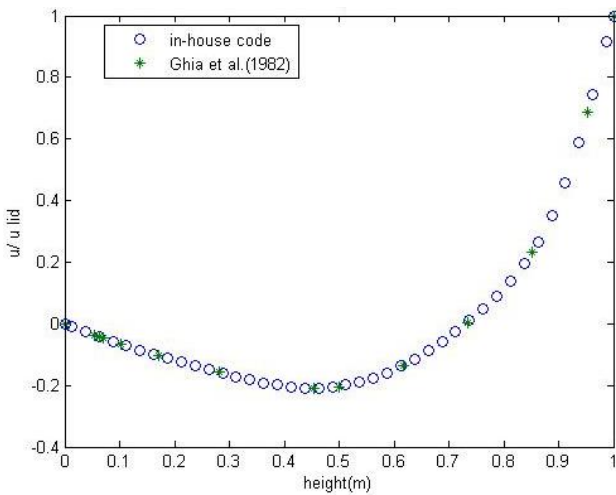


Figure 3.27. Variation of  $u$  velocity at  $x=0.5$ , Reynolds number 100,  $dx=1/40$ ,  $dy=1/40$

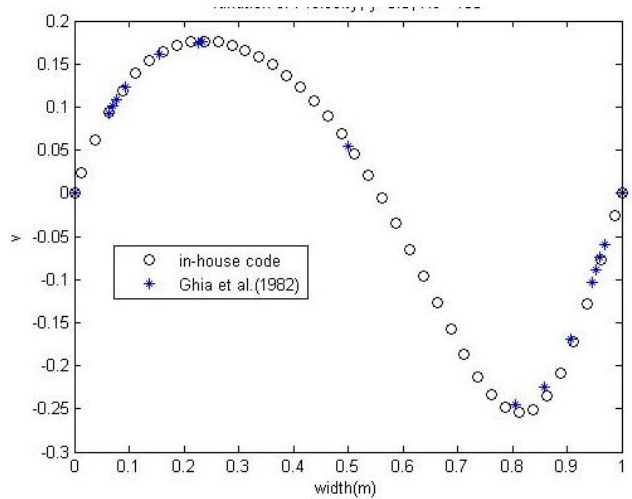


Figure 3.28. Variation of  $v$  velocity at  $y=0.5$ , Reynolds number 100,  $dx=1/40$ ,  $dy=1/40$

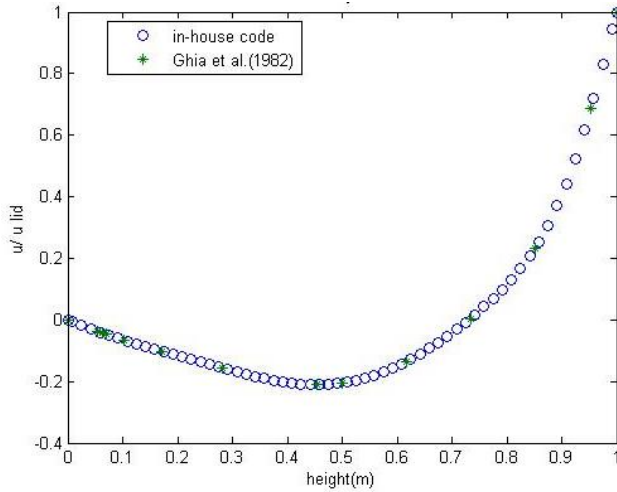


Figure 3.29. Variation of  $u$  velocity at  $x=0.5$ , Reynolds number 100,  $dx=1/60$ ,  $dy=1/60$

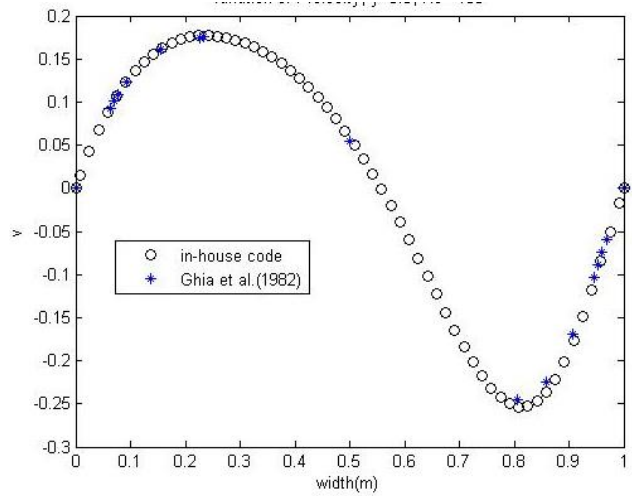


Figure 3.30. Variation of  $v$  velocity at  $x=0.5$ , Reynolds number 100,  $dx=1/60$ ,  $dy=1/60$

Error analysis has also been performed. For the error analysis, the finest grid resolution ( $dx=dy=1/80$ ) has been selected as the benchmark solution. Middle point  $u$  velocity of the reference solution has been selected as the target value. The results obtained with coarser grids then have been compared with this value. Error plot for the absolute error obtained in this manner is given in Figure 3.31.

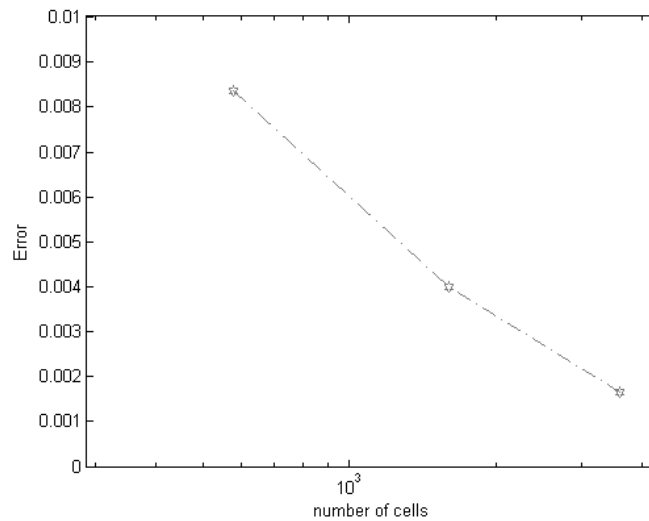


Figure 3.31. Midpoint  $u$  velocity absolute error variation with grid density,  $Re=100$ , collocated grid

### 3.2.3 COMPRESSIBLE FLOW, STAGGERED GRID (Problem No: 6-9)

For the compressible case, a compressible form of the lid driven cavity problem has been formulated by introducing wall temperatures. This has been carried out to solve the compressible form of the Navier Stokes equations.

The results have been obtained using First Order Upwind method for the computation of convective fluxes in the momentum and energy equations. Upwinding is also required for the density terms. After the temperature and pressure fields have been obtained using energy equation and SIMPLE procedure, the density field is calculated using the equation of state. Similar to other transport variables, under-relaxation is needed for the thermal energy equation as well.

To solve the equation of state, operating/reference pressure should be defined. After obtaining the operative pressure (relative pressure), it is summed with an absolute pressure. The final pressure thus obtained is used in the equation of state. Note that a similar procedure is utilised in commercial CFD solvers, such as ANSYS Fluent.

$$P = P_{\text{solution}} + P_{\text{op}} \quad (3.2)$$

Figure 3.32 shows the variation of temperature inside the lid driven cavity. The right wall is kept at 700 K while the other walls are maintained at 293 K. High temperature gradients in the region close to right wall and relatively low temperature gradients in the middle region is evident. From the analyses it has been observed that the solution takes approximately **60% more time** compared to incompressible simulation.

The isotherm map is rather complex. If there was no cavity flow, the regular parabolic curve structure would have formed. Instead, the cavity flow pushes the isotherm lines downward as can be observed in Figure 3.32.

Figure 3.33 shows the variation of density inside the lid driven cavity for Re=400. The density isolines follow approximately -but not exactly due to the effects of pressure and velocity terms- the isotherm lines. If the solution had been performed with a density approximated as solely a linear function of temperature, as in the case of Boussinesq approximation, the density isolines would have followed isotherm lines

more closely. To get a more realistic picture of the flow field, compressible solution where the dependence of density both on temperature and pressure is required.

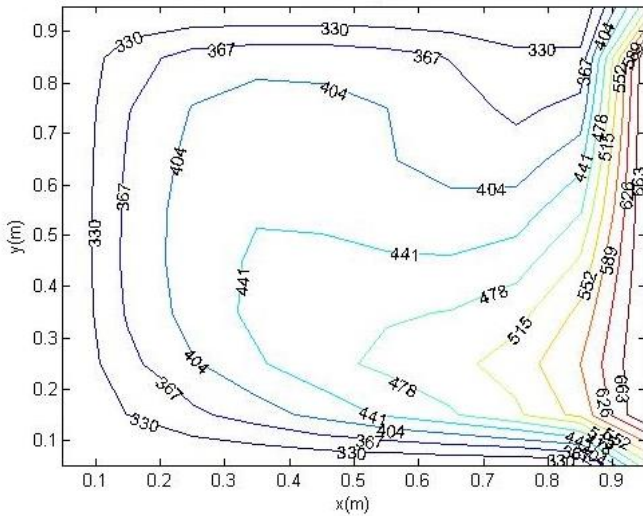


Figure 3.32. Variation of temperature for Reynolds number=400,  $dx=dy=1/10$ ,  $T_{\text{rightwall}}=700\text{ K}$

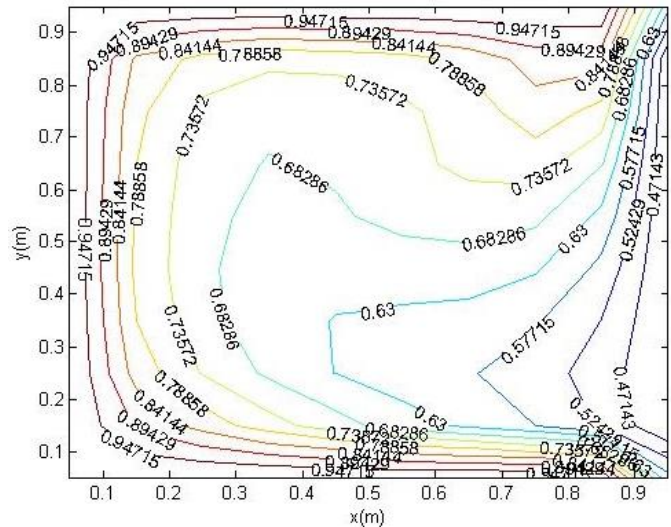


Figure 3.33. Variation of density for Reynolds number= 400,  $dx=dy=1/10$ ,  $T_{\text{rightwall}}=700\text{ K}$

Figure 3.34 shows the variation of temperature with a finer grid. It is evident that isotherm lines are getting smoother due to the use of finer grid spacing. Similarly, Figure 3.35 shows the variation of density with the same finer grid. It is evident that density isolines are smoother due to the use of finer grid resolution.

It is evident that, even with the relatively coarse mesh solutions given in Figure 3.34 and Figure 3.35, the motion of the lid causes a somewhat “swirling” temperature and density distribution inside the cavity. If this had been a regular heated plate with no momentum transport, a much regular pattern for the temperature distribution would have been observed.

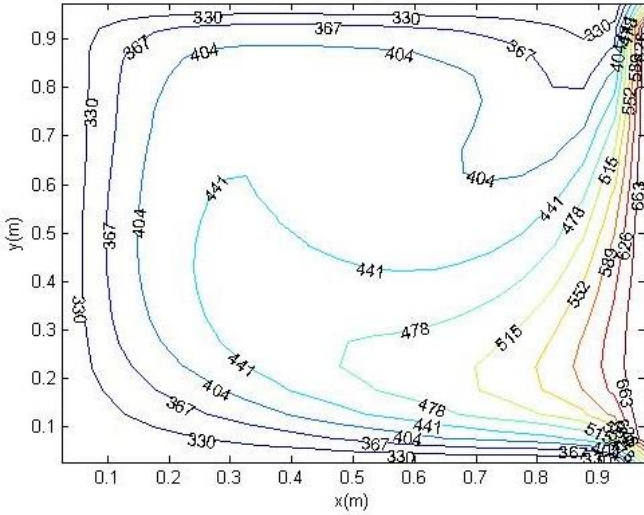


Figure 3.34. Variation of temperature for Reynolds number=400,  $dx=dy=1/20$ ,  $T_{\text{rightwall}}=700\text{K}$

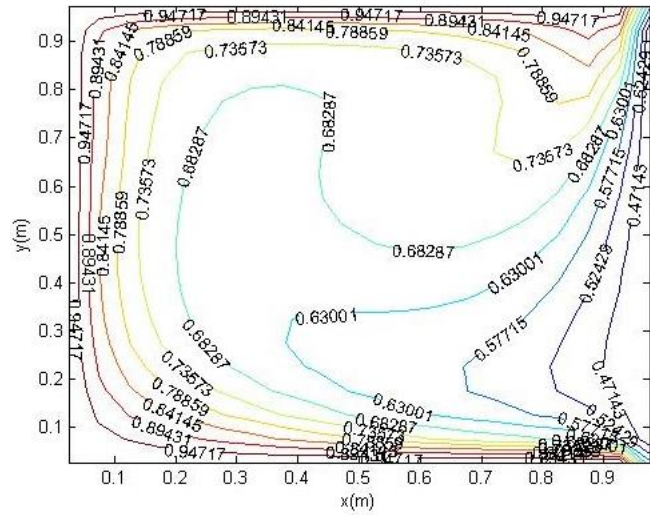


Figure 3.35. Variation of density for Reynolds number=400,  $dx=dy=1/20$ ,  $T_{\text{rightwall}}=700\text{K}$

Figure 3.36 shows the variation of temperature with  $dx=dy=1/40$  grid. The isotherm curves are smoother compared to the case with a relatively coarser,  $dx=dy=1/20$  grid. Values obtained are very close to those obtained previously.

Figure 3.37 shows the variation of density with  $dx=dy=1/40$  grid. The density isolines are smoother compared to the case with  $dx=dy=1/20$  grid. Values obtained are very close to those obtained previously.

Figure 3.38 shows the variation of temperature with  $dx=dy=1/60$  grid. Note the high gradient region appears especially near the right boundary. Figure 3.39 shows the variation of density with the same grid cell size of  $dx=dy=1/60$ . Similar to temperature field, it is worth noting the existence of high gradients especially near the right boundary. Swirling in the density field is again, evident. The isolines are smoother compared to coarser meshes used previously.

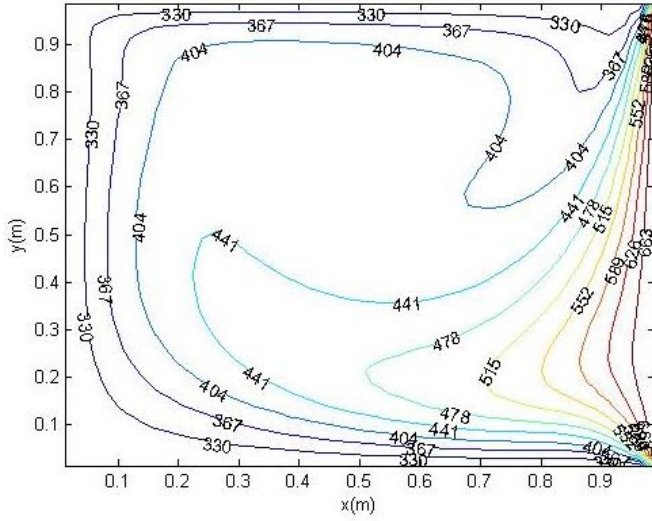


Figure 3.36. Variation of temperature, Reynolds number=400,  $dx=dy=1/40$ ,  $T_{\text{rightwall}}=700$  K

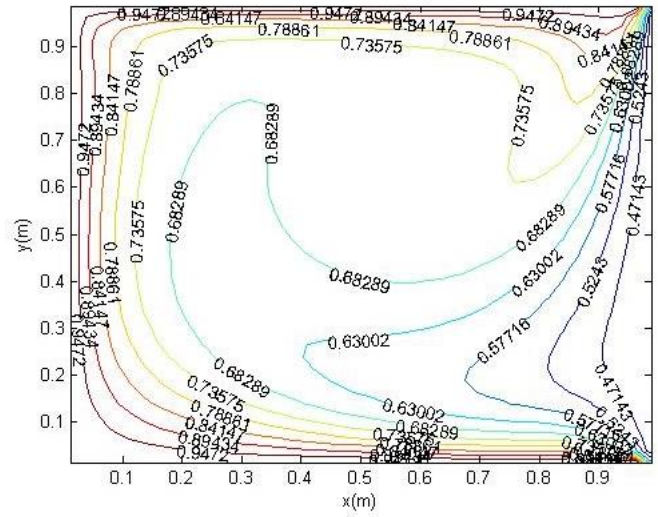


Figure 3.37. Variation of density, Reynolds number=400,  $dx=dy=1/40$ ,  $T_{\text{rightwall}}=700$  K

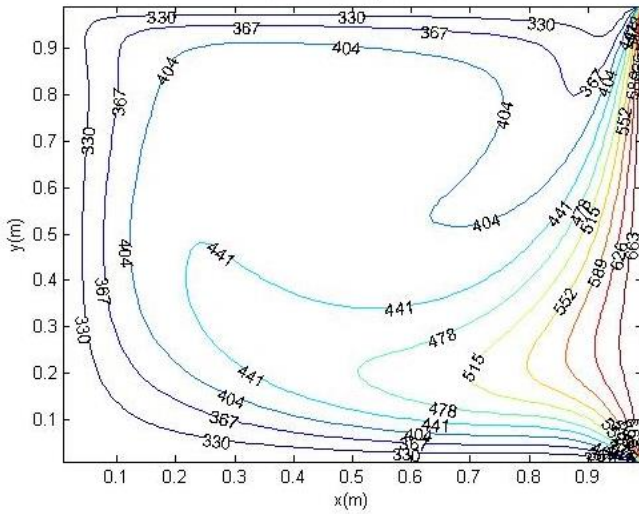


Figure 3.38. Variation of temperature,  $Re=400$ ,  $dx=dy=1/60$ ,  $T_{\text{rightwall}}=700$  K

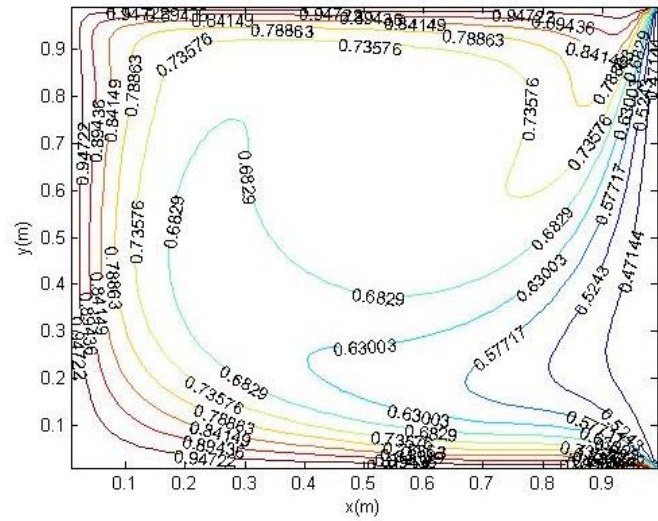


Figure 3.39. Variation of density,  $Re=400$ ,  $dx=dy=1/60$ ,  $T_{\text{rightwall}}=700$  K

Next, the solutions for  $Re=1000$  have been performed.

Figure 3.40 shows the temperature variation for  $Re=1000$ . Since a very coarse mesh,  $dx=dy=1/10$  is used the isolines are far from smooth. Swirling field and high temperature gradient near the right boundary is also evident.

Figure 3.41 shows the variation of density for  $Re=1000$ . For Figure 3.41, a pattern similar to that found in Figure 3.37 has been observed. However, note that the isolines representing 0.68 and 0.63 don't extend to far left as much as in the case of Figure 3.37. In other words, in the middle region, higher densities, and lower temperatures are observed compared to lower  $Re$  ( $Re=400$ ,  $Re=100$ ) solutions. The temperature is "convected" better towards the left side.

Figure 3.42 shows the temperature variation for  $Re=1000$  for  $dx=dy=1/20$ . Isotherm lines are smoother compared to the coarsest grid solution ( $dx=dy=1/10$ ). Swirling field and high temperature gradient near the right boundary are also evident. Similarly, Figure 3.43 shows the density variation for  $Re=1000$  with the same grid cell size of  $dx=dy=1/20$ . Density isolines are smoother compared to the coarsest grid solution ( $dx=dy=1/10$ ). Swirling density field and high density gradient near the right boundary are visible as well. In the middle region, changes in density and temperature are relatively smooth compared to coarser grid solution.



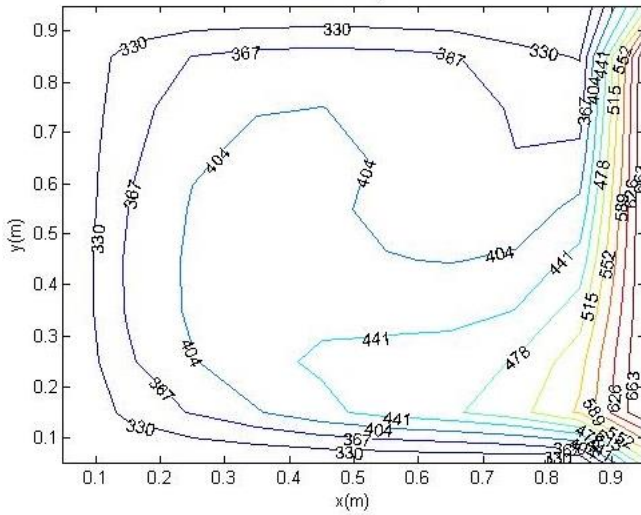


Figure 3.40. Variation of temperature,  $Re=1000$ ,  $dx=dy=1/10$ ,  $T_{rightwall}=700$  K

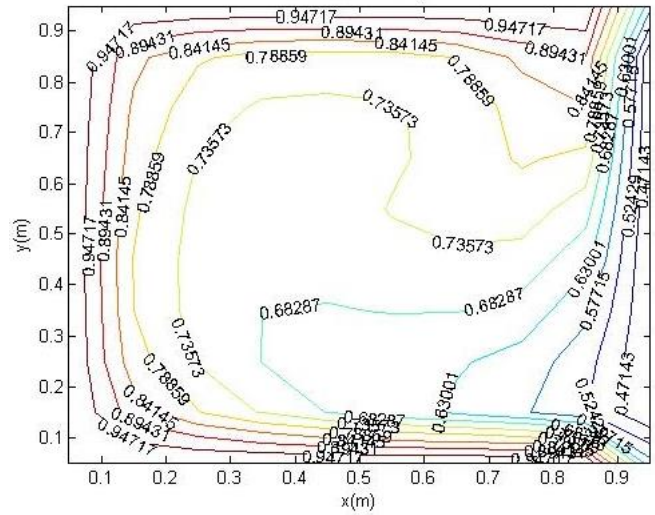


Figure 3.41. Variation of density,  $Re=1000$ ,  $dx=dy=1/10$ ,  $T_{rightwall}=700$  K

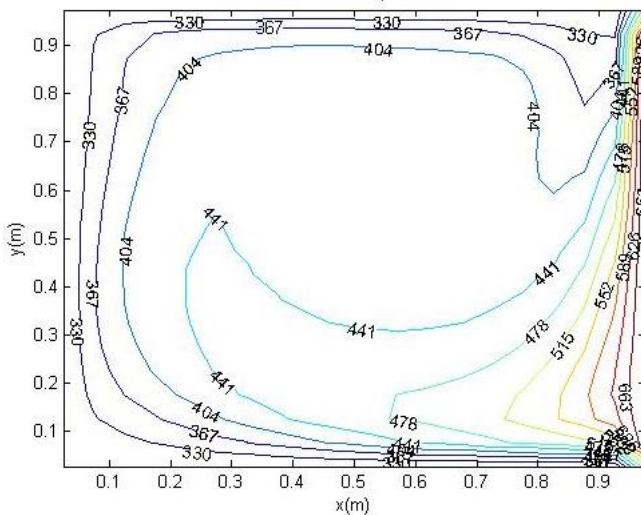


Figure 3.42. Variation of temperature,  $Re=1000$ ,  $dx=dy=1/20$ ,  $T_{rightwall}=700$  K

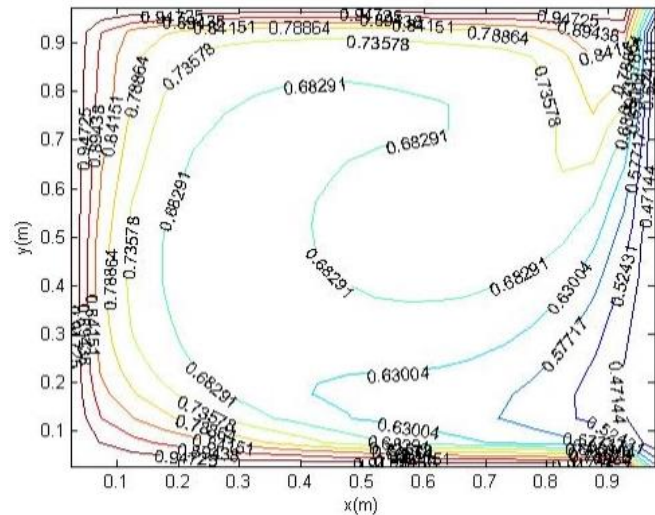


Figure 3.43. Variation of density for  $Re=1000$ ,  $dx=dy=1/20$ ,  $T_{rightwall}=700$  K

Figure 3.44 shows the isotherm lines for the  $dx=dy=1/40$  grid. The isolines are clearly a blend of streamlines typical of lid driven cavity flow and isotherms seen in a heat transfer problem with isothermal boundary condition.

Figure 3.45 shows the density isolines for the  $dx=dy=1/40$  grid.

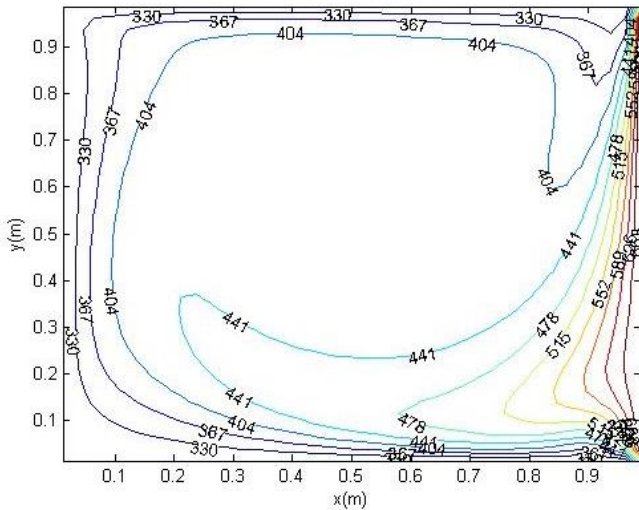


Figure 3.44. Variation of temperature for  $Re=1000$ ,  $dx=dy=1/40$ ,  $T_{rightwall}=700$  K

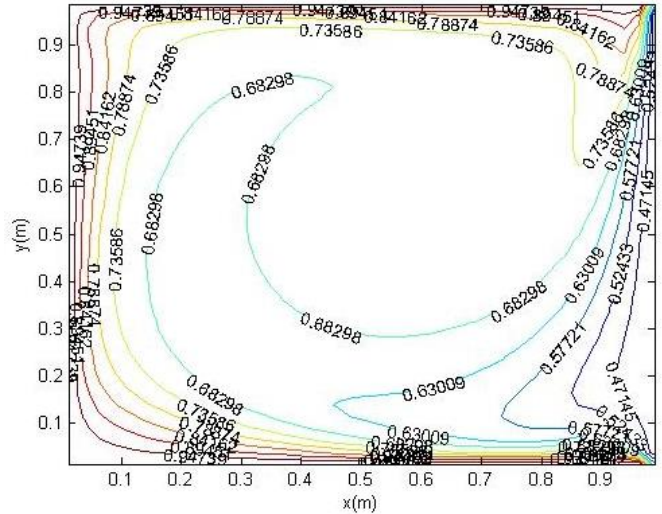


Figure 3.45. Variation of density for  $Re=1000$ ,  $dx=dy=1/40$ ,  $T_{rightwall}=700$  K

Figure 3.46 shows the finest grid ( $dx=dy=1/60$ ) solution for temperature. The isolines are smoother with little change in values compared to coarser grid ( $dx=dy=1/40$ ).

Figure 3.47 shows the finest grid ( $dx=dy=1/60$ ) density solution. The isolines are again smoother with little change in values compared to coarser grid ( $dx=dy=1/40$ ).

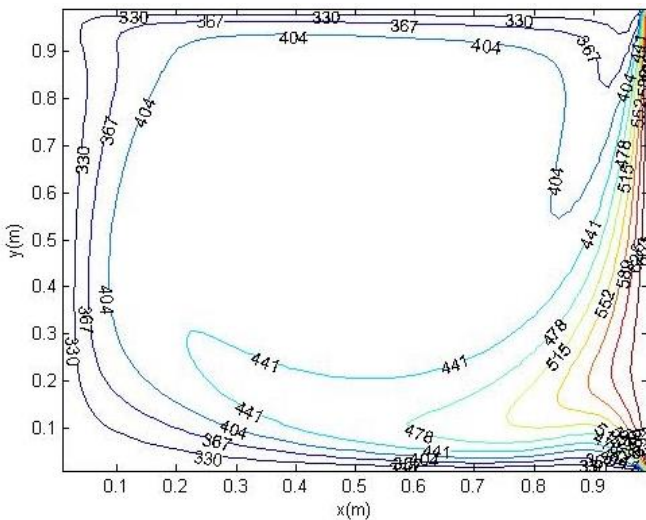


Figure 3.46. Variation of temperature for  $Re=1000$ ,  $dx=dy=1/60$ ,  $T_{rightwall}=700$  K

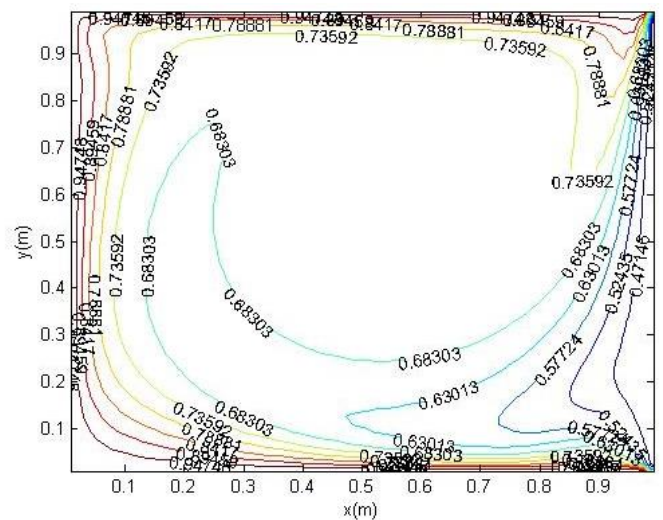


Figure 3.47. Variation of density for  $Re=1000$ ,  $dx=dy=1/60$ ,  $T_{rightwall}=700$  K

For the  $Re=400$  and  $Re=1000$  solutions where the right wall is kept at 700 Kelvins, error analysis has also been performed. For the error analysis a finer grid resolution

( $dx=dy=1/60$ ) has been selected as the benchmark solution. Error definition is the same with the definition given in Section 3.2.1. Error plots are given in Figure 3.48 and Figure 3.49.

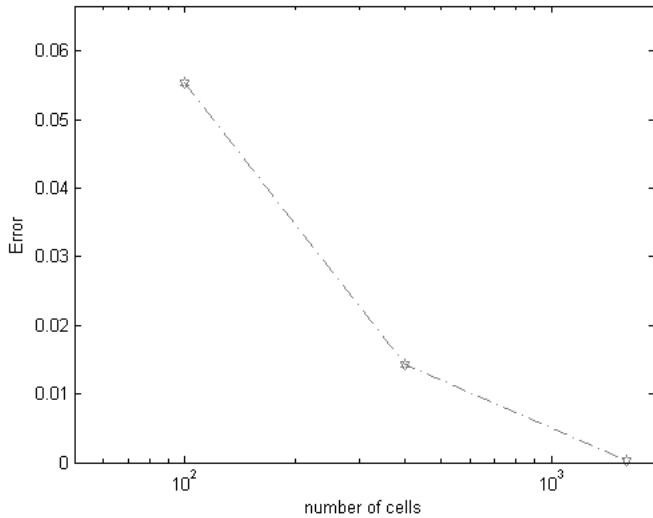


Figure 3.48. Midpoint u velocity absolute error variation with grid density, Re=400

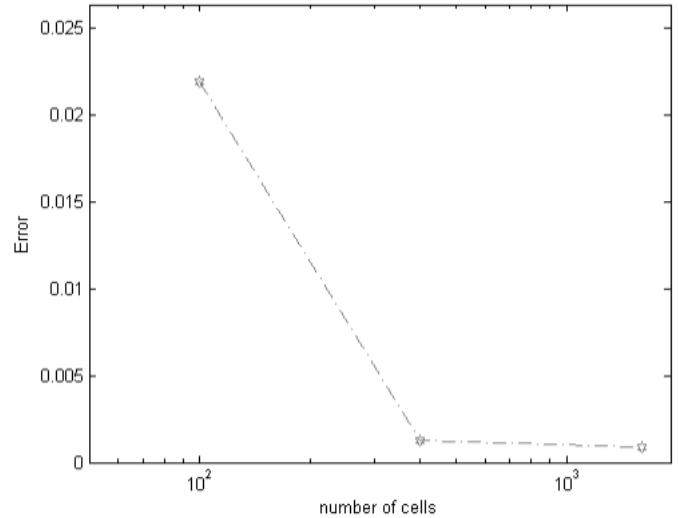


Figure 3.49. Midpoint u velocity absolute error variation with grid density, Re=1000

Next, the solutions have been carried out again with right wall fixed at 1000 K this time to study the effect of increasing diffusion term.

Figure 3.50 shows the variation of density for Re=100,  $dx=dy=1/10$  with  $T_{right\ wall}=1000\ K$ . The density values are overall smaller compared to the case where right wall was kept at 700 K. Also note that due to the lower Re (Re=100), the convective effects are lower compared to Re=1000 case given previously and density field follow more closely the field that can be observed in a pure thermal diffusion problem.

Figure 3.51 shows that the isotherm lines in this diffusion dominated case resemble isotherm lines in a pure diffusion problem due to the low Reynolds number and hence lower convection.

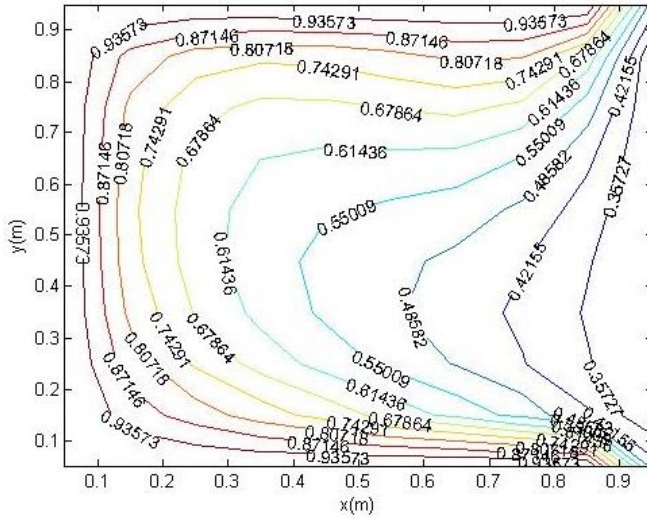


Figure 3.50. Variation of density for Reynolds number=100,  $dx=dy=1/10$ ,  $T_{\text{rightwall}}=1000$  K

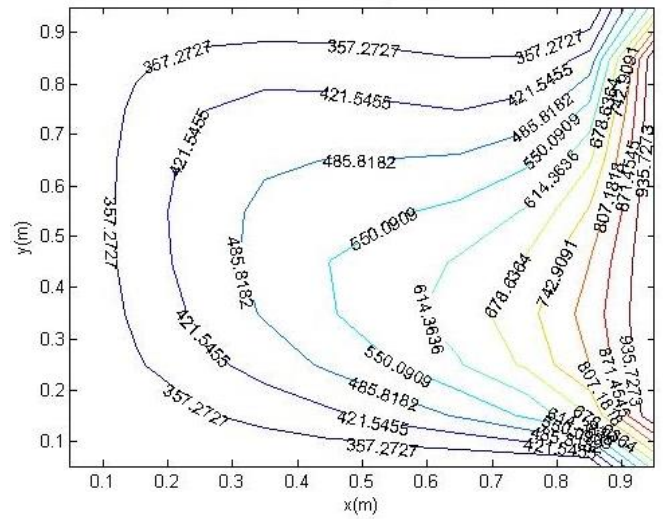


Figure 3.51. Variation of temperature for Reynolds number=100,  $dx=dy=1/10$ ,  $T_{\text{rightwall}}=1000$  K

Figure 3.52 shows the density variation for  $Re=100$ , with grid parameter  $dx=dy=1/20$ . Due to the low  $Re$ , isolines are similar to those found in a pure diffusion problem. slight downward bending in the isolines due to convective effects is observable. The mid region densities are lower compared to the case where  $T_{\text{rightwall}}=700$  K.

Figure 3.53 shows the variation of temperature variation for  $Re=100$ , with grid parameter  $dx=dy=1/20$ . The mid region temperatures compared to the case where the right wall was kept at 700 K. Again, somewhat swirling isotherms are seen in the solutions for  $Re=1000$  which does not exist for  $Re=100$  solution.

Figure 3.54 and Figure 3.55 show variation of density and temperature for the  $dx=dy=1/40$  grid.

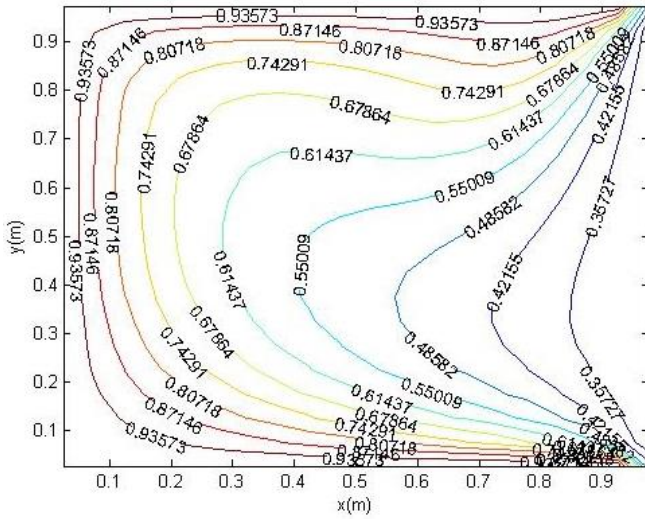


Figure 3.52. Variation of density for Reynolds number=100,  $dx=dy=1/20$ ,  $T_{\text{rightwall}}=1000 \text{ K}$

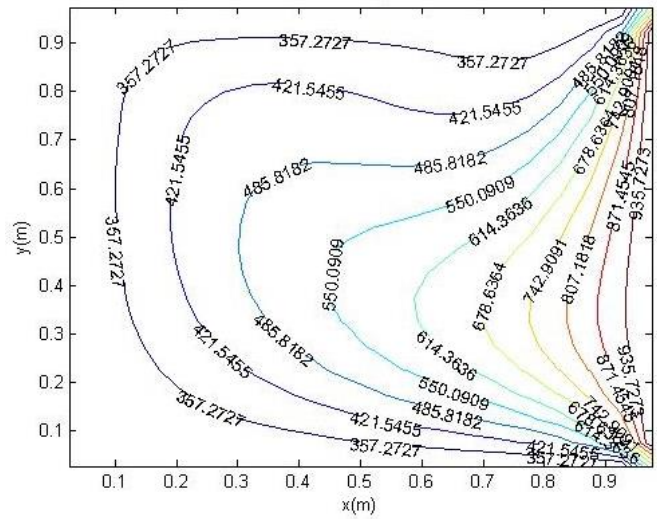


Figure 3.53. Variation of temperature for Reynolds number=100,  $dx=dy=1/20$ ,  $T_{\text{rightwall}}=1000 \text{ K}$

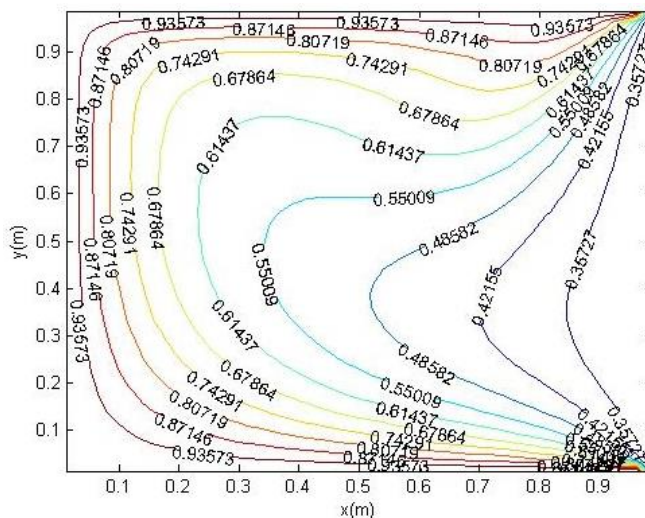


Figure 3.54. Variation of density for Reynolds number=100,  $dx=dy=1/40$ ,  $T_{\text{rightwall}}=1000 \text{ K}$

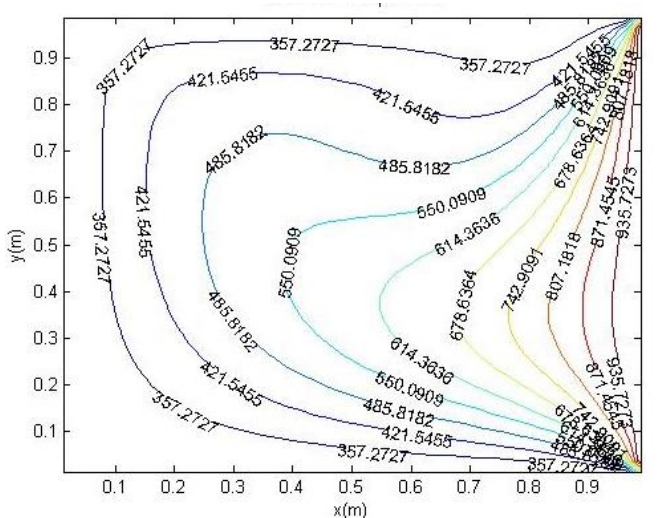


Figure 3.55. Variation of temperature for Reynolds number=100,  $dx=dy=1/40$ ,  $T_{\text{rightwall}}=1000 \text{ K}$

Next, the case where  $Re=400$ ,  $T_{\text{rightwall}}=1000 \text{ K}$  is studied. The right wall is kept at 1000 K. In this case, diffusive effects are higher compared to the case where right wall was kept at 700 K and convective effects are higher compared to the case where  $Re=100$ . So that, this solution is somewhat in between the above mentioned two solution cases.

Figure 3.56, Figure 3.58, and Figure 3.60 show the density isolines for different grid resolutions. Lower densities compared to the case where  $T_{\text{rightwall}}=700\text{ K}$  and higher amount of swirl compared to case where  $Re=100$  is observable.

Figure 3.57, Figure 3.59, and Figure 3.61 show the isotherm lines for different grid resolutions. Higher temperatures compared to the case where  $T_{\text{rightwall}}=700\text{ K}$  and higher amount of swirl compared to case where  $Re=100$  is observable.

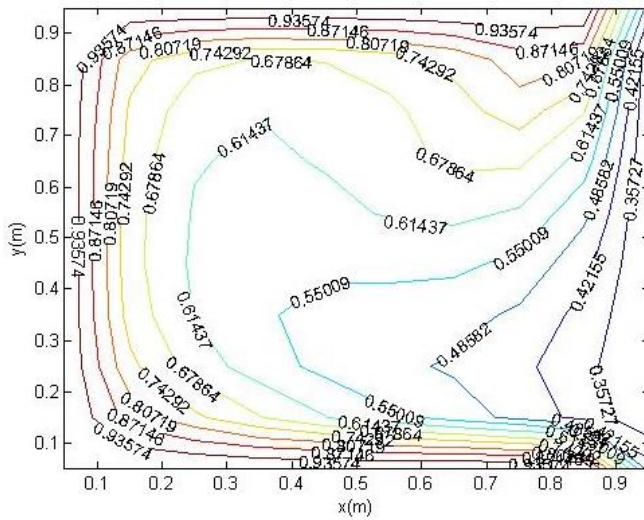


Figure 3.56. Variation of density for Reynolds number=400,  $dx=dy=1/10$ ,  $T_{\text{rightwall}}=1000\text{ K}$

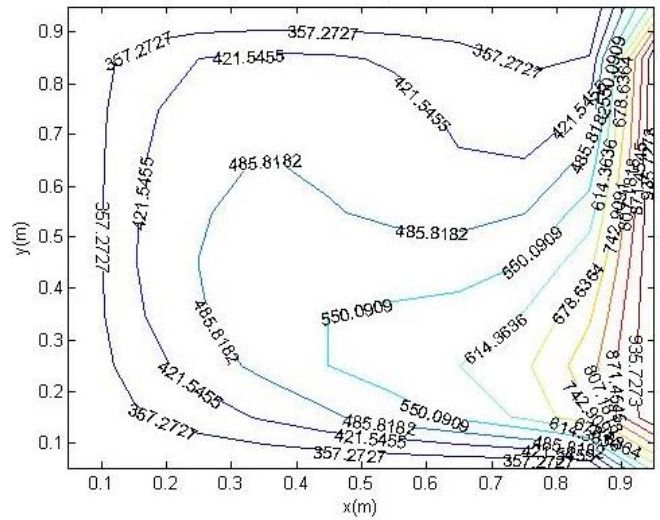


Figure 3.57. Variation of temperature for Reynolds number=400,  $dx=dy=1/10$ ,  $T_{\text{rightwall}}=1000\text{ K}$

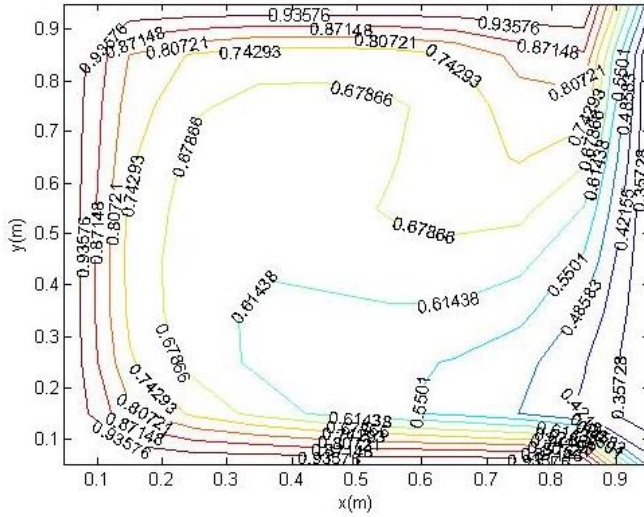


Figure 3.58. Variation of density for Reynolds number=1000,  $dx=dy=1/20$ ,  $T_{\text{rightwall}}=1000$  K

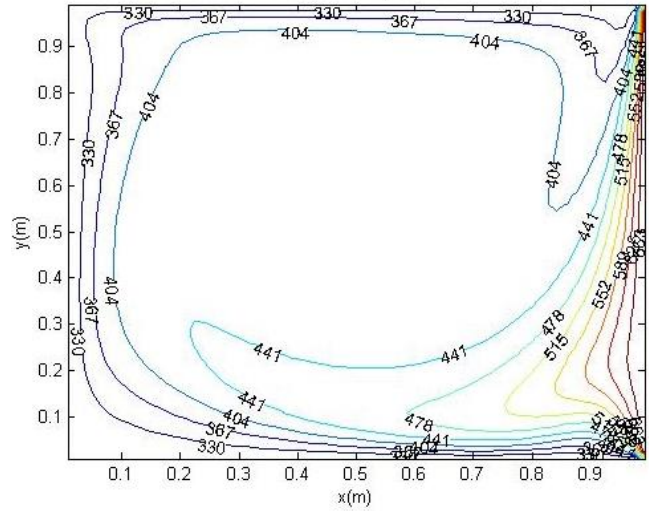


Figure 3.59. Variation of temperature for Reynolds number=1000,  $dx=dy=1/20$ ,  $T_{\text{rightwall}}=1000$  K

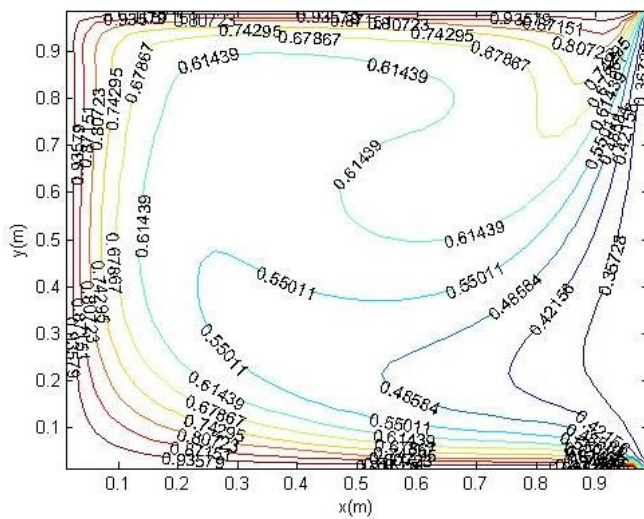


Figure 3.60. Variation of density for Reynolds number=400,  $dx=dy=1/40$ ,  $T_{\text{rightwall}}=1000$  K

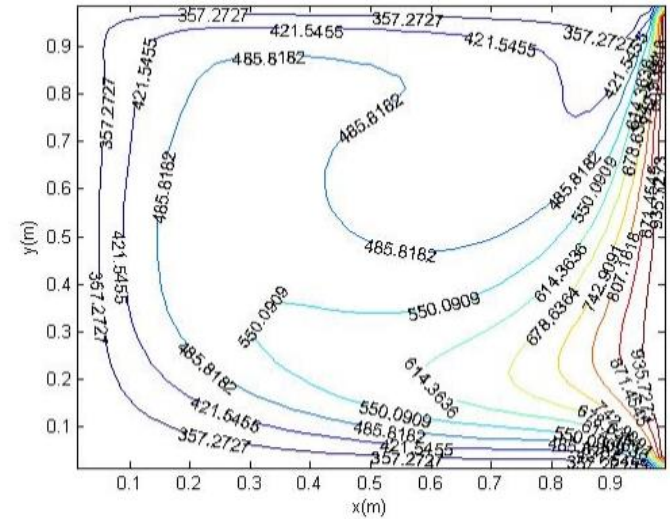


Figure 3.61. Variation of temperature for Reynolds number=400,  $dx=dy=1/40$ ,  $T_{\text{rightwall}}=1000$  K

Next, a case where  $T_{\text{rightwall}}=1000$  K and  $Re=1000$  is studied. In this case, due to the increased convective and diffusive transport, the gradients close to left, bottom and top walls are higher compared to previous cases.

Figure 3.62, Figure 3.64, and Figure 3.66 show the variation of density for different grid resolutions. Figure 3.63, Figure 3.65, and Figure 3.67 show the variation of temperature for different grid resolutions.

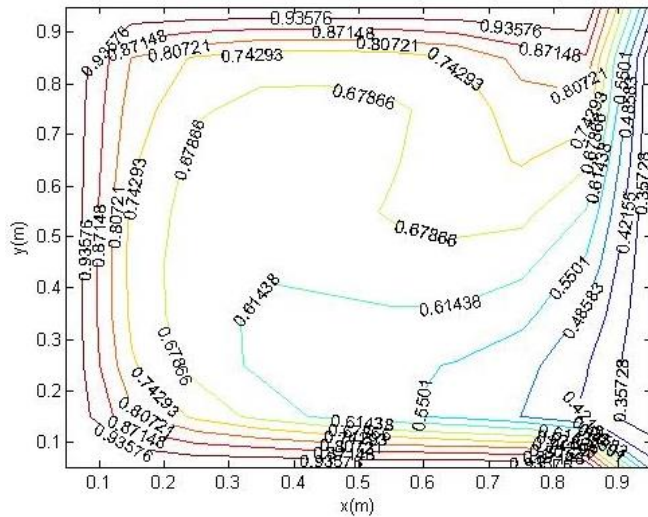


Figure 3.62. Variation of density for  $Re=1000$ ,  $dx=dy=1/10$ ,  $T_{rightwall}=1000$  K

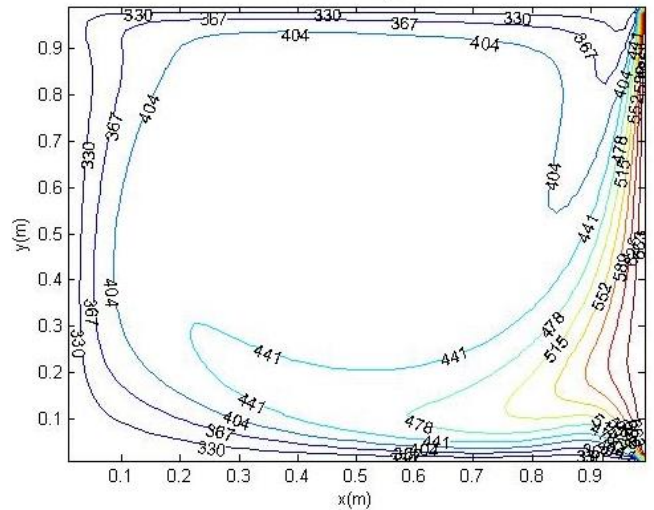


Figure 3.63. Variation of temperature for  $Re=1000$ ,  $dx=dy=1/10$ ,  $T_{rightwall}=1000$  K

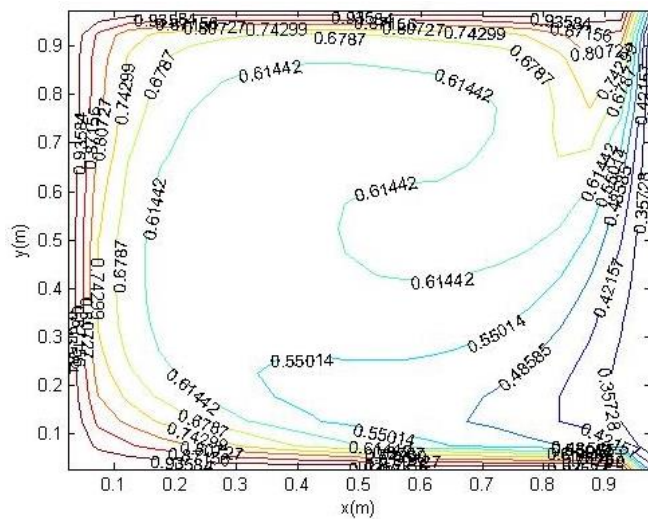


Figure 3.64. Variation of density for  $Re=1000$ ,  $dx=dy=1/20$ ,  $T_{rightwall}=1000$  K

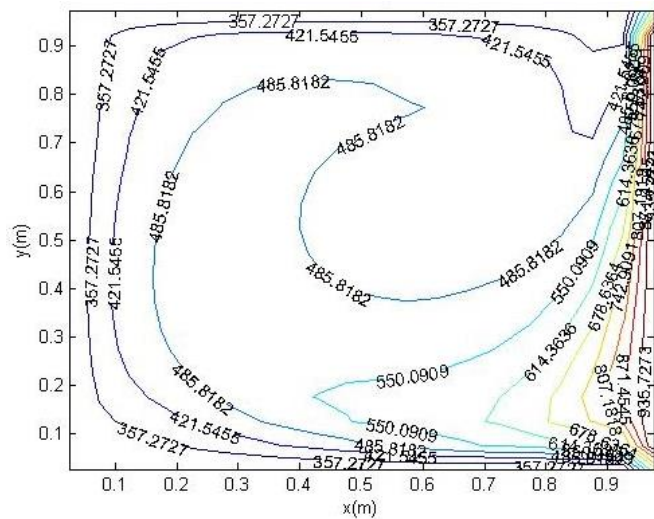


Figure 3.65. Variation of temperature for  $Re=1000$ ,  $dx=dy=1/20$ ,  $T_{rightwall}=1000$  K



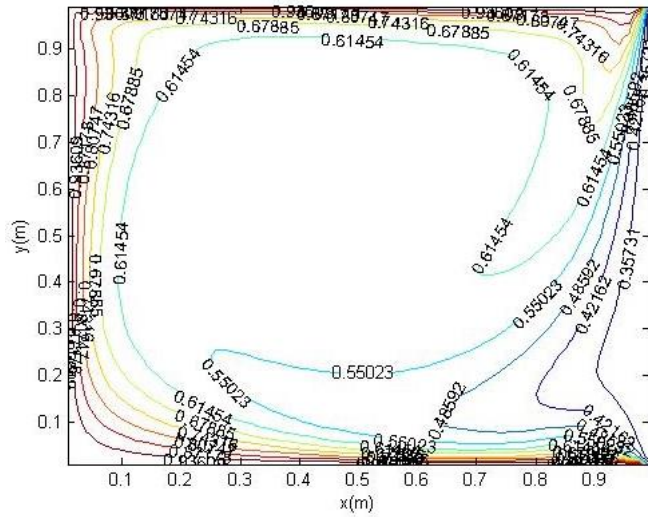


Figure 3.66. Variation of density for  $Re=1000$ ,  $dx=dy=1/40$ ,  $T_{rightwall}=1000$  K

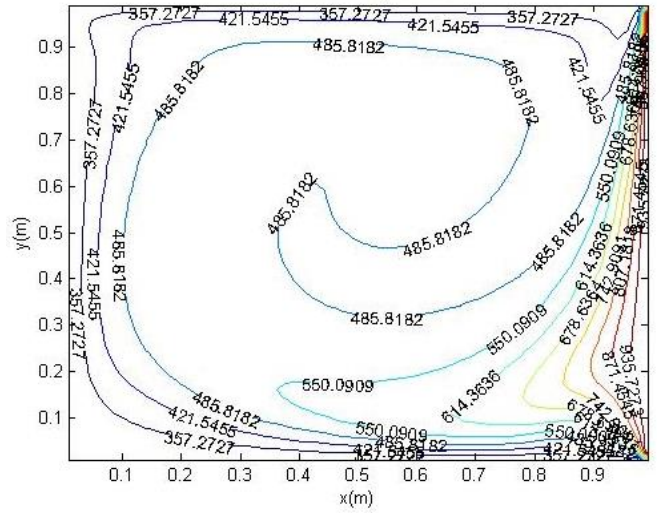


Figure 3.67. Variation of temperature for  $Re=1000$ ,  $dx=dy=1/40$ ,  $T_{rightwall}=1000$  K

For the  $Re=100, 400, 1000$  solutions where the right wall is kept at 1000 Kelvins, error analysis has also been performed. For the error analysis, a finer grid resolution ( $dx=dy=1/60$ ) has been selected as the benchmark solution. Middle point  $u$  velocity of the reference solution has been selected as the target value. The results obtained with coarser grids then have been compared with this value.

Figure 3.68, Figure 3.69, and Figure 3.70 illustrate error plots for the absolute error obtained in this manner.

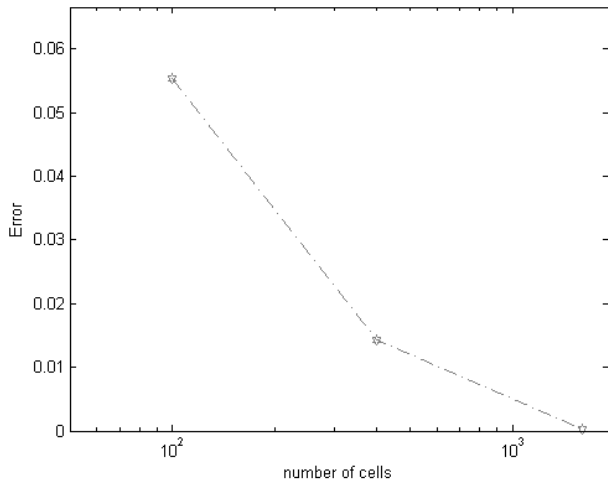


Figure 3.68. Midpoint  $u$  velocity absolute error variation with grid density,  $Re=100$ ,  $T=1000$  K

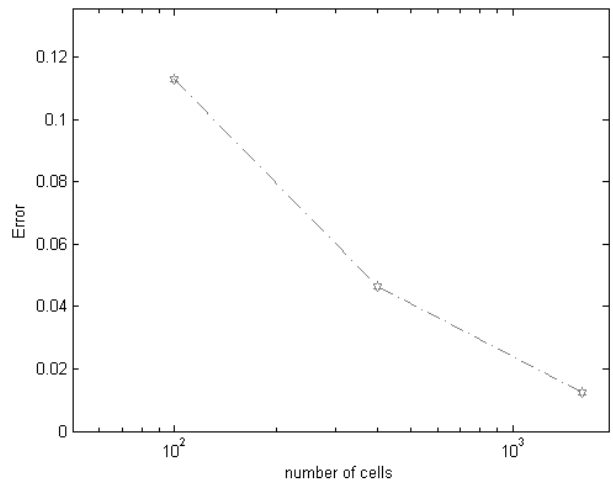


Figure 3.69. Midpoint  $u$  velocity absolute error variation with grid density,  $Re=400$ ,  $T=1000$  K

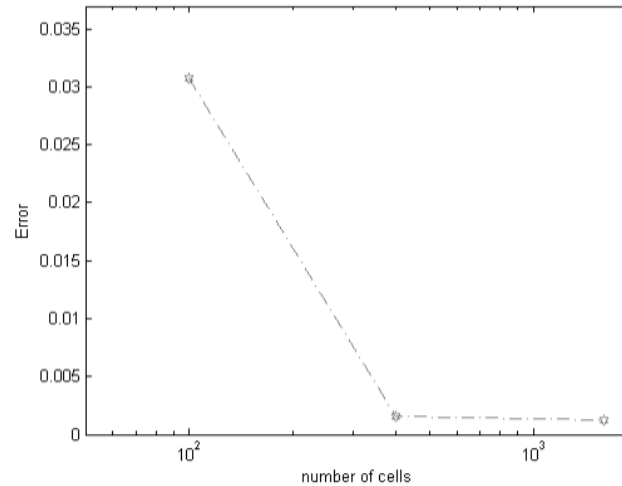


Figure 3.70. Midpoint u velocity absolute error variation with grid density, Re=1000, T=1000 K

### 3.3 DISCUSSION OF THE RESULTS

As can be seen from the above plots, higher Re number flows (hence higher convection) results in steeper temperature and density gradients. On the other hand, increasing the right wall temperature value at a given Re number makes the solution more diffusion dominated and higher temperature penetrates further towards the left wall. Similar behaviour is observed in the general convection diffusion type of equations. For this reason, the result is found to be quite reasonable.

### 3.4 COMBINED CODE

In this part, incompressible and compressible solutions are brought together in a single code to enhance the convergence characteristics of compressible solution. The u, v, and P fields found by incompressible solution is used in the compressible flow field simulation as an initial condition. The choice of error criteria selection on the convergence characteristics has been investigated.

#### 3.4.1 Fixed pseudo-temporal advancement for incompressible and compressible solutions

Previous simulations have shown that after t=6 s continuity residual is well below  $1e^{-5}$ . Simulation is split into two parts: t=3 s was spent on the incompressible solution and

the remaining 3 seconds on the compressible solution. For a reference Reynolds number of 400 (defined according to top lid velocity and initial density) the simulation with fully compressible code takes 60 seconds to finish while the combined code takes 42 seconds to complete. This indicates a 30% improvement.

### **3.4.2 Fixed residual for incompressible and compressible solutions**

An error criteria is defined for compressible flow (mass flux error residual of  $10^{-6}$ ,  $10^{-5}$  etc.) and a higher (typically 100 times higher than compressible error tolerance) is used for the incompressible solution. This approach also enhances convergence, but enhancement is less compared to part a). Although not tried yet, it has been anticipated that if temperature field is roughly obtained without using density variations in the incompressible solution, further enhancement in the convergence can be possible.

## 4. PROBLEM OF INTEREST 2- IMPINGING JET FLOW

### 4.1 LITERATURE SURVEY FOR THE PROBLEM

Impinging jet flow is a type of flow phenomenon that is important especially for cooling problems and associated complex flow fields. Turbine blades, annealing of metal and plastic sheets, the tempering of glass are some of its important industrial applications. Glauert (1956) studied the problem for both laminar and turbulent flows and tried to develop analytical solutions for the laminar incompressible case. Riley (1958) developed a corresponding solution to account for the compressibility effects in laminar radial wall jets with stream function formulation and under the assumption of boundary layer formulation. The viscosity has been assumed to be directly proportional to temperature in the solution. The solution is not fully applicable for the general viscous case. Bakke (1957) has carried out experimental studies for the wall jet flow using Pitot tubes. Experimental setup is shown below. He did not include thermal effects in the experimental procedure.

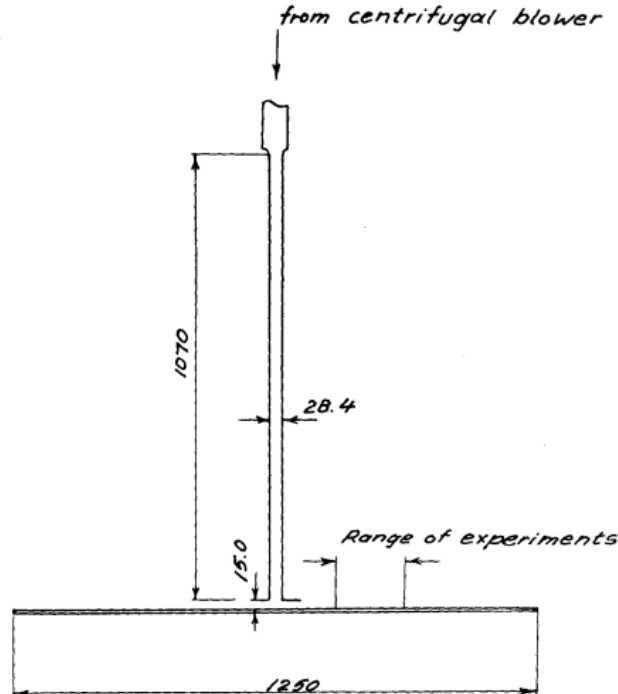


Figure 4.1. Experimental setup used by Bakke (1957)

Heiningen et al. (1976) used stream function formulation with finite difference discretisation to solve full set of Navier Stokes equations including energy equation in the laminar flow region. They used the Van Driest formula for the viscosity:

$$\frac{\mu}{\mu_r} = \left(\frac{T}{T_r}\right)^{1.5} * \left(\frac{T_r+110}{T+110}\right) \quad (4.1)$$

Where  $\mu_r$  is the reference viscosity at the reference temperature ( $T_r$ ) of 450 K. They compared the effect of flat and parabolic nozzle inlet velocities on velocity distribution for Reynolds numbers up to 1000.

Sezai and Mohammad (1999) studied the three-dimensional flow structure and heat transfer in laminar rectangular impinging jets for incompressible flow. They used staggered meshing and finite volume method. The convection terms are computed using QUICK scheme. SIMPLE algorithm has been used. For momentum and energy equations, an under-relaxation factor of 0.7 has been used. A 101x101x51 grid system has been used. Calculations have been performed up to the maximum Reynolds number of 500.

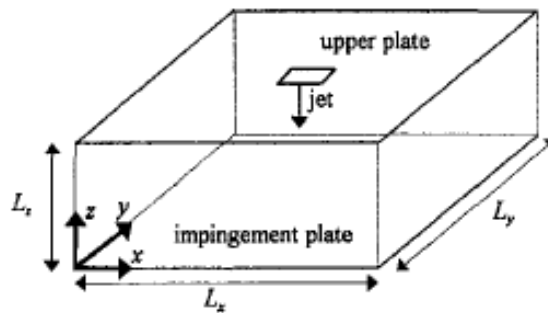


Figure 4.2. Solution domain used by Sezai and Mohammad (1999)

Turgeon et al. (1999) solved non-dimensionalized form of the Navier Stokes equations using the finite element method. Isothermal boundary conditions have been employed on the entrainment and impingement walls. On the exit section and at the inlet boundaries, the normal derivatives of temperatures are set to zero. For the impingement wall, effects of different temperature values on the flow and temperature fields have been investigated.

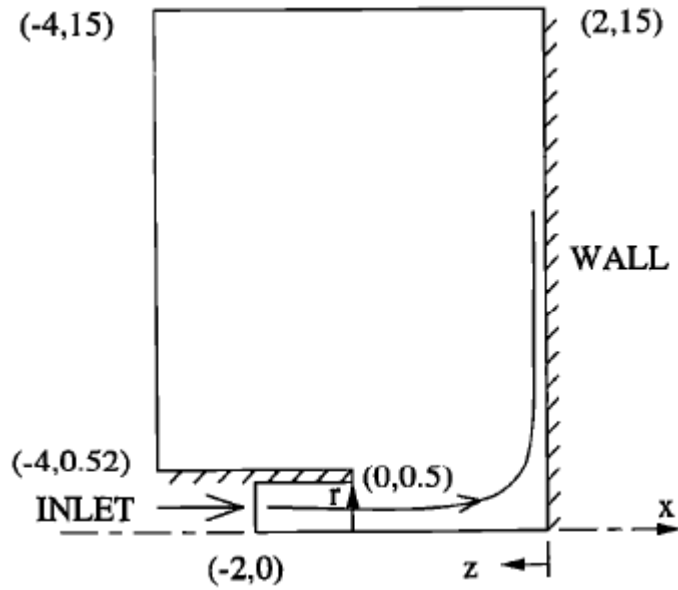


Figure 4.3. Domain used by Turgeon et al (1999)

Turgeon et al (1999) used unstructured mesh and a simple rectangular domain for the numerical solution.

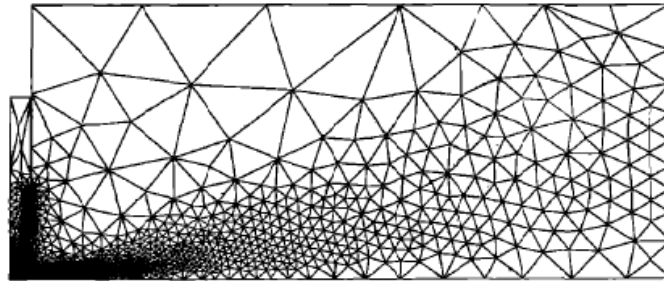


Figure 4.4. Mesh used by Turgeon et al. (1999)

Both air and CO<sub>2</sub> as working fluids have been investigated. For specific heat and viscosity, the values in Table 4-1 have been used between 280 K and 650 K.

Table 4-1 Simplified viscosity and temperature relations from Turgeon et al. (1999)

	Air	CO <sub>2</sub>
Cp/Cp <sub>r</sub>	$(T/T_r)^{0.5}$	$(T/T_r)^{0.34}$
$\mu/\mu_r$	$(T/T_r)^{0.68}$	$(T/T_r)^{1.5}(1+230/T_r)/(T/T_r+230/T_r)$
$\lambda/\lambda_r$	$(T/T_r)^{0.78}$	$(T/T_r)^{1.5}(1+(1440/T_r)^2)/((T/T_r)^2+(1440/T_r)^2)$

A pressure based finite element method has been employed by Turgeon et al (1999). Pressure difference at cells have been computed, they are added to the absolute pressure. Finally, density values at the cells have been obtained using the equation of state for a perfect gas. An extra approach where density is calculated as a function of temperature only (so called an elastic approach) has also been utilized. Turgeon et al. (1999) used different impingement wall temperatures to compare their effect on the wall skin friction coefficient. The solutions have been carried out for low Reynolds numbers.

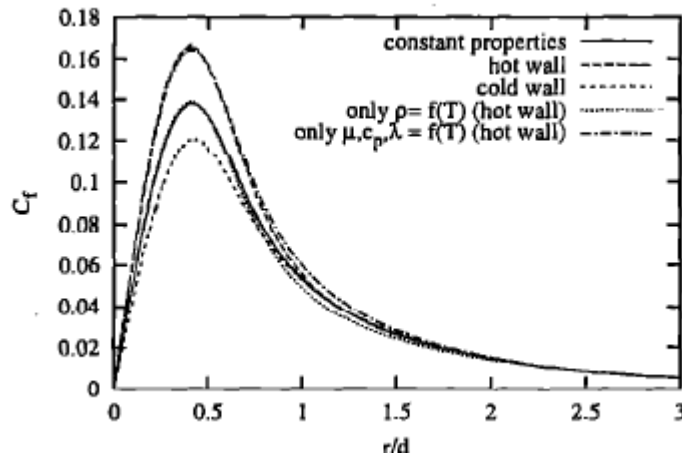


Figure 4.5. Skin coefficient values from Turgeon et al. (1999)

Dagtekin and Oztop (2008) studied heat transfer due to double laminar slot jets impingement. The domain is schematically shown in Figure 4.6. Incompressible form of the Navier–Stokes and energy equations were discretized with a finite volume procedure on a non-staggered grid arrangement using SIMLEM (SIMPLE-Modified) algorithm. The effect of the jet Reynolds number, the jet-isothermal bottom wall spacing, and the distance between two jets on heat transfer and flow field was examined. It is found that multi-cellular flow is formed in the impingement region due

to the interaction between two jets and entrainment effects in the duct. Under-relaxation factor of 0.5 was used for all variables. The power-law difference scheme is used to discretize the convective terms and central differencing for the diffusion terms. Reynolds numbers of 250, 500, and 750 have been investigated. For  $Re=250$ , velocity contours are shown in Figure 4.7. Left and top walls are taken as adiabatic while the bottom wall and the right boundary are taken as isothermal. Non-dimensionalized forms of the variables have been used in the solution. Isotherms for  $Re=250$  are shown in Figure 4.8.

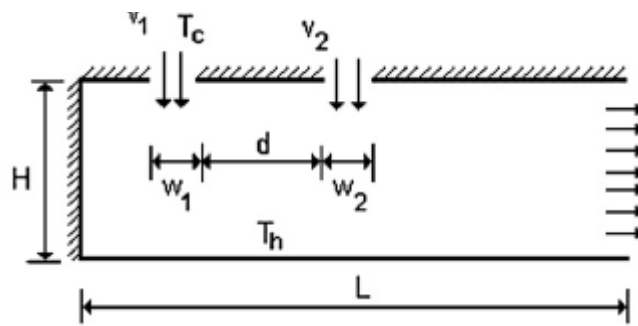


Figure 4.6. Solution domain used by Dagtekin and Oztop (2008)

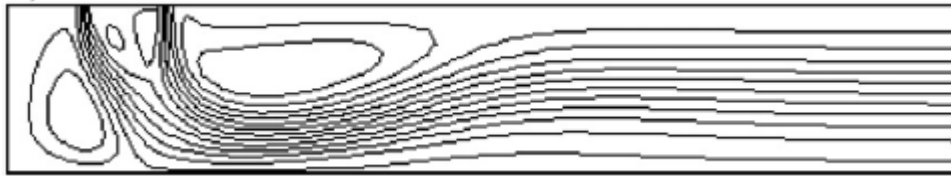


Figure 4.7. Flow field at  $Re=250$ ,  $H/W=4$ ,  $d/W=5$  from Dagtekin and Oztop (2008)

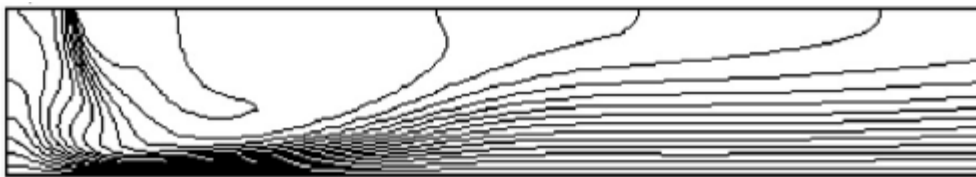


Figure 4.8. Isotherms at  $Re=250$ ,  $H/W=6$ ,  $d/W=5$  from Dagtekin and Oztop (2008)

Chou and Hung (1994) studied impingement cooling of an isothermally heated surface with a single jet. Incompressible and laminar flow for a Newtonian fluid with constant properties has been assumed. Furthermore, the viscous dissipation is



neglected in the energy equation. Non-dimensionalized form of the Navier Stokes equations has been used.

$$\left. \begin{aligned}
 X^* &= x/W_{\text{jet}}, \quad Y^* = y/W_{\text{jet}}, \\
 U^* &= uW_{\text{jet}}/\mu, \quad V^* = vW_{\text{jet}}/\mu, \\
 P^* &= P/(\rho^*v^2/W_{\text{jet}}^2) \\
 \Theta &= T - T_c / (T_h - T_c) \\
 Nu &= -\partial\Theta/\partial Y
 \end{aligned} \right\} \quad (4.2)$$

Power-law scheme with staggered grids has been employed by Chou and Hung (1994). SIMPLEC method presented by Van Doormaal and Raithby (1984) is implemented for steady-state solution. The following correlation approximates the relation between Nusselt number, Reynolds number and impingement domain height to impingement nozzle width,  $C_2$  is a parameter that depends on the impingement nozzle jet exit velocity profile.  $C_2=0.574$  is used for uniform nozzle jet velocity.

$$Nu_s = C_2 * Re_w^{0.5} * \left(\frac{H}{W}\right)^{-0.17} \quad (4.3)$$

Figure 4.9 shows the variation of Nusselt number on the bottom wall.

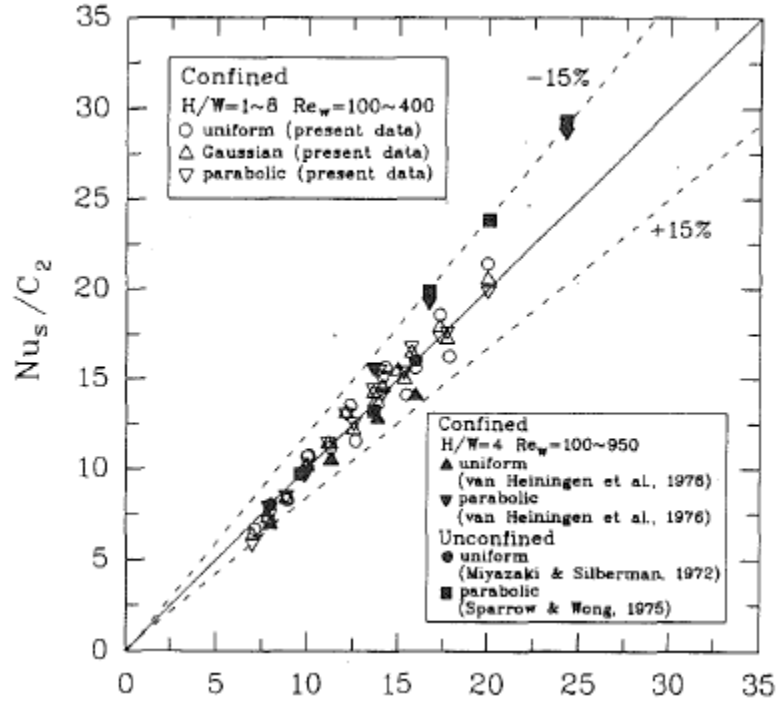


Figure 4.9. Nusselt number at the bottom wall from Chou and Hung (1994)

Chou and Hung (1994) also used Pohlhausen's analytical estimation of heat transfer on a flat plate and its modified form to get approximate solutions. Pohlhausen and modified Pohlhausen equations are given in Equations (4.4) and (4.5), respectively.

$$Nu_x = 0.332 * Pr^{\frac{1}{3}} * Re_w^{0.5} / X^{0.5} \quad (4.4)$$

$$Nu_{x,modified} = 0.295 * Re_w^{0.5} / (X - 0.5)^{0.5}, \text{ for } 3.5 \leq X \leq 10 \quad (4.5)$$

The comparison between numerical solution and analytical approximate approach is given in Figure 4.10.

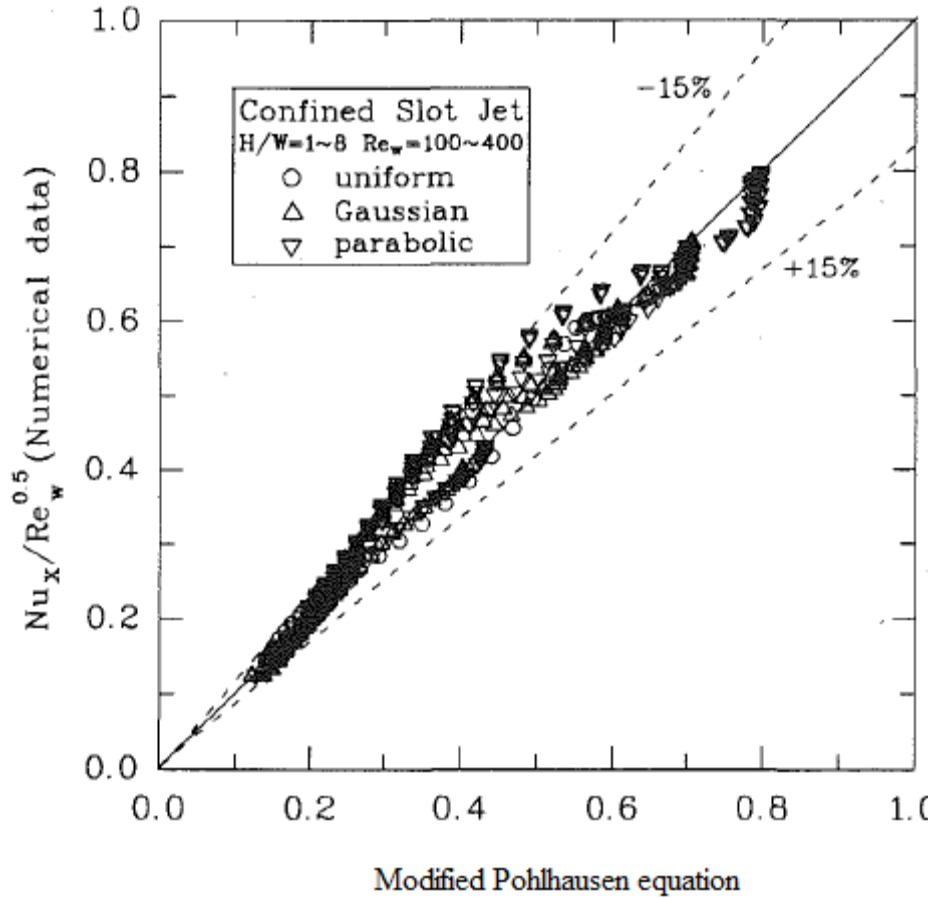


Figure 4.10. Modified Pohlhausen equation and numerical solution by Chou and Hung (1994)

Lorenzo et al. (2012) studied the impinging jet flow problem that is similar to the problem studied by Chou and Hung (1994). The domain is given in Figure 4.11. The material used in the study is water.

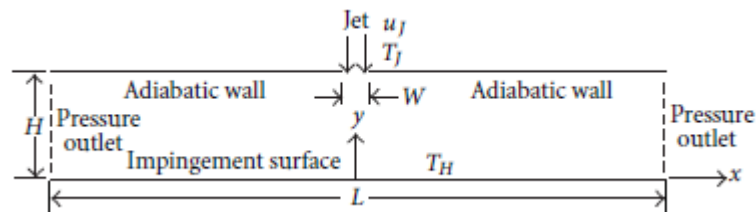


Figure 4.11. Domain studied by Lorenzo et al. (2012)

Lorenzo et al. (2012) used steady, laminar incompressible flow assumption and solved non-dimensionalized form of Navier Stokes equations. SIMPLE algorithm has

been utilized using Fluent software. They used 313 K bottom wall isothermal boundary condition and Boussinesq approximation to relate density variations to temperature. The jet temperature is specified at 293 K. So that there is a relatively small temperature difference between the boundaries.

The small temperature differential is essential for the accurate application of Boussinesq approximation. Boussinesq approximation is given by Gray and Giorgini (1975) as:

$$\rho = \rho_0 - \rho_0 \alpha_0 (T - T_0) \quad (4.6)$$

Gray and Giorgini (1975) specifies  $\alpha_0 = 3.5 \times 10^{-3}$  for air. The following criteria should be satisfied for the accurate modeling with Boussinesq approximation.

$$\alpha_0 (T - T_0) \ll 1 \quad (4.7)$$

Using  $T - T_0 = 100$  K, the above equation yields:

$$\alpha_0 (T - T_0) = 3.5 \times 10^{-3} \times 10^2 = 0.35 \quad (4.8)$$

This value (0.35) is not much small compared to 1 and validity of Boussinesq approximation is in question. So, if there is significant difference between boundary temperature values, use of a compressible fluid model is recommended.

Figure 4.12 shows the parameterized Nusselt number variation on the impingement wall. As expected, at the stagnation point just below the impinging jet, heat transfer and Nusselt number reaches maximum. Also, note that at relatively higher Reynolds numbers ( $Re=400$ ) a secondary local maximum in Nusselt number occurs. This can be due to the more complex character of the flow as Reynolds number increases. The vortex intensities increase as Reynolds number increase.

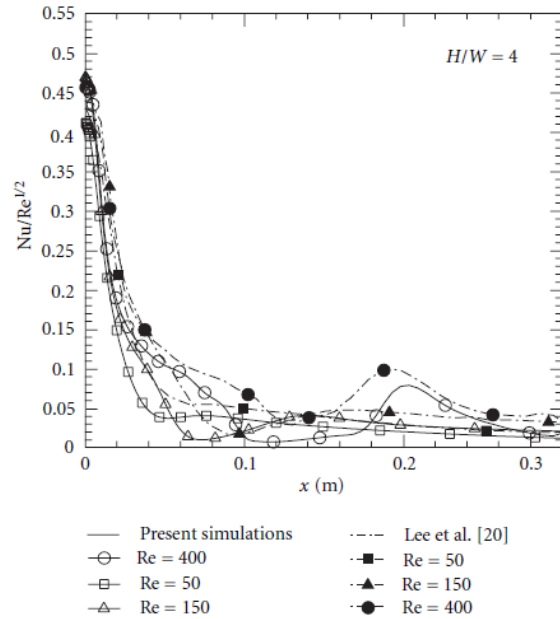


Figure 4.12. Nusselt number on the bottom wall from Lorenzo et al. (2012)

Figure 4.13 shows the variation of Nusselt number with Reynolds number. Increase in the Reynolds number results in enhanced heat transfer hence increased Nusselt number.

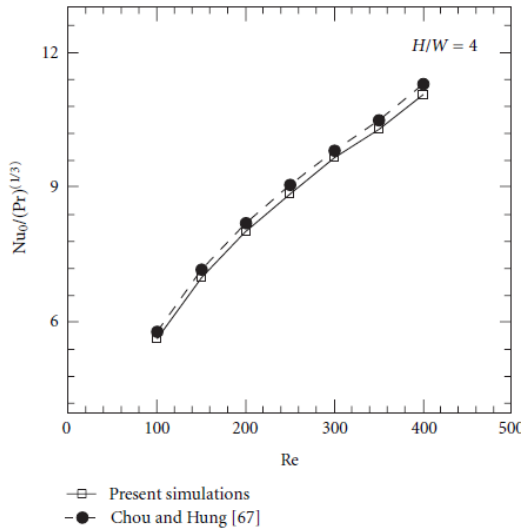


Figure 4.13. Variation of Nusselt number with Re from Lorenzo et al. (2012)

Chung and Luo (2002) modeled compressible impinging jet flow problem with direct numerical simulation. Direct numerical simulation (DNS) is used to study vortex

structures in more detail. In general, DNS simulations are very time consuming. Domain used in the study is given in Figure 4.14.

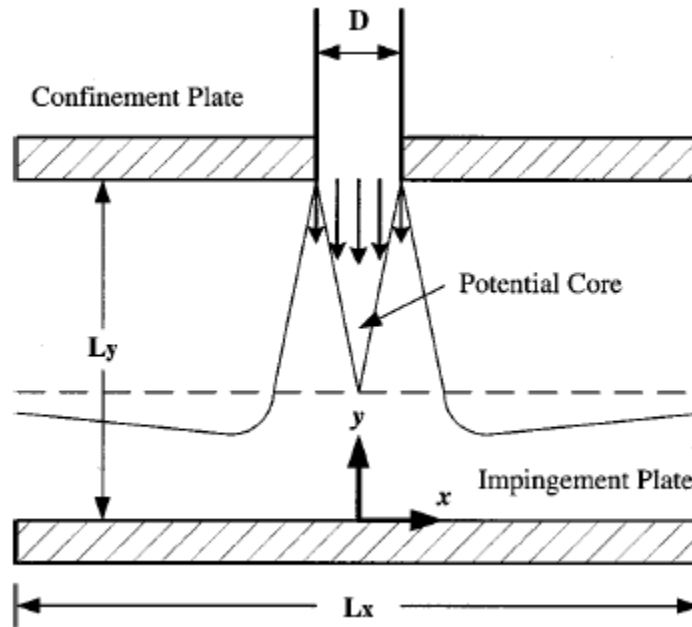


Figure 4.14. Domain used in Chung and Luo (2002)

Chung and Luo (2002) used air as the working fluid. Non-dimensionalized Navier Stokes equations have been solved. Very fine grids (up to 384x384) have been utilized. Test cases are illustrated in Table 4 2.

Table 4-2 Test cases used by Chung and Luo (2002)

Case	Re	Lx	Ly	Mesh sizes
1	300	10	10	256 <sup>2</sup>
2	500	10	10	300 <sup>2</sup>
3	1000	10	10	384 <sup>2</sup>
4	300	8	4	256 <sup>2</sup>
5	500	8	4	256 <sup>2</sup>
6	1000	8	4	256 <sup>2</sup>

Chung and Luo (2002) compared the numerical results with the experimental results given by Sparrow and Wong (1975).

The comparison of Nusselt numbers for the height to nozzle width ratio ( $H/W$ ) of 10 is illustrated in Figure 4.15.

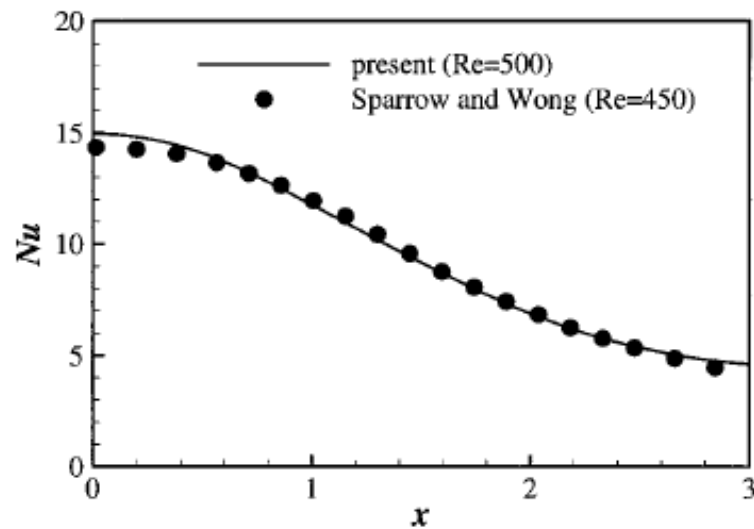


Figure 4.15. Experimental and numerical Nusselt numbers for  $H/W=10$  from Chung and Luo (2002)

Figure 4.16 shows the results for the variation of Nusselt number with different Reynolds numbers up to 1000 taken from Chung and Luo (2002). The formation of a secondary local maximum is attached to the stronger secondary vortices as Reynolds numbers increase.

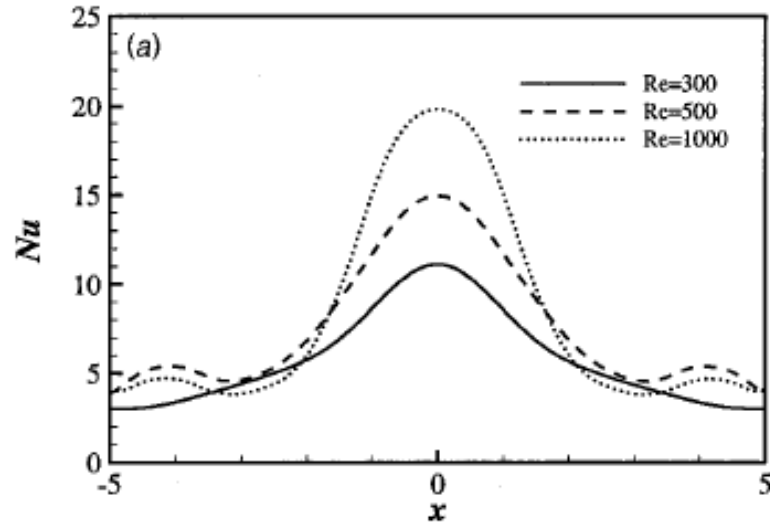


Figure 4.16. Variation of Nusselt number with Reynolds number from Chung and Luo (2002)

Chung and Luo (2002) also studied vortex structures. They concluded that above  $Re=500$ , secondary vortex is clearly evident. This is illustrated in Figure 4.17.

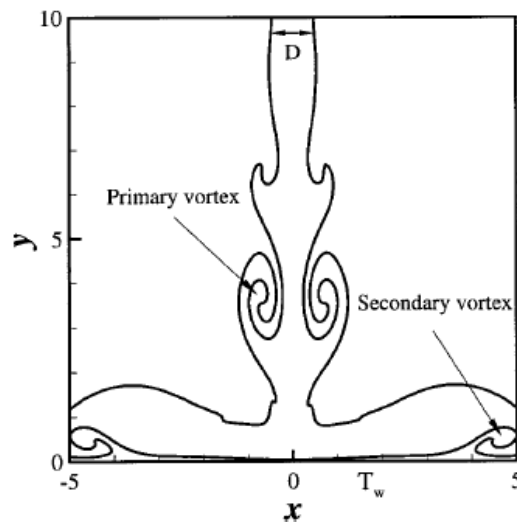


Figure 4.17. Vortex structure at  $Re=500$  from Chung and Luo (2002)

Tahsini and Mousavi (2012) studied the laminar compressible impinging jet problem for flat and curved plates. They used domain height to nozzle width ratio ( $H/b=H/W=2$ ) for the analyses. They noted that Nusselt number varies approximately



linearly with  $Re^{0.5}$  for laminar flows. At the stagnation point,  $Nu/Re^{0.5}=0.48$ . The data obtained in this study have been compared with Lee et al. (2008) in Figure 4.18.

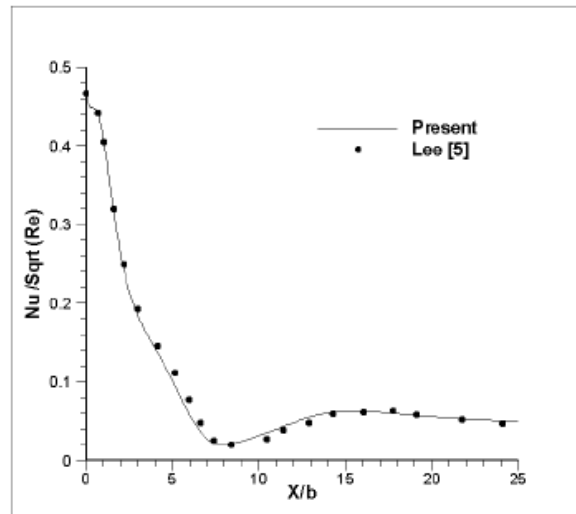


Figure 4.18. Nusselt number for flat plate at  $Re=300$ ,  $H/W=2$  from Tahsini and Mousavi (2012)

Narumanchi et al. (2005) studied liquid jet impingement cooling in power electronics. He studied the problem in two parts, first with single phase liquids and then with boiling liquid jets. He used water-glycol mixtures as the impingement liquid. He simulated average heat transfer coefficients on the impingement surface that is representative of chips. He carried out simulations with a commercial flow solver, Fluent. He then obtained velocity and temperature contours inside the domain.

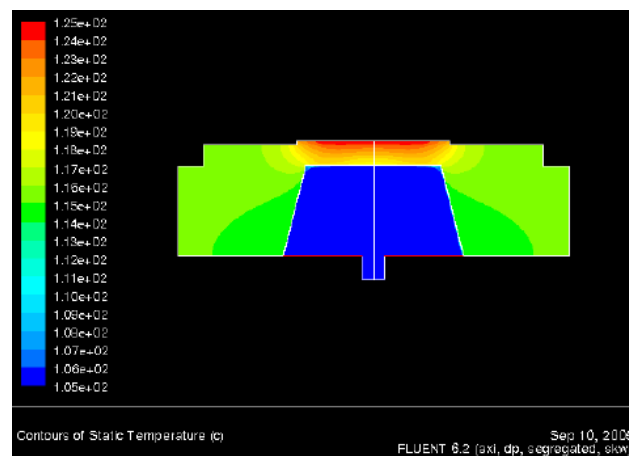


Figure 4.19. Jet impingement cooling isotherms from Narumanchi et al. (2005)

Shuja and Yilbas (2001) simulated the laminar jet impingement on to an adiabatic wall and investigated the effect of inlet velocity profiles. They utilized the axial and radial velocity components and momentum equations in axial and radial directions. A steady incompressible flow field has been assumed. First order upwind scheme has been used for the discretization of convective terms. SIMPLE scheme with staggered grid arrangement has been employed. A low Reynolds number of 50 has been used throughout the study. The domain used by Shuja and Yilbas (2001) is provided in Figure 4.20.

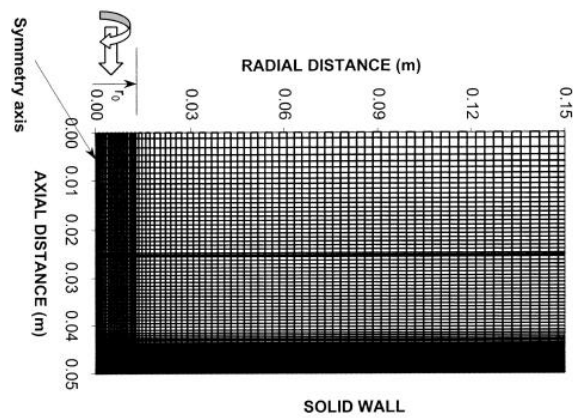


Figure 4.20. Domain used by Shuja and Yilbas (2001)

The jet exit velocity was defined as follows:

$$v_{\text{jet}} = v_{\text{max}} * \left( 1 - \left( \frac{r}{r_0} \right)^n \right) \quad (4.9)$$

Shuja and Yilbas (2001) then generated temperature and velocity profiles for different velocity profiles by changing the value of n.

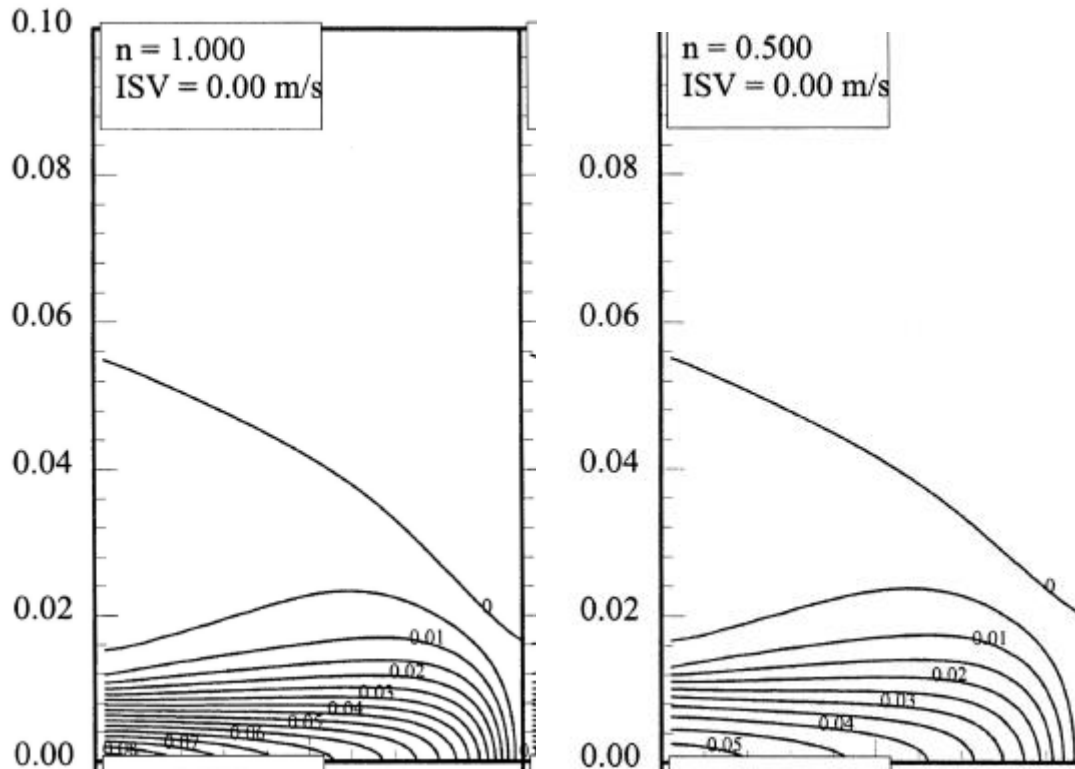


Figure 4.21. Axial velocity variation with changing jet exit profile from Shuja and Yilbas (2001)

Hadhrami et al. (2011) studied jet impingement problem with a focus on applications related to gas turbines. They studied the problem experimentally. They used jet diameters of 0.5 cm ( $d$ ) and jet Reynolds numbers of 18800. By varying the height of channel/jet nozzle diameter ( $H/d$ ) and jet spacing/jet nozzle diameter ( $X/d$ ) ratios, they obtained the Nusselt numbers on the impingement surface that is representative of a turbine blade. Setup used in this study is schematically shown in Figure 4.22.

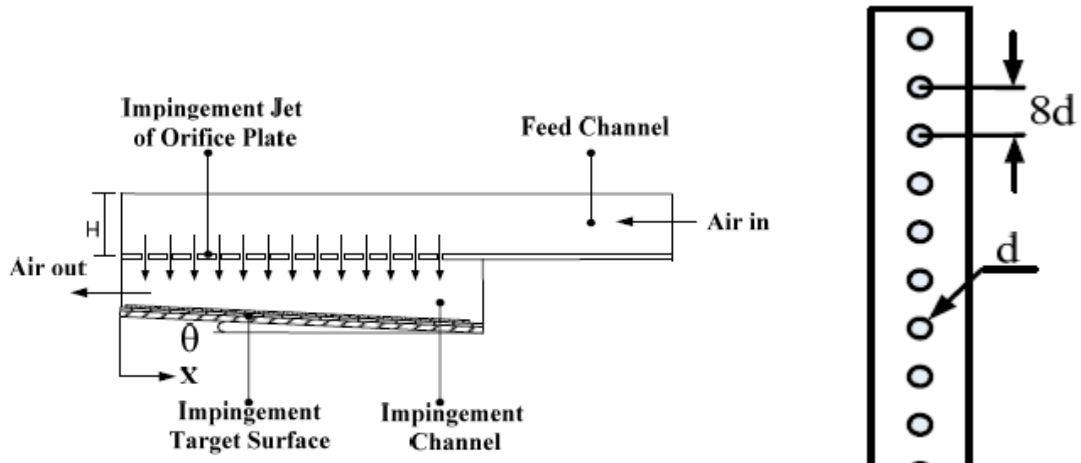


Figure 4.22. Experimental setup used by Hadhrami et al. (2011)

The variation of Nusselt number is shown in Figure 4.23.

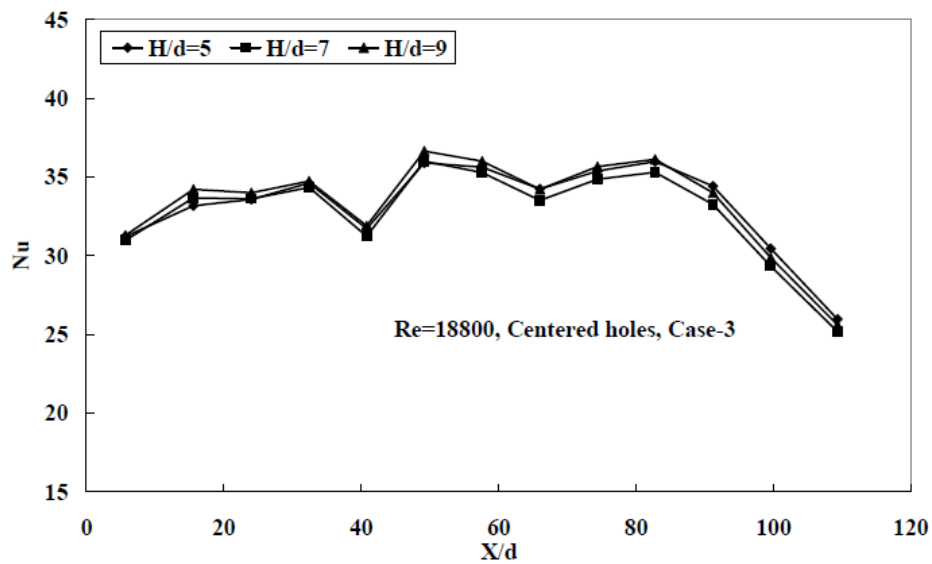


Figure 4.23. Variation of Nusselt number with different geometries from Hadhrami et al. (2011)

Sahoo and Sharif (2004) investigated cooling introduced by a single jet. Jet exit Reynolds numbers up to 500 have been investigated. They illustrated local and average Nusselt numbers at the hot surface. Domain used in the study is shown in Figure 4.24.  $L_x=10$ ,  $W/2=0.5$ ,  $L_y=1$  has been selected. Note that parameters are in non-dimensional form.  $q''=-1$ ,  $P_{outflow}=\text{constant}$  is used.

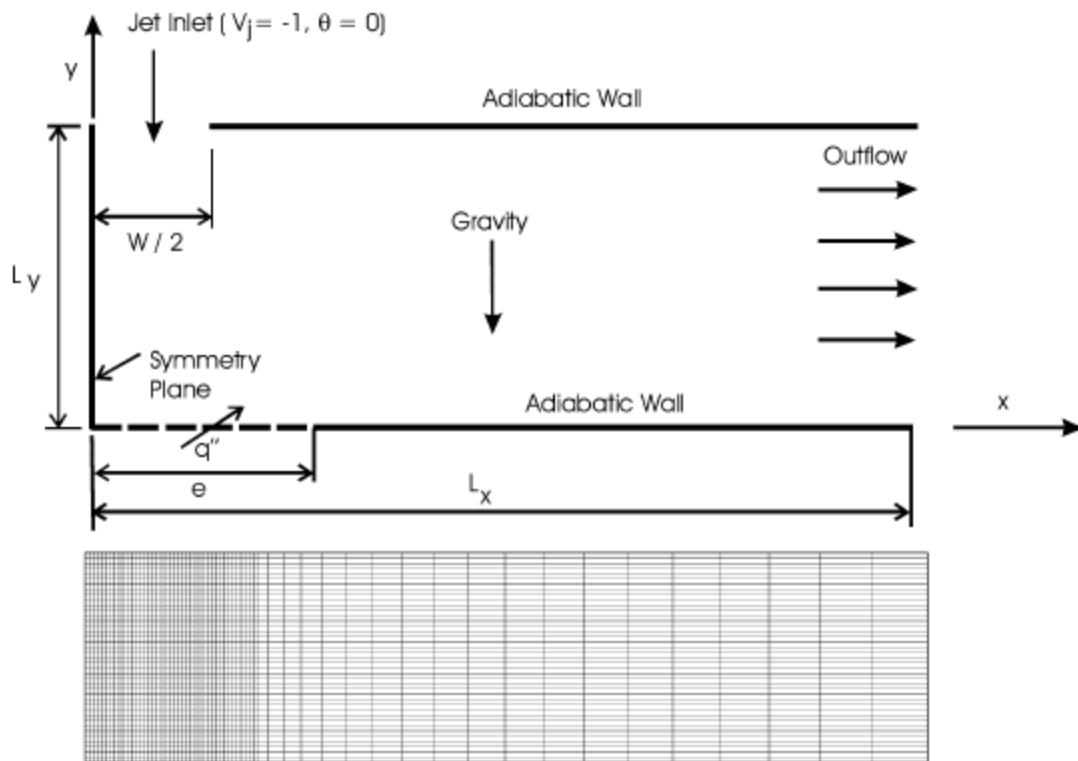


Figure 4.24. Solution domain used by Sahoo and Sharif (2004)

The steady state laminar incompressible flow assumption was used to solve the flow properties. PISO algorithm has been utilized for the solution of coupled system of equations. Second order upwind differencing is used for the discretization of convective terms. Central differencing is used for the calculation of diffusive terms. CFD2000 commercial solver has been utilized to solve the problem.

The results given in Figure 4.25 are obtained with  $Re=500$ .

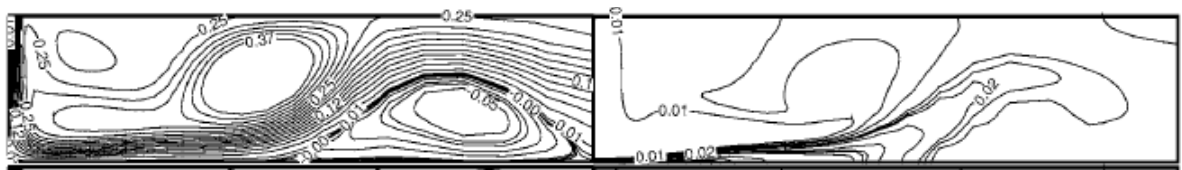


Figure 4.25. Velocity contours (left) and isotherms from Sahoo and Sharif (2004)

Nusselt number on the bottom source surface has also been studied. This is illustrated in Figure 4.26.

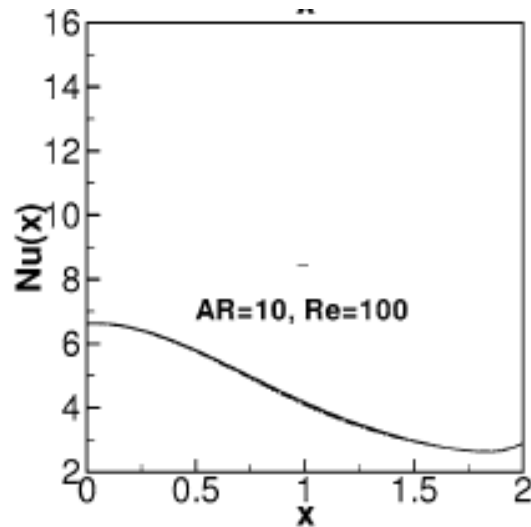


Figure 4.26. Nusselt number at the bottom wall from Sahoo and Sharif (2004)

In the analyses that are given in the next section, double impinging jet flows are studied. For double impinging jet flow, a solution domain similar to Dagtekin and Oztop (2008) with two intake slots are used. Dimensional form of Navier Stokes equations are solved. The results of the analyses are illustrated in the following sections.

#### 4.2 DOUBLE SLOT IMPINGING JET FLOW

A double slot impinging flow structure has been studied. Domain size of 2.5 x 0.5 m (LxH) has been used. Isothermal boundary conditions have been imposed. The bottom face is maintained at 500 K while the other boundaries are kept at 293 K.

Unsteady compressible Navier Stokes equations have been solved. Hybrid scheme has been employed for the discretisation of convective terms. SIMPLE scheme has been used to get the pressure field. Due to the temperature variation, energy equation has also been solved and density has been obtained in the domain. Choi(1999) momentum interpolation has been used to obtain face velocities. Different slot injection speeds have been used and its effect on the overall solution has been

studied. Results have been obtained for two different grids. Variables used are summarised in Table 4-3.

Table 4-3 Modelling parameters used for double slot impinging jet flow

<b>Variable name</b>	<b>Variable symbol</b>	<b>Value</b>
Width of nozzle 1	W	0.25
Width of nozzle 2	W	0.25
Domain height to nozzle width ratio	H/W	2
Domain length to nozzle width ratio	L/W	10
Prandtl number	Pr	1
Number of nodes in x direction	N <sub>x</sub>	102 to 202
Number of nodes in y direction	N <sub>y</sub>	22 to 42
Cell horizontal dimension	dx	1/40 to 1/80
Cell vertical dimension	dy	1/40 to 1/80
Reynolds number	Re	50 to 100
Injection velocity	V <sub>jet</sub>	-1 to -2 m/s
Time increment for the unsteady simulation	dt	dy/v <sub>jet</sub>
Freestream temperature	T	293 K
Lower boundary temperature	T	500 K
Outflow static pressure	P <sub>outflow</sub>	0
Time limit for unsteady simulations	t <sub>final</sub>	50 s

The slots are located between 0.25-0.5 m and 1.5-1.75 m from the top left edge.

Due to the impinging flow, cooling in the domain is realized. The cooling is more evident underneath the regions where slots are located. Density variation is greatly affected by the temperature.

The density field is illustrated in Figure 4.27 and Figure 4.29 for different grid resolutions. Results are close to each other. The density is affected by both pressure and temperature. However, the effect of temperature is higher on the density field compared to the effect of pressure on the density field. The temperature variation is illustrated in Figure 4.28 and Figure 4.30 for different grid resolutions.

It is seen in these figures that under the impingement nozzle exits, the predicted temperature and density values are lower due to the effect of velocity field. This manifests itself with the pocket like field structures under nozzle exits. Cooling underneath the nozzle jet exits is evident.

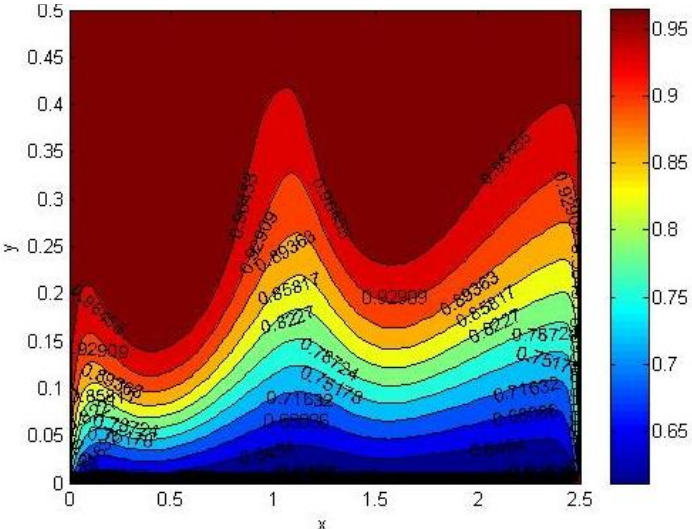


Figure 4.27. Density isolines for the double impinging flow,  $Re=50$ ,  $dx=dy=1/40$ ,  $v_{jet}=-1$  m/s

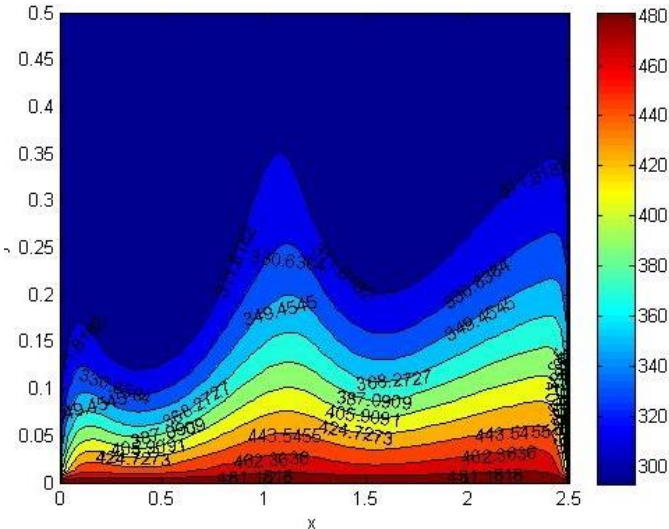


Figure 4.28. Isotherms for the double impinging flow,  $Re=50$ ,  $dx=dy=1/40$ ,  $v_{jet}=-1$  m/s



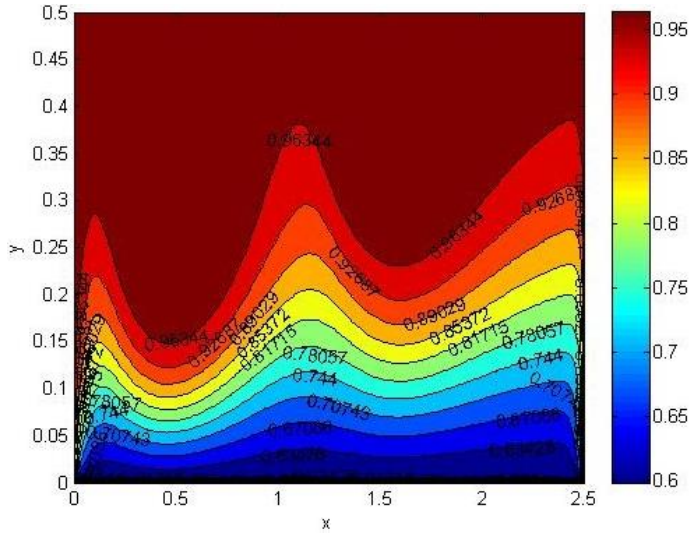


Figure 4.29. Density isolines for the double impinging flow,  $Re=50$ ,  $dx=dy=1/80$ ,  $v_{jet}=-1$  m/s

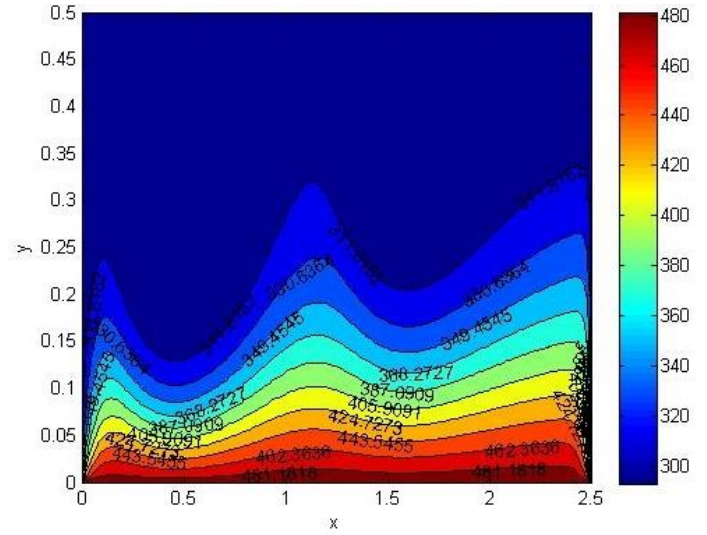


Figure 4.30. Isotherms (Kelvin) for the double impinging flow,  $Re=50$ ,  $dx=dy=1/80$ ,  $v_{jet}=-1$  m/s

Velocity contours are illustrated in Figure 4.31 and Figure 4.32 for different grid size. Strong vortices appear close to the impingement nozzle exits.

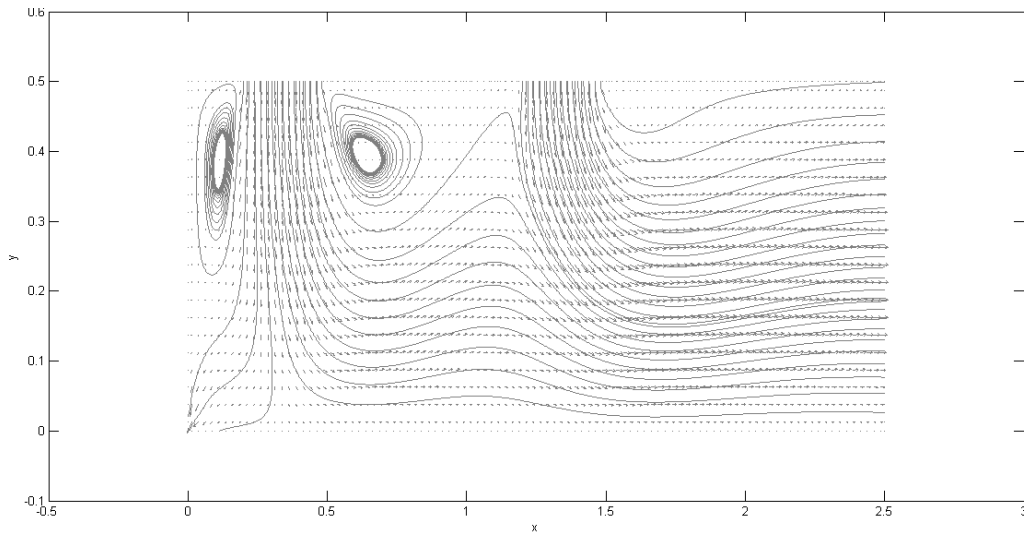


Figure 4.31. Velocity vector for the double impinging flow,  $Re=50$ ,  $dx=dy=1/40$

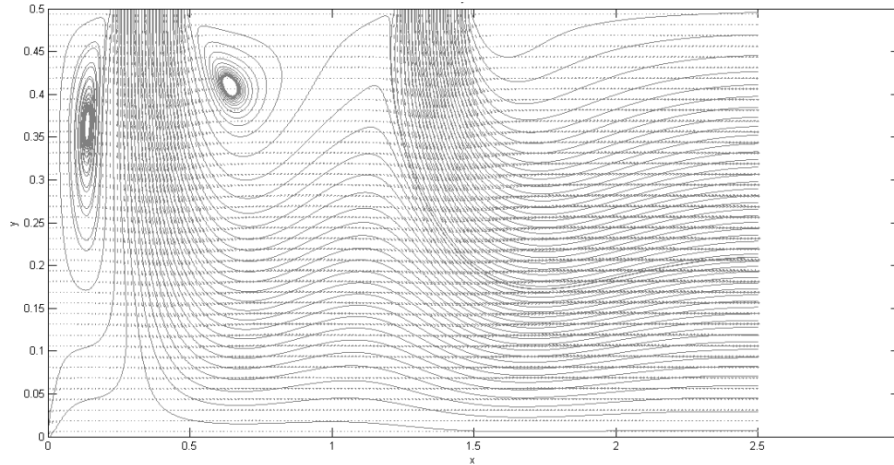


Figure 4.32. Velocity contours for the double impinging jet flow,  $Re=50$ ,  
 $dx=dy=1/80$

To increase the effect of cooling, impinging jet flow velocity has been increased by a factor of 2 and the solution has been repeated. In Figure 4.33 and Figure 4.35 temperature isotherms and in Figure 4.34 and Figure 4.36, density isolines have been illustrated. The results confirm a stronger cooling effect compared to the previous case where impinging jet velocity was lower. Predicted temperature values are lower in this case. Again the solution has been carried out for two different grid densities;  $dx=dy=1/40$  and  $dx=dy=1/80$ .

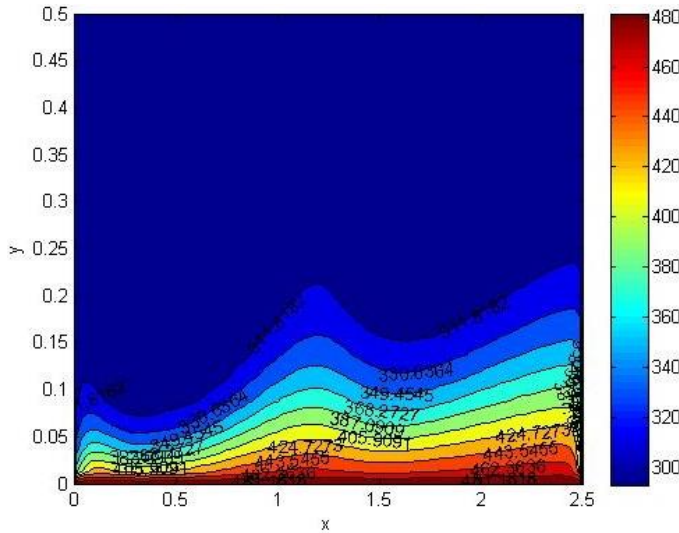


Figure 4.33. Isotherms (Kelvin) for the double impinging flow,  $Re=100$ ,  $dx=dy=1/40$ ,  $v_{jet}=-2$  m/s

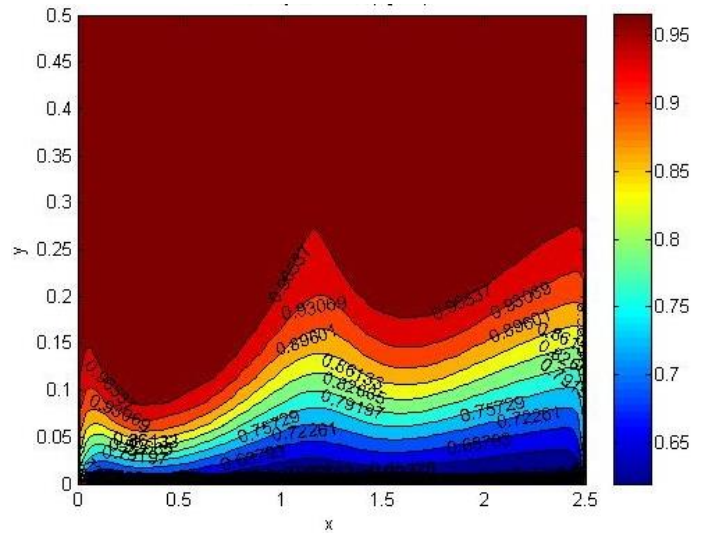


Figure 4.34. Density isolines for the double impinging flow,  $Re=100$ ,  $dx=dy=1/40$ ,  $v_{jet}=-2$  m/s

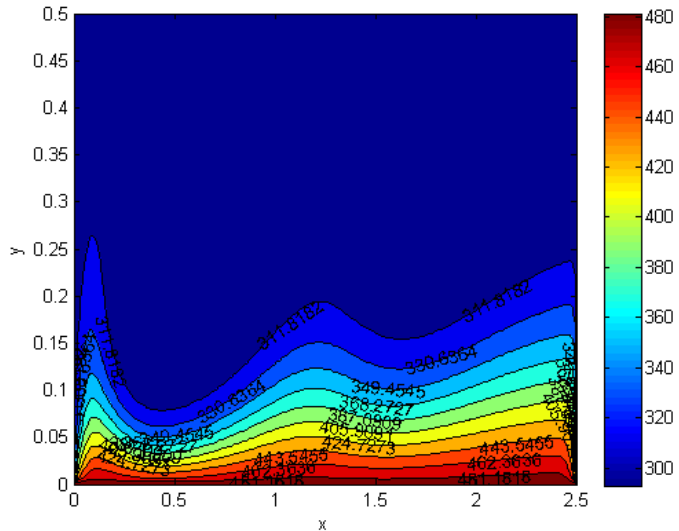


Figure 4.35. Isotherms (Kelvin) for the double impinging jet flow,  $Re=100$ ,  $dx=dy=1/80$ ,  $v_{jet}=-2$  m/s

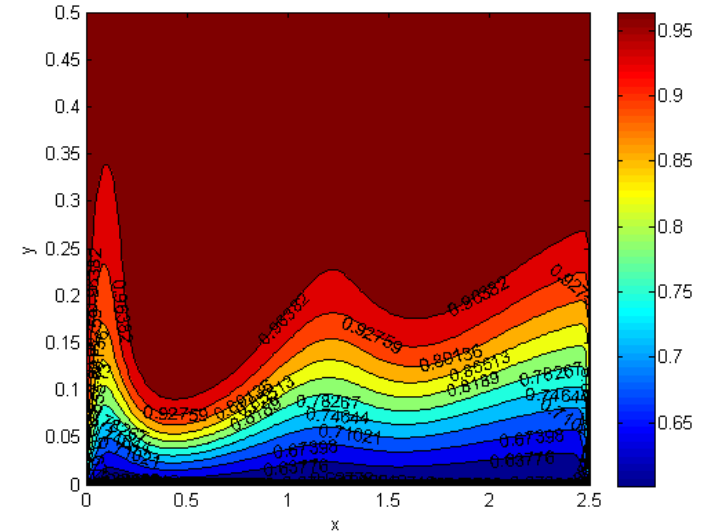


Figure 4.36. Density isolines for the double impinging jet flow,  $Re=100$ ,  $dx=dy=1/80$ ,  $v_{jet}=-2$  m/s

Velocity contours have been obtained for this configuration. These are given in Figure 4.37 and Figure 4.38 for two different grid resolutions. Vortices seem to grow in size with the increase in Reynolds number.

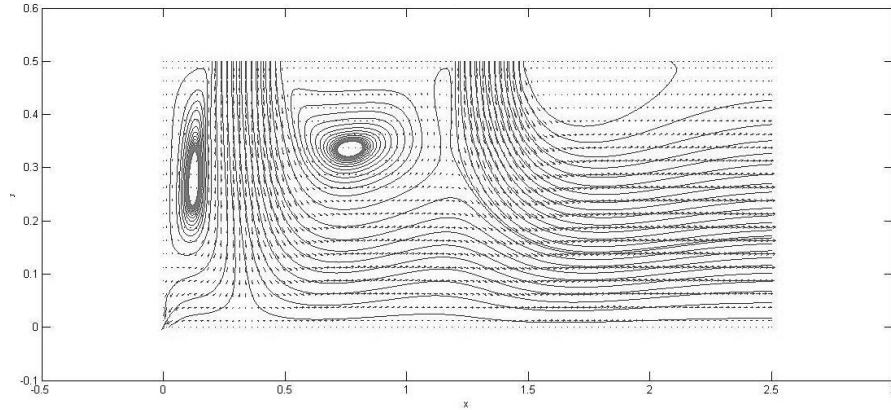


Figure 4.37. Velocity contours for the double impinging jet flow,  $Re=100$ ,  $dx=dy=1/40$ ,  $v_{jet}=-2$  m/s

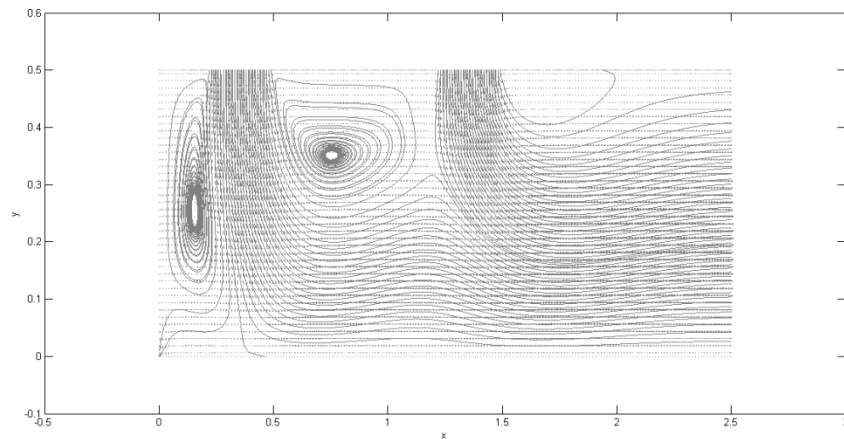


Figure 4.38. Velocity contours for the double impinging jet flow,  $Re=100$ ,  $dx=dy=1/80$ ,  $v_{jet}=-2$  m/s

Next, the solution has been performed with injection slots of different size. In the first case, slots are located at  $0.1 \cdot L - 0.3 \cdot L$ ,  $0.5 \cdot L - 0.7 \cdot L$ . Hence, slots are 2x wider. The solution has also been performed with a narrower slot width ( $w=0.02 \cdot L$ ).

The results are given in Figure 4.39 and Figure 4.41 for density and in Figure 4.40 and Figure 4.42 for temperature fields in the computational domain. Results indicate that with the narrower slot width, cooling is significantly reduced and with a wider slot width cooling is enhanced.

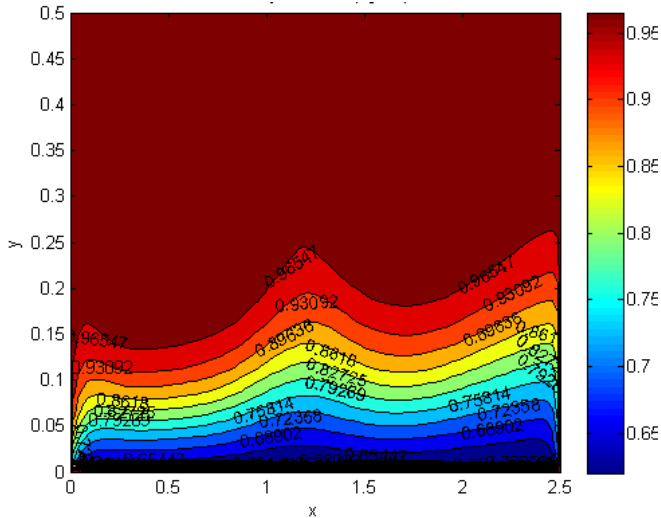


Figure 4.39. Density isolines for the double impinging flow,  $v_{jet}=-1$  m/s,  $dx=dy=1/40$ ,  $w=0.2*L$

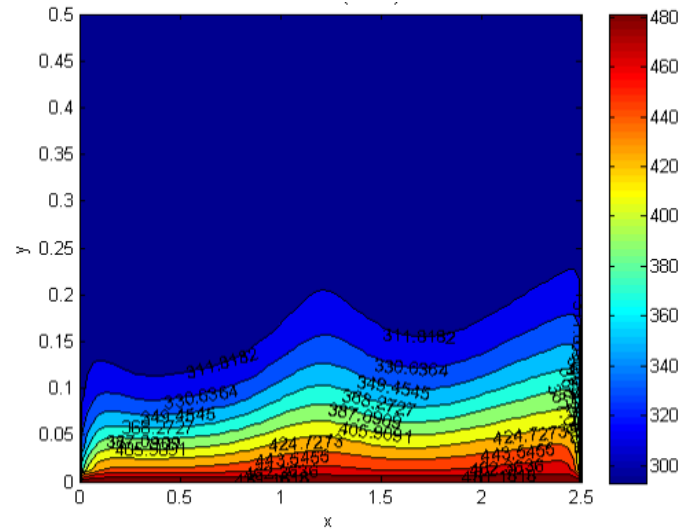


Figure 4.40. Isotherms for the double impinging jet flow,  $v_{jet}=-1$  m/s,  $dx=dy=1/40$ ,  $w=0.2*L$

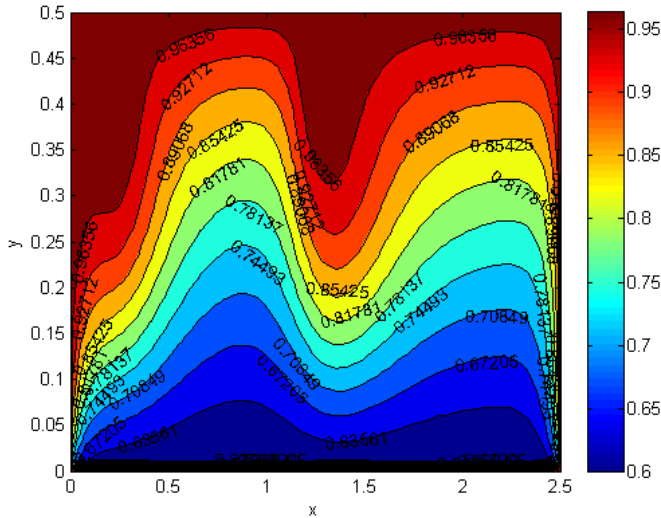


Figure 4.41. Density isolines for the double impinging flow,  $v_{jet}=-1$  m/s,  $dx=dy=1/40$ ,  $w=0.02*L$

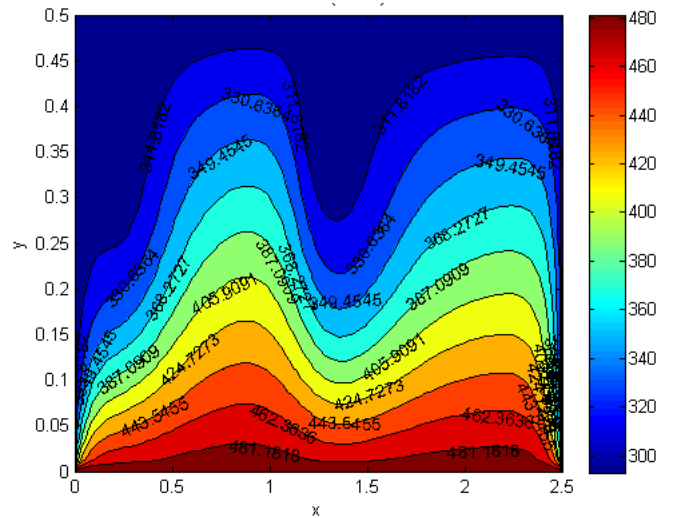


Figure 4.42. Isotherms for the double impinging jet flow,  $v_{jet}=-1$  m/s,  $dx=dy=1/40$ ,  $w=0.02*L$

Velocity contours for the different slot widths are illustrated in Figure 4.43 and Figure 4.44. For the narrow slot width, the mass flux is so weak that vortices are not visible.

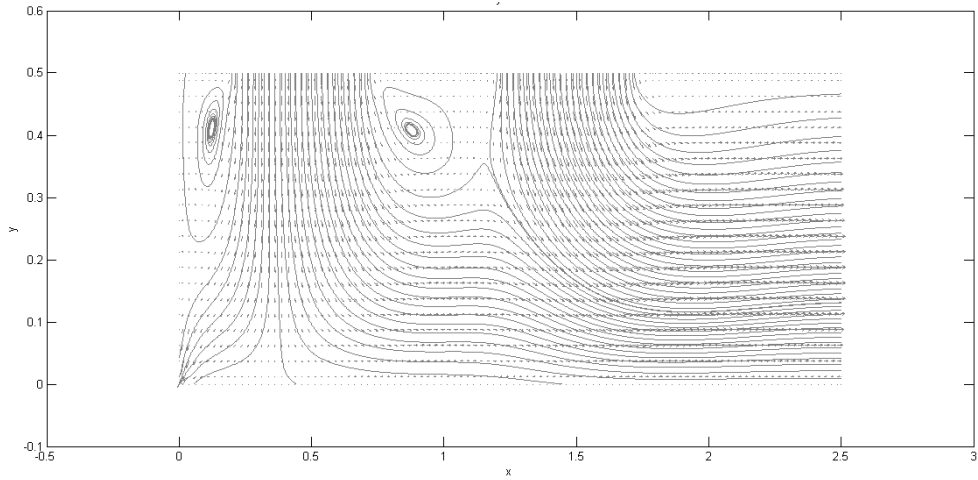


Figure 4.43. Velocity contours for the double impinging jet flow,  $v_{jet}=-1$  m/s,  $dx=dy=1/40$ ,  $w=0.2*L$

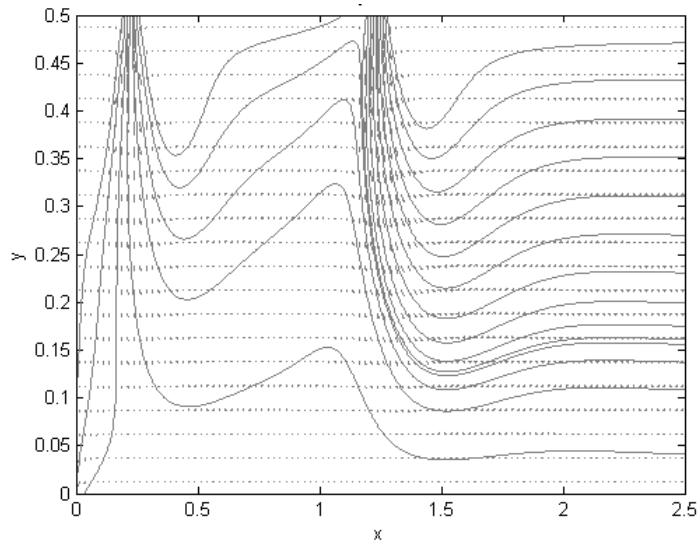


Figure 4.44. Velocity contours for the double impinging jet flow,  $v_{jet}=-1$  m/s,  $dx=dy=1/40$ ,  $w=0.02*L$

### 4.3 SINGLE SLOT IMPINGING JET FLOW

Single slot impinging flow has been studied using compressible form of Navier Stokes equations. Laminar flow has been assumed. Geometrical parameters for the single slot impinging flow are given in Table 4-4.

Table 4-4 Modelling parameters used for single impinging jet flow

Variable name	Variable symbol	Value
Width of nozzle	W	0.1
Domain height to nozzle width ratio	H/W	2
Domain length to nozzle width ratio	L/W	20
Prandtl number	Pr	0.71
Number of nodes in x direction	Nx	102
Number of nodes in y direction	Ny	42 to 102
Cell horizontal dimension	dx	1/50
Cell vertical dimension	dy	1/100 to 1/500
Reynolds number	Re	100 to 1000
Time increment for the unsteady simulation	dt	dy/v <sub>jet</sub>
Freestream temperature	T	293 K
Lower boundary temperature	T	393 K
Outflow static pressure	P <sub>outflow</sub>	0
Time limit for unsteady simulations	t <sub>final</sub>	50 s

Variation of Nusselt number is illustrated in Figure 4.45 for Reynolds number 100. As can be seen from the figure, heat transfer and Nusselt number is maximised at the stagnation point directly under the impingement nozzle. Nusselt number decays close to right boundary. A 102x42 grid system have been used.

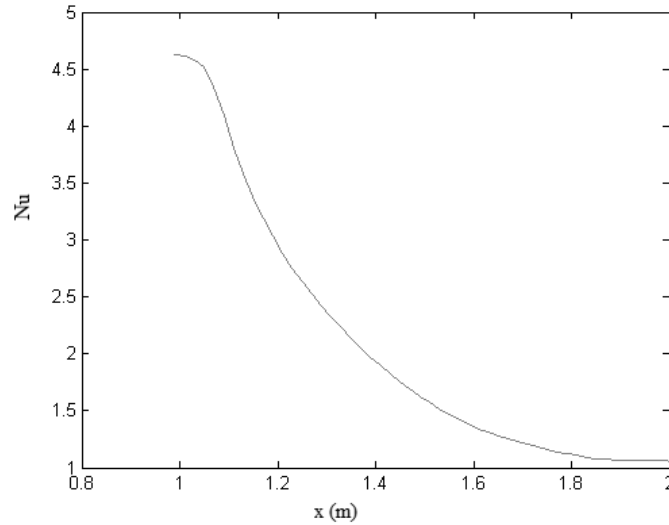


Figure 4.45. Variation of Nusselt number at impingement wall for Re=100

The result for Nusselt number variation is in accordance with the results in the literature.  $Nu/Re^{0.5}$  is **0.46** which is close to the value given by Tahsini and Mousavi (2012) for low Reynolds numbers specified as **0.48**.

Next, the flow with a Reynolds number of 300 has been studied to understand Nusselt number variation with Reynolds number. The relation given by Tahsini and Mousavi (2012) yields  $Nu=0.48*300^{0.5}= 8.3138$ . This time different grid resolutions from 102x42 to 102x102 has been used to better solve the vortex structures and understand the dependence of results on the grid resolution.

Figures 4.46 to 4.49 illustrate Nusselt number variation at the impingement wall for different grid resolutions. The result presented in Figure 4.49 yields  $Nu_s=8.3142$  for 102x102 nodes grid system which is almost the same with the result provided by Tahsini and Mousavi (2012) for compressible flows, given as **8.3138**. Note that there is notable difference between coarse grid and fine grid solutions in terms of Nusselt number variation.



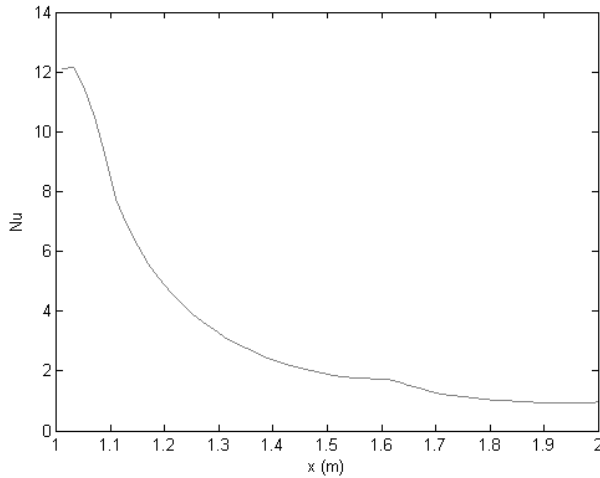


Figure 4.46. Variation of Nusselt number at impingement wall for  $Re=300$ , 102x42 grid

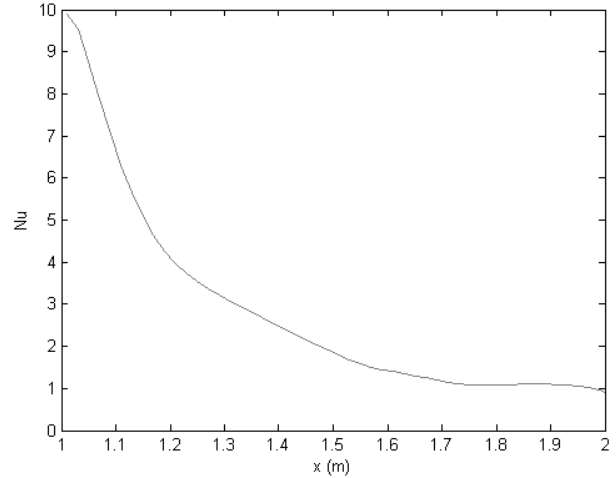


Figure 4.47. Variation of Nusselt number at impingement wall for  $Re=300$ , 102x62 grid

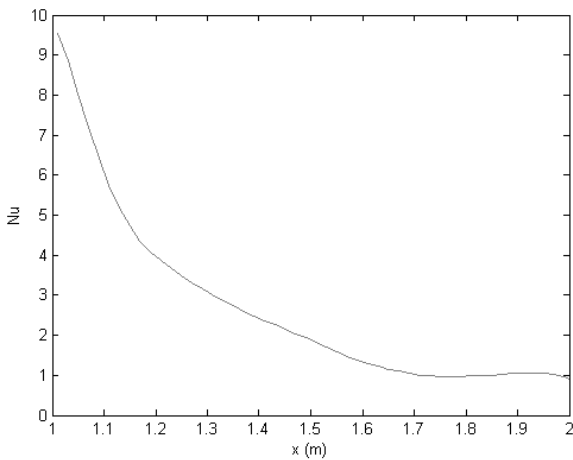


Figure 4.48. Variation of Nusselt number at impingement wall for  $Re=300$ , 102x82 grid

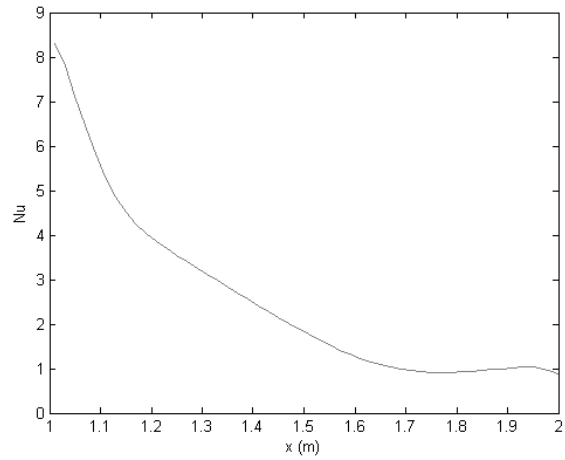


Figure 4.49. Variation of Nusselt number at impingement wall for  $Re=300$ , 102x102 grid

The variation of temperature is illustrated in Figure 4.50 for the finest grid solution. As can be seen, underneath the jet flow temperature cooling effect is more evident.

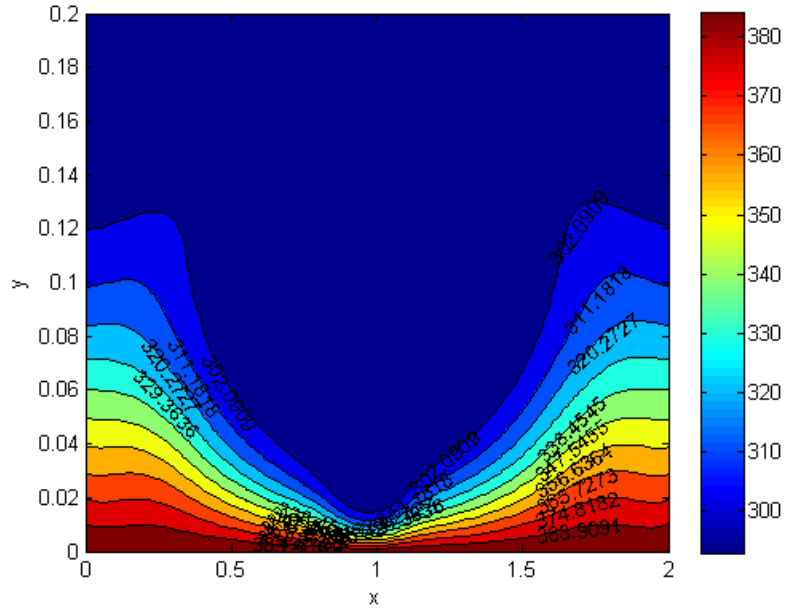


Figure 4.50. Variation of temperature for single impinging jet flow,  $Re=300$ , 102x102 grid

Next, the density variation has been studied. Figure 4.51 illustrates the density variation for the 102x102 nodes grid system. The density isolines follow a pattern similar (but not exactly equal) to temperature lines.

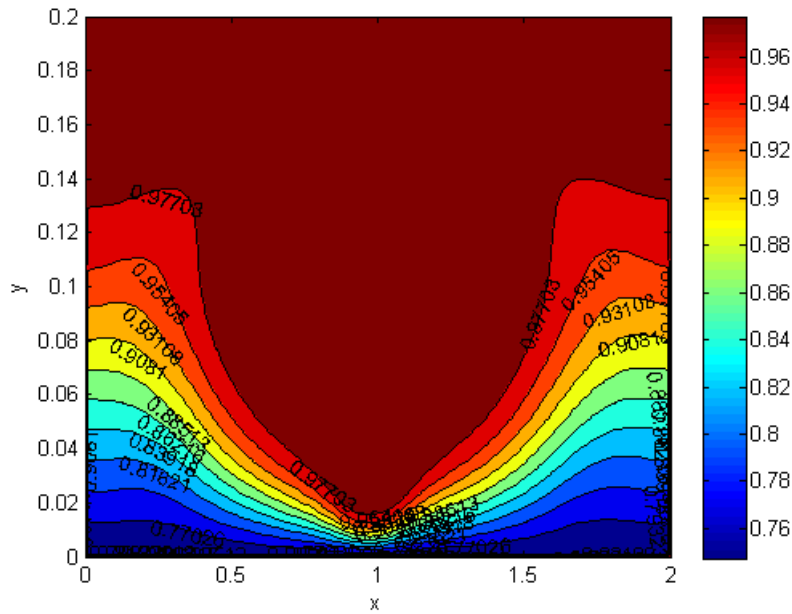


Figure 4.51. Variation of density for single impinging jet flow,  $Re=300$ , 102x102 grid

The velocity field has also been studied for the finest grid. The results show the primary vortex is clearly visible to the right and left of impingement nozzle exit at  $Re=300$  as illustrated in Figure 4.52.

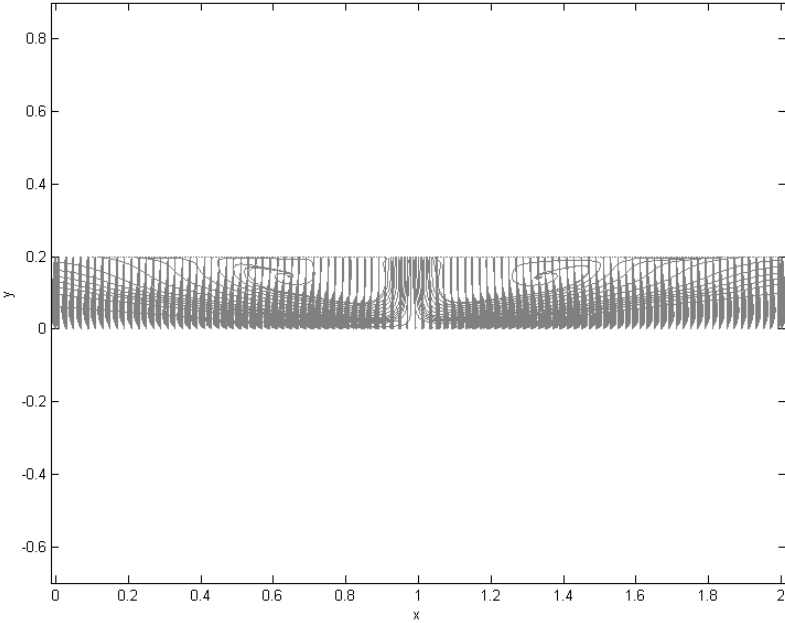


Figure 4.52. Velocity field for single impinging jet flow,  $Re=300$ ,  $102 \times 102$  grid

## 5. OPTIMISATION STUDIES

### 5.1 OPTIMISATION WITH GENETIC ALGORITHM

In this study, the genetic algorithm has been implemented for optimisation purposes. Use of optimization codes along with flow solvers have started in computational aerodynamics -especially for airfoil designs. The optimization procedures have been extended to other fluid flow problems.

Two main optimization routes are possible for fluid flow problems: gradient based optimization and evolutionary optimization. Gradient based approach is relatively faster in terms of convergence rate, but can get stuck at a local minimum more easily. Evolutionary approaches are more costly in terms of computing time requirement, but have a much lower chance of getting stuck to a local minimum. For multi parameter optimization problems, genetic algorithm is particularly interesting. It generates a family of solutions from which preferred solution couples are 'mated' to generate a more suitable family of solutions. The theory of the genetic algorithm is explored in Goldberg (1989) in detail.

Zhang et al. (2002) has studied the optimization of the airfoil and wing using genetic algorithm. Iannelli et al. (2012) has studied the optimization of high lift devices (flaps) using genetic algorithm. Dumas (2007) used genetic algorithm to study 3D simplified car exterior aerodynamic optimization. Tanner (2008) utilized the steepest descent optimization approach to explore the performance of different injection strategies in a diesel engine. Braembussche (2007) gives a detailed account of the use of genetic algorithm based optimization in conjunction with various turbomachinery problems.

The typical workflow of the genetic algorithm has been presented below.

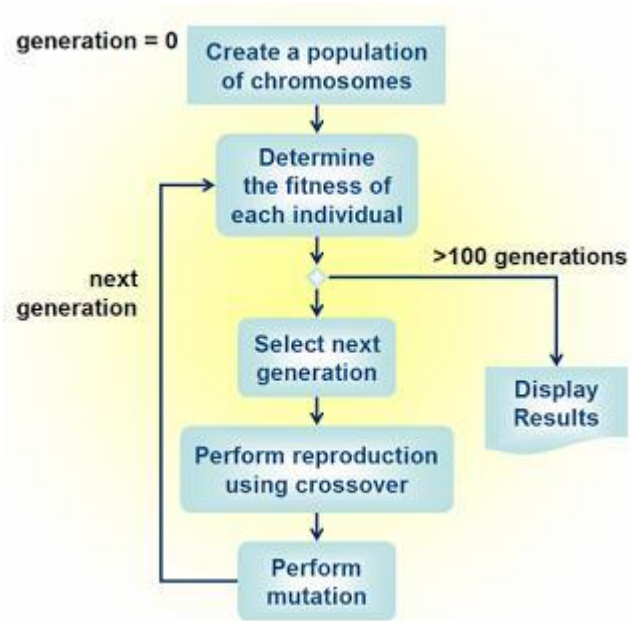


Figure 5.1. Schematic of Genetic Algorithm by Gupta (2016)

The behavior seen in the problems with a global minimum and with a global and local minimum has been represented in Figure 5.2 and Figure 5.3, respectively.

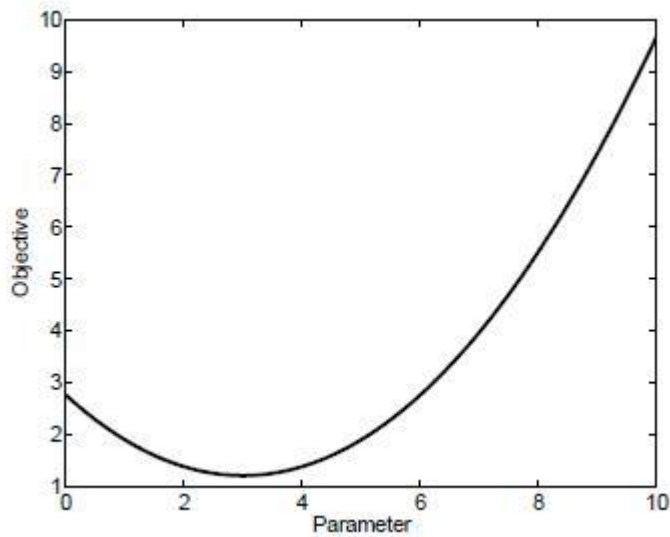


Figure 5.2. Problem with a global minimum

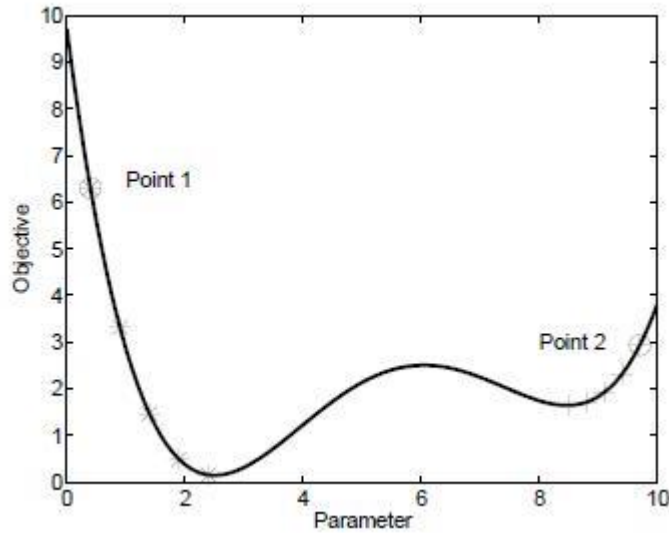


Figure 5.3. Problem with a global and local minimum

Genetic algorithm is finding new applications. Recently, Fabritius (2014) has applied genetic algorithm to optimize turbulence modeling parameters. He varied the turbulence related parameters in the  $k-\epsilon$  model. He solved the backward facing step problem at  $Re=64\ 000$  and utilized experimental data available as reference values. He utilised OPENFOAM finite volume solver.

Table 5-1 Turbulence paramaters for backward facing step from Fabritius (2014)

	Standard	Optimised
$C_1$	1.44	1.92
$C_2$	1.92	1.86

## 5.2 OPTIMISATION STUDIES WITH STAGGERED GRID

Lid driven cavity problem has been investigated with different objective functions and optimisation variables using staggered grid solver. Viscous, laminar, compressible form of the Navier Stokes equations have been utilised. Objective functions involve target temperatures. Genetic algorithm has been applied. Overall workflow of the optimisation procedure is given in Figure 5.4.

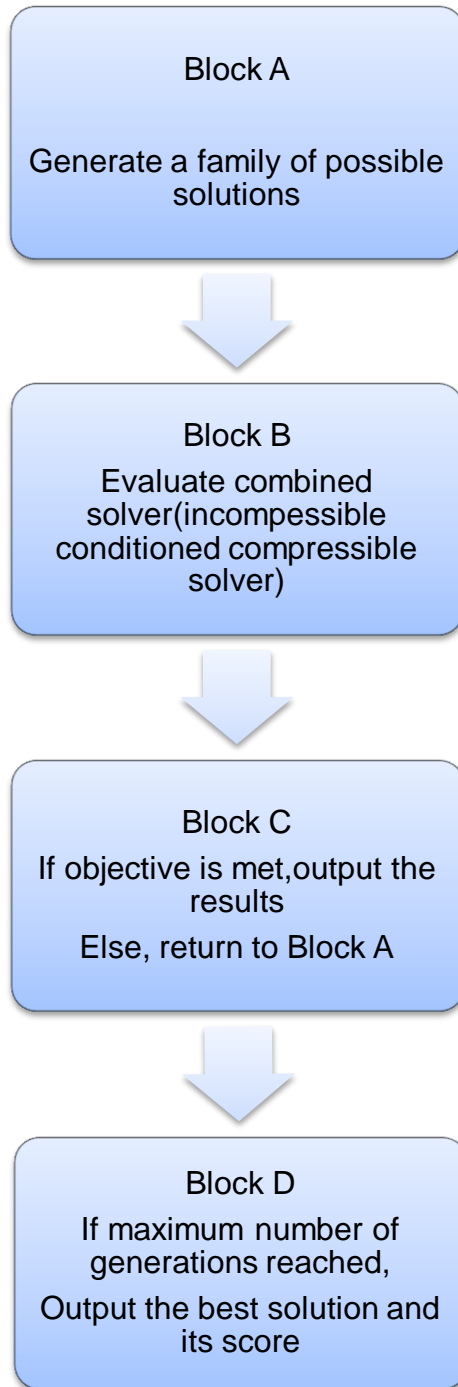


Figure 5.4. Flowchart of the genetic algorithm

### 5.2.1 Optimisation With A Target Middle Temperature

A target middle position temperature of 280 K have been formulated as an objective function and the wall temperatures are defined as the optimisation variables. The grid

size chosen is 10x10 and the grid type is staggered. As presented in the previous chapters, this mesh density provides acceptable accuracy. To avoid excessive computation time, this mesh density has been employed.

The objective function is defined as:

Objective function=  $\text{abs}(T_{\text{mid}}-280)$ , where abs signifies the absolute value.

Genetic algorithm optimisation work have been carried out for 15 generations in the following study. Population size for each generation has been selected as 10. Elite count is selected as 1. Elite solution is the solution that is passed to the next generation of solution.

Table 5-2 Optimisation parameter values, the first lid driven cavity problem

$T_{\text{topwall}}$	200-300 K
$T_{\text{bottomwall}}$	200-300 K
$T_{\text{leftwall}}$	200-300 K
$T_{\text{rightwall}}$	200-300 K

The best solution obtained from optimisation is given in Table 5-3.

Table 5-3 Optimum solution for target mid temperature

$T_{\text{topwall}}$	$T_{\text{bottomwall}}$	$T_{\text{leftwall}}$	$T_{\text{rightwall}}$
266	249	253	296

The score for this solution (value of objective function) is: 0.0045 So, optimisation has been terminated with good accuracy.



### 5.2.2 Optimisation With Top Lid Velocity As An Optimisation Variable

In this case, top wall, left wall, right wall temperatures and lid velocity have been selected as optimisation parameters. The bottom wall of the cavity is fixed at temperature (400 K). The grid used in Section 5.2.1 is used here as well.

The objective function is defined as:

Objective function =  $\text{abs}(T_{\text{mid}} - 300)$ , where abs signifies the absolute value.

Genetic algorithm optimisation work has been carried out for 15 generations in the following study. Population size for each generation has been selected as 10. Elite count is selected as 1. Elite solution is the solution that is passed to the next generation of solution.

Allowed values for optimisation variables are given in Table 5-4.

Table 5-4 Optimisation parameter values, the second lid driven cavity problem

$T_{\text{topwall}}$	200-300 K
$T_{\text{leftwall}}$	200-300 K
$T_{\text{rightwall}}$	200-300 K
Lid velocity	0-12 m/s

The best solution obtained from optimisation is given in Table 5-5.

Table 5-5 Optimum solution for target mid temperature, lid velocity as a optimization parameter

$T_{\text{topwall}}$	Lid velocity	$T_{\text{leftwall}}$	$T_{\text{rightwall}}$
299 K	10 m/s	228 K	284 K

The score for this solution (value of objective function) is 0.0192. This indicates that optimisation resulted in a very close value to the desired value of 300 K. Note also that the temperatures and lid velocity required are rather hard to predict without a proper optimisation work.

### 5.2.3 Optimisation With Top Lid Velocity And Location of a Heat Sink As Optimisation Variables

This time; left, right, top wall temperatures, lid velocity, and location of a heat sink have been selected as optimisation variables. Bottom wall is kept at 400 Kelvins again. So that in total 6 optimisation variables are present. Such a problem with more than a few optimisation variables is particularly suited to genetic algorithm procedure. The grid used in Section 5.2.1 is used here also. The objective function is defined as:

Objective function=  $\text{abs}(T_{\text{mid}}-280)$ , where abs signifies the absolute value.

Allowed values for optimisation variables are given in Table 5-6.

Table 5-6 Optimisation parameter values, the third lid driven cavity problem

$T_{\text{topwall}}$	200-300 K
$T_{\text{leftwall}}$	200-300 K
$T_{\text{rightwall}}$	200-300 K
Lid velocity	0-12 m/s
X node location of heat sink	9-9 (Next to right wall)
Y node location of heat sink	2-9 (Interior nodes)

The results have been presented in Table 5-7. Y location has been found close to the bottom wall. (Third node from the bottom, which means 0.2 m above the bottom wall.)

Table 5-7 Optimum solution for target mid temperature using heat sink as an optimization parameter

$T_{\text{topwall}}$	Lid velocity	$T_{\text{leftwall}}$	$T_{\text{rightwall}}$	X location of heat sink	Y location of heat sink
242 K	7 m/s	266 K	263 K	9	3

The score for this solution (value of objective function) is 0.0204. Again, the value obtained for mid temperature is very close to the target temperature. The heat sink location has been obtained with optimisation procedure and it is closer to the hotter bottom wall (400 K) than the top wall.

### 5.3 OPTIMISATION STUDIES WITH COLLOCATED GRID

In this part, optimisation studies that have been performed with collocated grid solver have been presented. In the first two sections, solver settings have been optimised. Then, optimisation procedure has been applied to impinging jet flow for two different cases.

#### 5.3.1 Solver Settings Used As Optimisation Variables (Number Of Iterations for Momentum and Pressure correction equation)

In this part, solver settings themselves have been subjected to optimisation. Collocated grid solver has been used for the lid driven cavity problem. A 28x28 grid and Reynolds number of 100 has been specified. Fixed number of iterations have been utilised for momentum and pressure correction equations. The iterations have been performed till the following error condition is met:

Infinity norm of maximum flux imbalance across cells/grid spacing  $> 10^{-4}$

For the number of iterations the intervals given in Table 5-8 have been specified.

Table 5-8 Optimisation variable intervals

Iteration <sub>momentum</sub>	1-12
Iteration <sub>pressure correction</sub>	1-12

Genetic algorithm solver settings have been specified below in Table 5-9.

Table 5-9 Genetic algorithm settings

Population for each generation	8
Number of generations	15

Elite member count	1
--------------------	---

The objective function is defined using the computation time. For this problem,

Objective function= computation time of the solver for a set of variables.

Out of 144 possible solutions, only 31 solutions have been performed. The results are given below in Table 5-10.

Table 5-10 Optimisation results

Iteration <sub>momentum</sub>	5
Iteration <sub>pressure correction</sub>	9
Computation time	43.8 seconds

This is the minimum time found in the overall optimisation procedure. Results of the members of possible solution family have been given below for reference in Table 5-11.

Table 5-11 Optimum momentum and pressure iterations for optimizing computation time

Population		Scores (Computation time in seconds)
Iteration <sub>momentum</sub>	Iteration <sub>pressure</sub>	
6	10	44.2497
<b>5</b>	<b>9</b>	<b>43.7923</b>
7	10	45.5584
5	11	47.7738

As a comparison, using Iteration<sub>momentum</sub>= Iteration<sub>pressure</sub>=1 results in 87.2 seconds of computation time. So that the overall computation time can be halved by selecting appropriate solver variables.

### 5.3.2 Solver Settings Used As Optimisation Variables (Number Of Iterations for Momentum and Pressure correction equations, Under-relaxation Terms for Pressure and Momentum)

In this part, solver settings themselves have been subjected to optimisation. Collocated grid solver has been used for the lid driven cavity problem. Since the aim is to select appropriate solver parameters fast convergence have been sought. So, a 40x40 grid have been utilised on a collocated grid.

Fixed number of iterations have been utilised for momentum and pressure correction equations. The iterations have been performed till the following error condition is met:

Infinity norm of maximum flux imbalance across cells  $> 10^{-5}$

For the number of iterations the following intervals have been specified in Table 5-12.

Table 5-12 Optimisation parameter intervals

Iteration <sub>momentum</sub>	1-12
Iteration <sub>pressure correction</sub>	1-12
Under-relaxation for pressure	0.5-0.9
Under-relaxation for momentum equations	0.5-0.9(selected same for u,v)

Genetic algorithm solver settings have been specified below in Table 5-13.

Table 5-13 Genetic algorithm solver settings for collocated grid

Population for each generation	10
Number of generations:	20
Elite member count	1

The objective function is defined using the computation time. For this problem,

Objective function= computation time of the solver for a set of variables x10

The results are given in Table 5-14 including the minimum computation time found from optimisation.

Table 5-14 Optimum under-relaxation parameters for optimizing computation time

Population				Scores (Computation time in seconds)
Iteration <sub>momentum</sub>	Iteration <sub>pressure</sub>	$\alpha_p$	$\alpha_u, \alpha_v$	
<b>5</b>	<b>6</b>	<b>0.9</b>	<b>0.9</b>	<b>126.9</b>
4	6	0.9	0.9	128.6

As a comparison, using Iteration<sub>momentum</sub>=1; Iteration<sub>pressure</sub>=1;  $\alpha_p = \alpha_u = \alpha_v = 0.5$  results in 409.2 seconds computation time. The computation has been reduced to **31%** percent of its original value. Increasing momentum and pressure inner iterations helps achieve faster convergence up to a point. If momentum and pressure inner iterations are increased excessively, solution time again increases.

### 5.3.3 First Impinging Jet Optimisation With Only Thermal Parameters

Impinging jet optimisation problem has been studied with unsteady simulation involving also the solution of energy equation. The top wall and bottom wall temperatures are selected as optimisation variables while the right and left outlets are kept at room temperature (293 K). Unsteady simulation has been run for 50 seconds. The optimisation target function has been defined such as to maximise the stagnation point Nusselt number.

Objective function= $-\text{Nu}_s$

The solution domain is schematically shown in Figure 5.5.

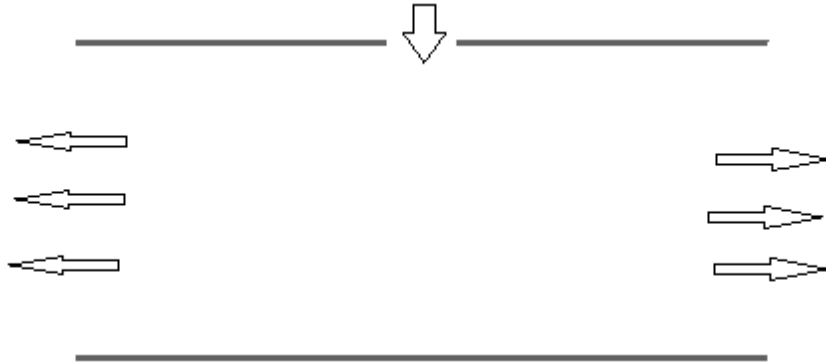


Figure 5.5. Single impinging jet flow outline of domain

The parameter value intervals used for the optimisation work are given in Table 5-15.

Table 5-15 First impinging jet optimisation parameter value intervals

Top wall temperature	295-400 K
Bottom wall temperature	295-400 K

Due to the few number of variables, 20 generations with 10 population has been run. The best candidate that is passed over to next generation (elite member) is kept at 1. The maximum stagnation point Nusselt number is obtained with highest bottom wall and lowest top wall temperature as given in Table 5-16.

Table 5-16 First impinging jet optimisation parameter values

Top wall temperature	295 K
Bottom wall temperature	400 K

### 5.3.4 Second Impinging Jet Optimisation With Thermal, Fluid and Geometric Parameters

Impinging jet optimisation problem has been studied with unsteady simulation involving also the solution of energy equation. Unsteady simulation has been run for 50 seconds. Impinging jet optimisation problem has been studied with fluid and geometric variables apart from thermal variables. 6 parameters (bottom wall temperature, top wall temperature, impinging jet domain height, impinging jet domain

length, Reynolds number, injection nozzle width) have been selected as optimisation variables. The selected intervals for these variables are listed in Table 5-17.

Table 5-17 Second impinging jet optimisation parameter value intervals

Top wall temperature	295-330 K
Bottom wall temperature	400-500 K
Injection nozzle width	1-3
Height of impinging jet domain	1-4
Length of impinging jet domain	15-25
Reynolds number	100-1000

Objective function has been defined as:

Objective function =  $-Nu_s$

The optimization problem has been run with genetic algorithm for 40 generation with 35 population. Optimum result (highest stagnation point Nusselt number) is obtained with the set of values for the optimization variables given in Table 5-18.

Table 5-18 Second impinging jet optimisation parameter values

Top wall temperature	295
Bottom wall temperature	459
Injection nozzle width	3
Height of impinging jet domain	1
Length of impinging jet domain	15
Reynolds number	1000

Decreasing the height of impinging jet domain, length of domain, and the top wall temperature while increasing injection nozzle width maximise the stagnation point Nusselt number. Due to the thermal fluid interaction, stagnation point Nusselt number is not maximised when bottom wall is at the maximum allowable temperature. Rather,



a value approximately at the middle of the selected interval (400-500 K) optimises the stagnation point Nusselt number.

## 6. CONCLUSION

In the thesis, incompressible and compressible flow solvers that can run together has been developed. The incompressible solution has been fed into the compressible solver automatically to speed up convergence and increase stability of the solution algorithm. Both staggered and collocated grid arrangements have been studied numerically. It has been observed that both grid arrangements can be used for both flow regimes but their behaviour is characteristically different. One should pay extra attention to face interpolation of variables at cell faces to avoid divergence and irrelevant results in the collocated grid. Staggered arrangement is a more natural way of handling especially in the case of compressible flows as it does not require a face interpolation for velocity. But it is slightly more difficult to program and implement.

The developed code has been applied to lid driven cavity and impinging jet flow problems. The results have been compared to those found in the literature whenever applicable and good conformity has been observed.

The thermal effects have also been studied as part of the compressible field simulations. It has been observed that despite low velocities, significant compressibility effects are present due to thermal effects for both lid driven cavity and impinging jet flows.

Preconditioning has been applied to compressible flow with incompressible flow solution. For the preconditioning, pseudo-transient under-relaxation has been utilised for momentum equations. It has been shown that computational time to march to a convergent solution can be reduced significantly with this approach. For the lid driven cavity problem, after 6 seconds marching in time and reaching to a convergent state, 30% reduction in computational time has been achieved.

Optimisation studies have been carried out with the in-house code. As part of the optimisation studies genetic algorithm has been used. Different problems have been investigated. Optimisation of solver settings have been done. Under-relaxation parameters, and number of iterations for momentum and pressure correction

equations have been selected as optimisation variables. It has been observed that computational time can be significantly reduced with the optimised selection of solver parameters after the optimisation.

As a test case for the lid driven cavity optimisation problem, location of a heat sink, and boundary conditions for temperature and velocity have been selected as optimisation parameters to obtain a target temperature value in the middle of the domain. This analysis enabled the positioning of the heat sink inside the domain.

For the impinging jet flow problem, several optimisation studies have been performed to obtain highest possible stagnation point Nusselt number at the impingement wall. First, a simpler optimisation problem where only thermal parameters are used as optimisation variables have been solved. Secondly, an optimisation problem, where thermal, fluid and geometric properties are used as optimisation variables have been solved. For the bottom wall, a temperature value at the middle of the selected optimisation interval maximises the stagnation point Nusselt number. So that the dependency of the stagnation point Nusselt number on the bottom wall temperature is found to be nonlinear.

## 7. REFERENCES

- 1) Arani, A., Abbaszadehi, M., Ardeshiri, A., Mixed convection fluid flow and heat transfer and optimal distribution of discrete heat sources location in a cavity filled with nanofluid, *Trans. Phenom. Nano Micro Scales*, vol. 5(1), pp. 30-43, **2017**.
- 2) Bhuiyan, A. B., Alam, M. S., Alim, M. A., Numerical simulation of heat transfer and fluid flow with lid-driven square cavity and discrete source-sink pairs, *American Institute of Physics Conference Proceedings*, 1851, 020049, 2017.
- 3) Braembussche, R., Numerical Optimization for Advanced Turbomachinery in *Optimization and Computational Fluid Dynamics*, pp.147-189, 2007.
- 4) Chorin, A.J., A numerical method for solving incompressible viscous flow problems. *Journal of Computational Physics*, Vol. 2, pp. 12-26, 1967.
- 5) Choi, S. K., Note on the use of momentum interpolation method for unsteady flows. *Numerical Heat Transfer: Part A: Applications*, vol. 36, pp. 545–550, 1999.
- 6) Chou, Y. J., Hung, Y., Isothermally Heated Surface With a Confined Slot Jet, *Journal of Heat Transfer*, Vol. 116, pp. 479-482, 1994.
- 7) Chung, Y. M., Luo, K. H., Unsteady Heat Transfer Analysis of an Impinging Jet, *Journal of Heat Transfer*, Vol. 124, pp.1039-1048, 2002
- 8) Dagtekin, I., Oztop, H. F., Heat transfer due to double laminar slot jets impingement onto an isothermal wall within one side closed long duct, *International Communications in Heat and Mass Transfer*, Vol. 35, pp. 65–75, 2008.
- 9) Darwish, M., Mangani, L., Moukalled, F., *The Finite Volume Method In Computational Fluid Dynamics*, Springer International Publishing, 2016.
- 10) Dumas, L. *CFD Based Optimization for Automative Aerodynamics*, *Optimization and Computational Fluid Dynamics* pp.191-215, 2007.
- 11) Fabritius, B., *Application of Genetic Algorithms to Problems in Computational Fluid Dynamics*, University of Exeter, Doctor of Philosophy in Engineering, 2014.
- 12) Ferziger, J. H., Peric, M., *Computational Methods for Fluid Dynamics*, 3rd ed., Springer, New York, 2002.
- 13) Ghia, U., Ghia, K. N., and Shin, C. T., High-Re solutions for incompressible flow using the Navier-Stokes equations and a multigrid method, *Journal of Computational Physics*, Vol. 48, pp. 387-411, 1982.
- 14) Glauert, M. . The Wall Jet, *Journal of Fluid Mechanics*, V. 1 , pp.625-643, 1956.
- 15) Goldberg, D. E., *Genetic Algorithms in Search, Optimization and Machine Learning*, 1989.

- 16) Gray, D. G., Giorgini, A., The Validity Of The Boussinesq Approximation For Liquids And Gases, hr. J. Hear Mass Transfer. Vol. 19, pp. 545-551, 1975.
- 17) Gupta, T., Optimisation of Benchmark Functions Using Genetic Algorithm, International Journal of Advanced Research in Computer Engineering & Technology (IJARCET) Vol. 5(1), 2016.
- 18) Hadhrami, L. M. A., Shaahid, S. M., Mubarak A. A., Jet Impingement Cooling in Gas Turbines for Improving Thermal Efficiency and Power Density, Advances in Gas Turbine Technology, pp. 191-210, 2011.
- 19) Harlow, F. H., Welch, J. E., Numerical Calculation of Time-Dependent Viscous Incompressible Flow with Free Surface, The physics of fluids, Volume 8, pp. 2182-2189. 1965.
- 20) Heiningen, A. R. P., Mujumdar, A. S., Douglas, W. J. M., Numerical Prediction of the Flow Field and Impingement Heat Transfer Caused by a Laminar Slot Jet, Journal of Heat Transfer, Transactions of ASME, pp. 654-658, 1976.
- 21) Hussain, A Numerical Study of Compressible Lid Driven Cavity Flow with a Moving Boundary, MSc Thesis, Jawaharlal Nehru Technological University, 2016.
- 22) Ianelli, P., Wild, J., Minervino, M., Moens, F., and Raets, M., Analysis And Application Of Suitable Cfd-based Optimization Strategies For High-lift System Design, European Congress on Computational Methods, 2012.
- 23) Issa, R.I., Solution of the implicitly discretized fluid flow equations by operator-splitting, Journal of Computational Physics Vol. 62, pp. 40–65, 1985.
- 24) Lee, H.G., Yoon, H.S., Ha, M.Y., A Numerical Investigation on the Fluid Flow and Heat Transfer in the Confined Impinging Slot Jet in the Low Reynolds Number Region for Different Channel Heights, Int. J. Heat Mass Transfer, Vol. 51, pp. 5055-4068, 2008.
- 25) Leonard, B. P. Computer Methods In Applied Mechanics And Engineering 19, pp. 59-98, 1979.
- 26) Lorenzo, G., Manca, O., Nardini, S., Ricci, D., Numerical Study of Laminar Confined Impinging Slot Jets with Nanofluids, Advances in Mechanical Engineering, 2012.
- 27) Majumdar, S. Role Of Underrelaxation in Momentum Interpolation for Calculation of Flow with Nonstaggered Grids, Numerical Heat Transfer, vol. 13, pp. 125-132, 1988.
- 28) Narumanchi, S. V. J., Hassani, V., Bharathan, D., Modeling Single-Phase and Boiling Liquid Jet Impingement Cooling in Power Electronics, National Renewable Energy Laboratory Technical Report NREL/TP-540-38787, 2005.
- 29) Nastase, A., Computation of Supersonic Flow over Flying Configurations, First edition, Great Britain: Elsevier, 2008.
- 30) Patankar, S., Numerical Heat Transfer and Fluid Flow, 1980.

- 31) Rhie, C. M. and Chow, W. L., Numerical study of the turbulent flow past an airfoil with trailing edge separation, *AIAA Journal*, vol. 21, pp. 1525-1532, 1983.
- 32) Riley, N., Effects of compressibility on a laminar wall jet, *Journal of Fluid Mechanics*, Vol. 4 (6), pp. 615-628, 1958.
- 33) Sahoo, D., Sharif, M. A. R., Numerical modeling of slot-jet impingement cooling of a constant heat flux surface confined by a parallel wall, *International Journal of Thermal Sciences* vol. 43, pp. 877–887, 2004.
- 34) Sezai, I., Mohamad, A. A. Three-Dimensional Simulation of Laminar Rectangular Impinging Jets, Flow Structure, and Heat Transfer *Journal of Heat Transfer*, Transactions of ASME, pp. 51-56. 1999.
- 35) Shah, P., Rovagnati, B., Mashayek, F. Jacobs, G.B., Subsonic compressible flow in two-sided lid-driven cavity. Part I: Equal walls temperatures, *International Journal of Heat and Mass Transfer*, Volume 50, Issues 21–22, Pages 4206-4218, 2007.
- 36) Shuja, S.Z., Yilbas, B. S., A laminar swirling jet impingement on to an adiabatic wall: Effect of inlet velocity profiles, *International Journal of Numerical Methods for Heat & Fluid Flow*, Vol. 11 No. 3, 2001, pp. 237-254, 2001.
- 37) Spalding, D.B., A Novel Finite-difference Formulation for Differential Expression Involving Both First and Second Derivatives, *Int. J. Numer. Methods Eng.*, Vol. 4., 1972.
- 38) Taher, M. A., Saha, S. C., Lee, Y. W., Kim, H. D., Numerical Study of Lid-Driven Square Cavity with Heat Generation Using LBM, *American Journal of Fluid Dynamics* 2013, Vol. 3(2), pp. 40-47, 2013.
- 39) Tahsini, A. M., Mousavi, S. T., Laminar Impinging Jet Heat Transfer for Curved Plates, *International Journal of Aerospace and Mechanical Engineering*, Vol. 6 (12), pp. 2788-2793, 2012.
- 40) Tanner, F. X., Srinivasan, S., CFD-based optimization of fuel injection strategies in a diesel engine using an adaptive gradient method, *Applied Mathematical Modelling*, 33, pp. 1366–1385, 2008.
- 41) Turgeon, E., Pelletier, D., Ilinca, F., Compressible Heat Transfer Computations By An Adaptive Finite Element Method, 37th AIAA Aerospace Sciences Meeting and Exhibit, 1999.
- 42) Van Leer, B., Towards the Ultimate Conservative Difference Scheme V. A Second Order Sequel to Godunov's method, *J. Computational Physics*, 32, pp.101-136, 1979.
- 43) Versteeg, H., Malalasekera, W., *An Introduction to Computational Fluid Dynamics: The Finite Volume Method*, Pearson Prentice Hall, 2nd edition, 2010.

- 44) Yu, B., Tao W., Wei, J. Kawaguchi, Y., Tagawa, T., Ozoe, H., et al., Discussion On Momentum Interpolation Method For Collocated Grids of Incompressible Flow, Numerical Heat Transfer Part B, 42: 141-166, 2002.
- 45) Zhang, F., Chen, S., and Khalid, M., Optimizations Of Airfoil And Wing Using Genetic Algorithm, Congress of International Council of the Aeronautical Sciences(ICAS), 2002.

## APPENDICES

### APPENDIX 1: DISCRETISATION OF FLUXES

The flux discretization schemes are briefly reviewed in this Appendix. Coefficients used in the transport equations for the schemes described below are given by Malalasekera and Versteeg (2010).

In central differencing scheme, face values of variables are obtained by linear interpolation. Since central differencing scheme does not take into account the direction of the flow, it is used for diffusive terms mainly in the solution.

$$\phi_{i=e,w,n,s} = 0.5 * \phi_P + 0.5 * \phi_{i=E,W,N,S} \quad (\text{A1. 1})$$

The convection diffusion equation with the neighbor coefficients in 2 dimensions can be represented as follows:

$$a_P \phi_P = a_e \phi_E + a_w \phi_W + a_n \phi_N + a_s \phi_S + RHS \quad (\text{A1. 2})$$

Here, RHS term represents pressure, source, and other terms that appear in the equation depending on the physical variable solved.

The generalization of the central differencing scheme to 2 dimensions for the convective and diffusive terms yields:

$$a_w = D_w + \frac{F_w}{2} \quad (\text{A1. 3})$$

$$a_e = D_e - \frac{F_e}{2} \quad (\text{A1. 4})$$

$$a_n = D_n - \frac{F_n}{2} \quad (\text{A1. 5})$$

$$a_s = D_s - \frac{F_s}{2} \quad (\text{A1. 6})$$



In first order upwind scheme, face values are obtained based on the direction of the convective flux.

$$\phi_e = \begin{cases} \phi_P, & F_e \geq 0 \\ \phi_E, & F_e < 0 \end{cases} \quad (\text{A1. 7})$$

The generalization of the central differencing scheme to 2 dimensions for the convective and diffusive terms yields:

$$a_w = D_w + \max(F_w, 0) \quad (\text{A1. 8})$$

$$a_e = D_e + \max(-F_e, 0) \quad (\text{A1. 9})$$

$$a_n = D_n + \max(-F_n, 0) \quad (\text{A1. 10})$$

$$a_s = D_s + \max(F_s, 0) \quad (\text{A1. 11})$$

The hybrid scheme combines the first order upwind scheme and central differencing scheme. Depending on the cell Peclet number either of these methods is utilized to obtain the fluxes at cell faces.

$$a_w = \max\left(F_w, \left(D_w + \frac{F_w}{2}\right), 0\right) \quad (\text{A1. 12})$$

$$a_e = \max\left(-F_e, \left(D_e - \frac{F_e}{2}\right), 0\right) \quad (\text{A1. 13})$$

$$a_s = \max\left(F_s, \left(D_s + \frac{F_s}{2}\right), 0\right) \quad (\text{A1. 14})$$

$$a_n = \max\left(-F_n, \left(D_n - \frac{F_n}{2}\right), 0\right) \quad (\text{A1. 15})$$

For cartesian grids, convective terms (F) terms and diffusive terms (D) are given by the following expressions.

$$F_e = (\rho u)_e A_e \quad (\text{A1. 16})$$

$$F_w = (\rho u)_w A_w \quad (\text{A1. 17})$$

$$F_n = (\rho v)_n A_n \quad (\text{A1. 18})$$

$$F_s = (\rho v)_s A_s \quad (\text{A1. 19})$$

$$D_w = \left(\frac{\mu}{\Delta x}\right)_w A_w \quad (\text{A1. 20})$$

$$D_e = \left(\frac{\mu}{\Delta x}\right)_e A_e \quad (\text{A1. 21})$$

$$D_s = \left(\frac{\mu}{\Delta x}\right)_s A_s \quad (\text{A1. 22})$$

$$D_n = \left(\frac{\mu}{\Delta x}\right)_n A_n \quad (\text{A1. 23})$$



HACETTEPE UNIVERSITY  
GRADUATE SCHOOL OF SCIENCE AND ENGINEERING  
THESIS/DISSERTATION ORIGINALITY REPORT

HACETTEPE UNIVERSITY  
GRADUATE SCHOOL OF SCIENCE AND ENGINEERING  
TO THE DEPARTMENT OF MECHANICAL ENGINEERING

Date: 10/06/2019

Thesis Title / Topic: **Development of a Navier Stokes solver for compressible viscous flows and coupling it with optimization codes**

According to the originality report obtained by my thesis advisor by using the *Turnitin* plagiarism detection software and by applying the filtering options stated below on 10/06/2019 for the total of 94 pages including the a) Title Page, b) Introduction, c) Main Chapters, d) Conclusion sections of my thesis entitled as above, the similarity index of my thesis is 8 %.

Filtering options applied:

1. Bibliography/Works Cited excluded
2. Quotes included
3. Match size up to 5 words excluded

I declare that I have carefully read Hacettepe University Graduate School of Science and Engineering Guidelines for Obtaining and Using Thesis Originality Reports; that according to the maximum similarity index values specified in the Guidelines, my thesis does not include any form of plagiarism; that in any future detection of possible infringement of the regulations I accept all legal responsibility; and that all the information I have provided is correct to the best of my knowledge.

I respectfully submit this for approval.

Name Surname: Burak PEHLIVAN

Student No: N14221228

Department: Mechanical Engineering

Program: Mechanical Engineering

Status:  Masters  Ph.D.  Integrated Ph.D.

10/06/2019  
Date and Signature

**ADVISOR APPROVAL**

APPROVED.

Assist. Prof. Dr. Özgür EKİCİ

(Title, Name Surname, Signature)

## CURRICULUM VITAE

### Credentials

Name, Surname: Burak PEHLİVAN  
Place of Birth: Elazığ  
E-mail: burakpehlivn@gmail.com  
Address: Yenimahalle ANKARA

### Education

High School: Gazi Anatolium  
BSc.: Aerospace Engineering, Middle East Technical  
University  
MSc.: Mechanical Engineering, Hacettepe University

### Foreign Languages

English (Fluent)

### Work Experience

Turkish Technic – Maintenance Engineer(2013-14)  
University of Turkish Aeronautical Association – Research Assistant(2014-  
2015)  
Ministry of Transport and Infrastructure (2015- ) – Expert

### Areas of Study

Computational Fluid Dynamics and Heat Transfer, Aerodynamics,  
Optimization, Numerical Modelling